Universiteit Leiden
The Netherlands

Novel applications of objective measures in cochlear implants

Dong, Y.

Citation

Dong, Y. (2022, February 15). *Novel applications of objective measures in cochlear implants*. Retrieved from https://hdl.handle.net/1887/3275097

Version:	Publisher's Version
License:	Licence agreement concerning inclusion of doctoral thesis in the Institutional Repository of the University of Leiden
Downloaded from:	https://hdl.handle.net/1887/3275097

Note: To cite this publication please use the final published version (if applicable).

Novel Applications of Objective Measures in Cochlear Implants

Yu Dong

董宇

Novel Applications of Objective Measures in Cochlear Implants

Leiden University Medical Center
Department of Otorhinolaryngology
© copyright Yu Dong, 2022

Layout & cover design: Yu Dong, Sarah Wang
Printing: ProefschriftMaken || www.proefschriftmaken.nl
ISBN 978 94 6423 650 7

All Rights Reserved. No part of this publication may be reproduced, stored in a retrieval system or transmitted, in any form or by any means, electronic, mechanical, photocopying, recording or otherwise, without prior permission of the author or the copyright-owning journals for previous published chapters.

This thesis was financially supported by: Advanced Bionics and Oticon Medical.

Novel Applications of Objective Measures in Cochlear Implants

PROEFSCHRIFT

ter verkrijging van

de graad van doctor aan de Universiteit Leiden,

op gezag van rector magnificus prof.dr.ir. H. Bijl,

volgens besluit van het college voor promoties

te verdedigen op

dinsdag 15 februari 2022 klokke 16:15

door

Yu Dong

geboren te Sichuan, China

in 1988

Promotor

Prof. dr. ir. J.H.M. Frijns

Copromotoren

Dr. ir. J.J. Briaire

Dr. ing. H.C. Stronks

Leden promotiecommissie

Prof. dr. P.P.B. van Benthem

Dr. M.J. van Gendt

Prof. J. Firszt, PhD	Washington University
Dr. H. Versnel	Universiteit Utrecht Medical Center

For my family

Table of contents

Chapter 1 Introduction and outline of the thesis **13**

1.1. Physiology of hearing 15

1.2. Cochlear implant 17

1.3 Objective measures of cochlear implant function 19

1.4 Overview of the current thesis 23

1.4.1 Aims 23

1.4.2 Outline of the current thesis 23

References 25

Chapter 2 An iterative deconvolution model to extract the temporal firing properties of the auditory nerve fibers in human eCAPs **31**

Abstract 32

2.1 Background 32

2.2 Model Construction 36

2.2.1 Construction of the UR and CDLD 36

2.2.2 Optimization routine 37

2.2.3 Extraction of temporal AN firing properties from eCAPs 38

2.3 Method validation 41

2.4 Conclusion 43

References 44

Chapter 3 Unravelling the Temporal Properties of Human eCAPs through an Iterative Deconvolution Model **47**

Abstract 48

3.1. Introduction 49

3.2. Materials and methods 53

3.2.1. Patients and recordings 53

3.2.2. Deconvolution model 54

3.2.3 The validation of the two-Gaussian component CDLD model 58
3.3. Results 60
3.3.1 The unitary response of human auditory nerve fibers 59
3.3.2 Typical cases in the deconvolution model 60
3.3.3 Temporal properties of human eCAPs 60
3.4. DISCUSSION 62
3.4.1 The UR of human auditory nerve fibers 63
3.4.2 The temporal information of eCAPs contained in CDLDs 65
3.5 Conclusions 68
Acknowledgements 69
References 70
Chapter 4 Predicting speech performance in individuals with cochlear implants, based on temporal firing properties of auditory nerve fibers derived from eCAPs 75
Abstract 76
4.1 Introduction 77
4.2 MATERIAL AND METHODS 80
4.2.1 Patient Population 80
4.2.2 Data Recordings 81
4.2.3 Evaluation of Speech Perception 84
4.2.4 Statistical Analysis 84
4.3 RESULTS 86
4.3.1 Derivation of CDLDs 86
4.3.2 Relationship between CDLDs and Speech Perception 86
4.3.3 Abilities of CDLD Parameters, eCAP Amplitude, and AGF Slope to Explain the Variance in Speech Perception 88
4.4 DISCUSSION 91
4.5 CONCLUSIONS 95
ACKNOWLEDGMENTS 96
REFERENCES 97

Chapter 5 Short and long-latency components of the eCAP reveal different refractory properties **103**

Abstract 104

5.1 Introduction 105

5.2 MATERIAL AND METHODS 108

5.2.1 Patients 108

5.2.2 Data recordings 108

5.2.3 Analysis 110

5.2.4 Speech perception 112

5.2.5 Statistics 112

5.3 RESULTS 114

5.3.1 Extraction of S-eCAP and L-eCAP from R-eCAP 114

5.3.2 The refractory parameters derived from the R-RRF, S-RRF, and L-RRF 115

5.3.3 Comparisons of refractory parameters between children and adults 117

5.3.4 Relations between refractory parameters and speech perception 118

5.4 DISCUSSION 119

5.4.1 The refractory properties derived from the R-RRF, S-RRF, and L-RRF 119

5.4.2 Refractory characteristics of the AN in children and adults 120

5.4.3 Effects of auditory refractory properties on speech perception 122

5.5 CONCLUSIONS 123

ACKNOWLEDGMENTS 123

REFERENCES 124

Chapter 6 Detection of Translocation of Cochlear Implant Electrode Arrays by Intracochlear Impedance Measurements **129**

Abstract 130

6.1 Introduction 131

6.2 MATERIAL AND METHODS 135

6.2.1 Subjects 135

6.2.2 Data recording 136

6.2.3 Translocation detection from CT imaging 137

6.2.4 Analysis 137
6.3 RESULTS 139
6.4 DISCUSSION 142
6.5 CONCLUSIONS 146
ACKNOWLEDGMENTS 147
REFERENCES 148
Chapter 7 General discussion 153
7.1 Application of physiological measures in cochlear implants 156
7.2 Application of nonphysiological measures in cochlear implants 158
7.3 Clinical implications 160
7.4 Future perspectives 161
REFERENCES 164
Chapter 8 168
Summary 169
Samenvatting 175
List of publications 181
Curriculum Vitae 185
Acknowledgements 189

Chapter 1

Introduction and outline of the thesis

1.1. Physiology of hearing

Hearing, or auditory perception, begins when the auditory system transduces sound vibrations into nerve impulses and forwards them to the brain, where they are perceived as sounds. The sense of hearing plays a crucial role in maintaining connections with the world around us. Our external ears capture this mechanical signal, the middle ear transmits it to the receptor organ, the cochlea, which transduces it into neural signals to the central nervous system (Figure 1.1A). The external ear consists of the auricle and the external ear meatus, which ends at the tympanic membrane (eardrum). In the air-filled middle ear, three tiny connected auditory ossicles are located, namely the malleus, the incus, and the stapes. The stapes is placed on the oval window, which separates the middle ear from the inner ear, or cochlea. The cochlea is a coiled tube, divided into three liquid-filled compartments: the scala tympani, scala media, and scala vestibuli (Figure 1.1B). The base of the scala vestibuli is closed by the oval window. The base of the scala tympani ends in the round window, a thin, flexible membranous structure. Both scalae are filled with perilymph. The scala vestibuli and scala tympani communicate with each other at the apical helicotrema.

Between the scala media and the subjacent scala tympani lies the basilar membrane along the length, which supports the organ of Corti (Figure 1.1B). In the process of hearing, sound waves are captured and converged to the external meatus by the auricle. Then sound waves stimulate the tympanic membrane to vibrate, such that the connected ossicular chain starts to vibrate and simultaneously amplify the vibration pressure. Because the stapes connects to the cochlea via the oval window, the action of the stapes produces a travelling wave that propagates along the length of the basilar membrane. As the travelling wave pushes up on the basilar membrane, the hair cells of the organ of Corti are excited resulting in the release of neurotransmitters, which causes the auditory nerve fibers (ANFs) to generate action potentials (Pickles, 1988). These action potentials can be transmitted along the brainstem to the auditory cortex where sound waves are ultimately interpreted as meaningful sounds (Rizzolatti and Kalaska, 2013).

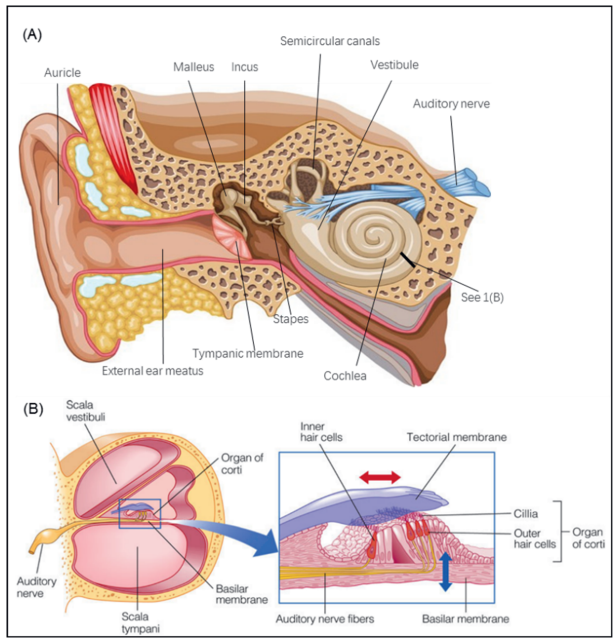

Fig. 1.1. Graphical representation of the basic anatomy of the human ear.

Hearing loss can arise from both physiological and structural defects in the auditory system and can be roughly classified as conductive and sensorineural hearing loss. Conductive hearing loss occurs in the outer and/or middle ear when sound waves cannot be carried through to the cochlea. Sensorineural hearing loss results from damage to the neural structures in the cochlea, auditory nerve or central auditory system (Hartmann and Kral, 2004). In recent decades, remarkable advances in the capability to treat deafness have been achieved. For the majority of patients who have significant residual hearing, such as patients with conductive hearing loss, hearing aids are typically recommended which can amplify sound to activate the residual hair cells. When greater degrees of hearing loss has occurred, the benefit of hearing aid may become insufficient. However, severe hearing loss can be restored with a cochlear implant (CI), which can bypass the hair cells and the whole preceding normal route of sound conduction.

1.2. Cochlear implant

A CI is an implantable electronic prosthesis that can restore a part of the hearing abilities of patients by directly applying electrical stimulation to the auditory nerve fibers (ANFs). In the last decades, CI has become a standard method of rehabilitation for patients with severe to profound hearing loss (stated by WHO, https://www.who.int/en/news-room/fact-sheets/detail/deafness-and-hearing-loss). Although CI designs differ in appearance across manufacturers and generations of technology, all CIs share the same basic components and functions. A CI system is composed of two basic parts. The externally worn part, the sound processor, has microphones, electronics, a battery and a headpiece. The surgically implanted internal component contains a coil to receive signals, electronics and an array of electrode contacts which is typically placed into the scala tympani. A microphone captures sound waves and converts them to electrical signals which are processed in a sound processor. The auditory signals are decoded into a number of frequency bands and the temporal envelope of each band is extracted. The amplitudes of the various frequency bands are forwarded to the receiving antennas implanted in the temporal bone across the skin by radio frequency transmission. The information is further decoded into an electrical current in the internal electronics. Like the basilar membrane and hair cells, the ANFs are tonotopically organized. That is to say, nerve fibers in the basal turn of the cochlea process higher frequencies and lower frequencies in the apical region. Due to this tonotopic organization, electrode contacts are arranged near ANFs along the scala tympani to code specific frequencies. Lead wires carry the electrical signals from the internal electronics to appropriate electrode contacts placed at various locations. Activation of the electrodes evokes action potentials in the nearby auditory nerves and thus produces a different auditory percept.

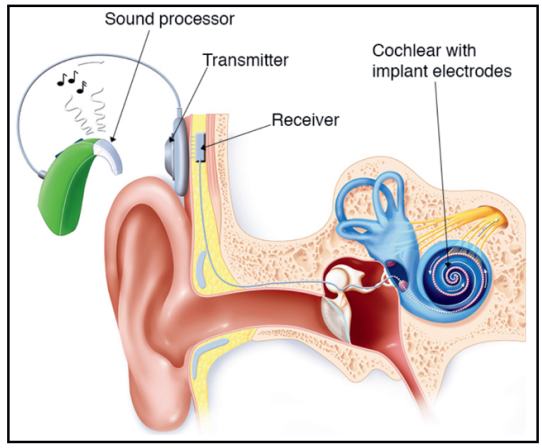

Fig. 1.2 Schematic representation of the basic components of a cochlear implant system. Picture adapted from healthdirect (https://www.healthdirect.gov.au/cochlear-implant#backToTop).

To date, cochlear implantation is the most successful treatment for severe sensorineural hearing loss through developments in speech processing strategies, surgical techniques and electrode designs. As of December 2019, over 736 thousand registered devices worldwide have implanted since their development in the 1970s (stated by NIH, https://www.nidcd.nih.gov/health/cochlear-implantsCochlear). Most patients demonstrate improved speech performance when compared to their pre-implant abilities. However, the outcomes of the population of CI recipients still differ greatly between implanted patients and ears. This makes it difficult to predict post-implantation speech performance before implantation. A multitude of related factors may potentially contribute to the variability, including patient-related characteristics, device designs, and neurophysiological properties. More specifically, factors that attribute to variation in speech outcomes across patients include the degree of nerve degeneration (Shepherd et al., 1983; He et al., 2017), characteristics of the auditory nerve like the capability to recover from the refractory state (Stypulkowski & van den Honert, 1984; Brown et al., 1990; Abbas et al., 1996), age at implantation, duration of deafness, spatial and temporal resolution abilities (Shannon,1983; Zeng & Shannon, 1994), the extent of residual hearing (Miller et al., 2008), the placement of electrode arrays and the integrity of the central auditory nervous system (Oviatt et al., 1991; Micco et al., 1995). Up to now, however, variability in speech perception is not completely understood.

1.3 Objective measures of cochlear implant function

State-of-the-art CIs usually provide multiple objective measures for both clinical and scientific research purposes that can aid in verifying the device function in CI recipients. Objective measures encompass two general measuring techniques, namely physiological measures and nonphysiological measures.

Physiological measures are tools for recording neural responses from different levels of the auditory system in response to electrical stimulation through a CI device. They are usually applied to assess the physiological functioning of the auditory pathway (Botros and Psarros, 2010) and device functionality (Gantz et al., 1988). Although there are some potential clinical applications of physiological measures, the most immediate is to determine if the outcome responses are useful for facilitating the programming of the CI processor so as to achieve better speech perception. The commonly used physiological measures in CI research are electrically evoked stapedial reflexes (ESRs), electrically evoked auditory brainstem responses (EABRs) and electrically evoked compound action potentials (eCAPs).

The scope of physiological measures in this thesis is to apply eCAP measurements involved in CIs. ECAP measures are widely used in clinical practice and represent a synchronous physiological response produced by depolarization of an aggregate population of electrically evoked activity in ANFs (e.g., DeVries et al., 2016; He et al., 2017). Modern CI devices incorporate a reverse telemetry system that allows for eCAPs to be recorded using the intra-cochlear electrode array. In contrast to the acoustically evoked CAP, eCAPs are immune to dampening by the anaesthesia effect and to muscle artefacts (e.g., Stronks et al., 2010; Hughes 2012). As a result, patients do not have to keep still or be asleep or sedated during recording. In sum, the eCAP recording is an easy and quick method to obtain clinically, and they are ideal for use with pediatric or other difficult-to-test patients (van Dijk et al., 2007). Despite the eCAPs recording has been extensively used in clinical practice, the eCAPs are not variable to determine

the behavioural threshold and maximum comfortable hearing levels (e.g., De Vos et al., 2018). The eCAP is usually characterized by the main peak, namely, a negative deflection (N1), followed by a positive peak or plateau, P2 (Fig 1.3) (Stypulkowski & van den Honert,1984; Abbas et al., 1999; Cullington et al., 1997). Earlier studies have used eCAP recordings to objectively assess the performance of CIs, such as the eCAP amplitude growth functions and the refractory recovery function (Abbas et al., 1999; Kim et al., 2010; Walker et al., 2010; He et al., 2017). These eCAP-based studies have mainly focused on the magnitude characteristics of eCAPs rather than temporal firing properties. The morphology of eCAP waveforms is dependent on both the number of action potentials and the degree of synchronicity of neural responses (namely, the temporal firing properties) in the ANF population. As the onsets of speech segments are encoded by the synchronous response of a large number of ANFs, the temporal firing properties may potentially affect CI outcomes. Given that the eCAP amplitudes alone do not provide synchronical information, it is worthwhile to investigate whether the temporal features underlying eCAPs can be indicative of CI outcomes after implantation.

To investigate the temporal firing properties of excited ANFs underlying eCAP, it has been simplified to assume that the neural response of each single ANFs is identical to the so-called unitary response (UR) and that all URs contribute equally to the eCAP (e.g., Versnel et al., 1992a; Strahl et al., 2016; van Gendt et al., 2019). Accordingly, the eCAP can be mathematically described as the convolution of this UR with a compound discharge latency distribution function (CDLD) across all fibres (Goldstein and Kiang 1958; de Sauvage et al., 1987; Versnel et al., 1992b). The CDLD reflects both the weights of all URs of each excited ANF over time as well as the neural synchronicity that the eCAP waveform does not show directly. Strahl et al. (2016) have extracted CDLDs from human eCAP recordings using a convolution model with the guinea pig UR reported by Versnel et al. (1992a). Although this is an interesting approach, it has some serious limitations which will be improved in Chapter 2 of this thesis.

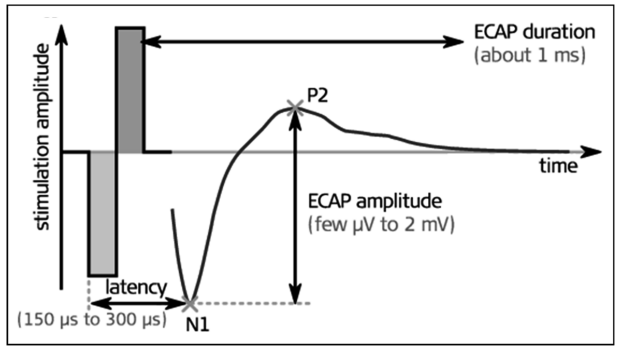

Fig. 1.3 Example of an electrically evoked compound action potential (eCAP) response for a current pulse. The horizontal axis shows time from stimulus onset. The difference between the negative peak N1 and the second positive peak P2 is defined as the eCAP amplitude.

Nonphysiological measures, such as the electrode impedance, and electric field imaging (EFI) are typically applied to evaluate the function of the internal device. These measures can be used to obtain insight into the characteristics of the surrounding tissue, the electrode-tissue interface and the path of current flow.

Electrode impedance depends on the static electrical impedances of the elements involved, but also on dynamic electrochemical processes at the level of this electrode-tissue interface (Fig. 1.4). Electrode impedance consists of the resistance component and the reactance component (Clark et al. 2003; Tykocinski et al. 2001, 2005; Hughes 2012). The resistance component refers to the access resistance which depends on the size and type of metal in the electrode contact and lead wire, and the resistivity of the surrounding fluid and tissue in cochlear implants (e.g., perilymph, fibrous tissue, bone; Clark et al. 2003). The reactance component arises from the electrode-tissue interface, involving mechanisms of charge transfer. The first is capacitive, indicating that a capacitor stores electrons ("C" in Fig. 1.4A). The second is the faradic ("Rf" in Fig. 1.4A), which transfers electrons through chemical reactions (Clark, 2004). Electrode impedance measures are incorporated into clinical software by all four manufacturers (i.e., Advanced Bionics, Cochlear, MED-EL and Oticon) (Hughes 2012; Dang et al. 2015). Electrode impedance has been used for some clinical practices, such as identifying the electrode failures, monitoring impedances over time and verifying voltage compliance.

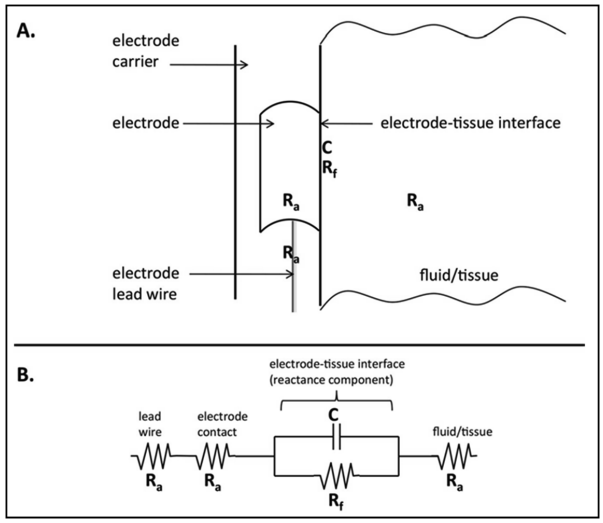

Fig. 1.4 Graphical presentation of the components of electrode impedance. A. Schematic of electrode contact on a carrier. R_a represents the access resistance; C represents the capacitance (reactance component) at the electrode-tissue interface; R_f represents potential faradic resistance. B. Corresponding electrical circuit for panel A. Adapted from Hughes, M. L., (2012) with permission.

EFI represents an intracochlear potential (or impedance) map which is measured by consecutively stimulating each contact from apex to base (e.g., Vanpoucke et al., 2004, 2012; Mens 2007). The intracochlear potential is recorded at all contacts, including the stimulating contact and thereby a picture of the distribution of electrical current in a cochlea is provided. The difference between electrode impedance and EFI recording is that voltages in the EFI mode are recorded across the whole electrode array for each single stimulated electrode pair. For electrode impedance, the voltage across only the stimulated electrode pair is recorded. Previous studies have found that the field distributions may be a feasible measure to evaluate the placement of the electrode array, such as tip fold-over (Vanpoucke et al., 2004, 2012) within the cochlea and the nature of the tissue in the cochlea (e.g., Hughes 2012). However, to date, neither the electrode impedance nor EFI yet has been deployed for the detection of electrode translocation, namely, the shift of an electrode array from the scala tympani to the scala vestibuli through the basilar membrane, which is the most common type of electrode misplacement in patients with CIs

(Finley et al. 2009; Holden et al. 2013).

1.4 Overview of the current thesis

1.4.1 Aims

The research goal of the present thesis is to explore the novel applications of objective measures in cochlear implants. The first aim is to extract the temporal firing properties of excited ANFs underlying eCAPs and examine the possible implications in terms of neural survival and refractory properties of ANFs and, ultimately, speech perception. To do this, a deconvolution model of neural responses to electrical stimulation of the ANFs was developed. The second aim of this thesis is to develop a novel tool to detect translocations of the electrode array using EFI recordings.

1.4.2 Outline of the current thesis

In **chapter 2** we propose an iterative deconvolution model for estimating the human evoked unitary response (UR) and then extract the temporal firing properties of ANFs underlying human eCAPs. In **chapter 3**, we validate this iterative deconvolution model using a relatively large data set of human eCAP recordings, consisting of 4982 eCAPs recorded from 111 CI recipients at the Leiden University Medical Center. This validation process encompasses the verification of the estimation of the human UR, the extraction of CDLDs and finding the optimal CDLD model for each eCAP waveform. From the CDLDs the temporal firing properties of excited ANFs underlying the eCAPs can be obtained. To investigate whether the temporal firing properties between children and adults are different, CDLDs derived from the two groups are compared. To further investigate the association between the CDLD extracted from eCAPs and speech perception performance in CI recipients, **chapter 4** conducts a prospective study on a group of 134 adult patients in our center. The relationship between the number and the temporal firing properties of ANFs underlying eCAPs and speech perception is evaluated. **Chapter 5** describes

a retrospective study evaluating to what extent the refractory properties of the short and long-latency components of the eCAP differed from each other and their potential clinical relevance.

In **Chapter 6** we attempt to detect translocation of the Hi-Focus Mid-Scala electrode array (Advanced Bionics, Valencia, CA) using the electrode impedance and access resistances recorded preoperatively in CI recipients.

Finally, **chapter 7** presents an overall discussion and conclusions of the studies reported in this thesis. Practical implications in clinics and future perspectives are presented.

References

Abbas, P. J., & Brown, C. J. (1988). Electrically evoked brainstem potentials in cochlear implant patients with multi-electrode stimulation. Hearing Research, 36, 153–162.

Abbas, P. J. (1993). Electrophysiology. In R. S. Tyler (Ed.), Cochlear Implants: Audiological Foundations. San Diego: Singular Publishing Group.

Abbas, P. J., Brown, C. J., Shallop, J. K., Firszt, J. B., Hughes, M. L., Hong, S. H., & Staller, S. J. (1999). Summary of results using the Nucleus CI24M implant to record the electrically evoked compound action potential. Ear and Hearing, 20, 45–59.

Aschendorff, A., Kromeier, J., Klenzner, T., & Laszig, R. (2007). Quality Control After Insertion of the Nucleus Contour and Contour Advance Electrode in Adults. Ear and Hearing, 28(Supplement), 75S-79S.

Botros, A., & Psarros, C. (2010). Neural Response Telemetry reconsidered: I. The relevance of ECAP threshold profiles and scaled profiles to cochlear implant fitting. Ear and Hearing, 31, 367–379.

Brown, C. J., Abbas, P. J., & Gantz, B. J. (1990). Electrically evoked whole-nerve action potentials I. Data from Symbion cochlear implant users. Journal of the Acoustical Society of America, 88, 1385–1391.

Brown, C. J., Abbas, P. J., Fryauf-Bertschy, H., Kelsay, D., & Gantz, B. J. (1994). Intraoperative and postoperative electrically evoked auditory brainstem responses in Nucleus cochlear implant users: Implications for the fitting process. Ear and Hearing, 15, 168–176.

Brown, C. J., Etler, C., He, S., O'Brien, S., Erenburg, S., Kim, J.-R., Dhuldhoya, A. N., &Abbas, P. J. (2008). The electrically evoked auditory change complex: Preliminary results from Nucleus cochlear implant users. Ear and Hearing, 29, 704–717.

Carlson, M. L., Driscoll, C. L. W., Gifford, R. H., Service, G. J., Tombers, N. M., Hughes-Borst, B. J., Neff, B. A., & Beatty, C. W. (2015). Implications of Minimizing Trauma During Conventional Cochlear Implantation. Journal of Investigative Dermatology, 135(2), 612–615.

Clark, G., & Richter, C. P. (2004). Cochlear Implants: Fundamentals and Applications. Physics Today, 57(11), 66-67.

Cullington, H. E., & Clarke, G. P. (1997). Integrity testing of cochlear implants in the awake child. British Journal of Audiology, 31, 247–256.

de Sauvage, R. C., Aran, J. M., & Erre, J. P. (1987). Mathematical analysis of VIIIth nerve cap with a linearly-fitted experimental unit response. Hearing Research, 29(2–3), 105–115.

De Vos, J. J., Biesheuvel, J. D., Briaire, J. J., Boot, P. S., Van Gendt, M. J., Dekkers, O. M., ... & Frijns, J. H. (2018). Use of electrically evoked compound action potentials for cochlear implant fitting: a systematic review. Ear and hearing, 39(3), 401-411.

Finley, C. C., & Skinner, M. W. (2009). Role of electrode placement as a contributor to variability in cochlear implant outcomes, 29(7), 920–928.

Gantz, B. J., Tyler, R. S., McCabe, B. F., Tye-Murray, N., Lansing, C., Kuk, F., Knutson, J. F., Hinrichs, J., Woodworth, G., Abbas, P., & Brown, C. (1988). Evaluation of five different cochlear implant designs: Audiologic assessment and predictors of performance. In Laryngoscope (Vol. 98, Issue 10, pp. 1100–1106).

Goldstein, M. H., & Kiang, N. Y. S. (1958). Synchrony of Neural Activity in Electric Responses Evoked by Transient Acoustic Stimuli. Jasa, 30(2), 107–114.

Hartmann, R.,& Kral, A. (2004). Central responses to electrical stimulation. In F.-G. Zeng, A. N. Popper, & R. R. Fay (Eds.), Cochlear implants: Auditory prostheses and electric hearing (pp. 213–285). New York, NY: Springer-Verlag.

Holden, L. K., Finley, C. C., Firszt, J. B., Holden, T. A., Brenner, C., Potts, L. G., Gotter, B. D., Vanderhoof, S. S., Mispagel, K., Heydebrand, G., & Skinner, M. W. (2013). Factors Affecting Open-Set Word Recognition in Adults With Cochlear Implants. Ear and Hearing, 34(3), 342–360.

Hughes, M. L. (2012). Objective Measures in Cochlear Implants. Abingdon, SD: PLURAL PUBLISHING.

He, S., Teagle, H. F. B., & Buchman, C. A. (2017). The electrically evoked compound action potential: From laboratory to clinic. Frontiers in Neuroscience, 11(JUN), 1–20.

Kandel, E., R., Schwartz, J. H., Jessell, T. M. (2012), Siegelbaum SA, Hudspeth AJ. 'Principles of Neural Science, 5th ed. McGraw-Hill, New York.ISBN 0-07-139011-1

Kim, J.R., Abbas, P.J., Brown, C.J., Etler, C.P., O'Brien, S. and Kim, L.S. (2010). The relationship between electrically evoked compound action potential and speech perception: a study in cochlear implant users with short electrode array. Otology & neurotology: official publication of the American Otological Society, American Neurotology Society [and] European Academy of Otology and Neurotology, 31(7), p.1041.

Mens, L. H. M. (2007). Advances in Cochlear Implant Telemetry: Evoked Neural Responses, Electrical Field Imaging, and Technical Integrity. Trends in Amplification, 11(3), 143–159.

Micco, A. G., Kraus, N., Koch, D. B., McGee, T. J., Carrell, T. D., Sharma, A., Nicol, T., & Wiet, R. J. (1995). Speech-evoked cognitive P300 potentials in cochlear implant recipients. American Journal of Otology, 16, 514–520.

Miller, C. A., Brown, C. J., Abbas, P. J., & Chi, S.-L. (2008). The clinical application of potentials evoked from the peripheral auditory system. Hearing Research, 242, 184–197.

Oviatt, D. L., & Kileny, P. R. (1991). Auditory event-related potentials elicited from cochlear implant recipients and hearing subjects. American Journal of Audiology, 1, 48–55.

Pickles, J. O. (1988). An introduction to the physiology of hearing (2nd ed.). San Diego, CA: Academic Press.

Rizzolatti, G., & Kalaska, J. F. (2013). Voluntary movement: the parietal and premotor cortex. Principles of neural science, 5, 865-893.

Shannon, R. V. (1983). Multichannel electrical stimulation of the auditory nerve in man: I. Basic psychophysics. Hearing Research, 11, 157–189.

Shepherd, R. K., Clark, G. M., & Black, R. C. (1983). Chronic electrical stimulation of the auditory nerve in cats. Acta Oto-laryngology (Stockholm), 399, 19–31.

Stronks, H. C., Aarts, M. C., & Klis, S. F. (2010). Effects of isoflurane on auditory evoked potentials in the cochlea and brainstem of guinea pigs. Hearing research, 260(1-2), 20-29.

Stypulkowski, P. H., & van den Honert, C. (1984). Physiological properties of the electrically stimulated auditory nerve. I. Compound action potential recordings. Hearing Research, 14, 205–223.

Tykocinski, M., Duan, Y., Tabor, B., & Cowan, R. S. (2001). Chronic electrical stimulation of the auditory nerve using high surface area (HiQ) platinum electrodes, 159.

Tykocinski, M., Cohen, L. T., & Cowan, R. S. (2005). Measurement and analysis of access resistance and polarization impedance in cochlear implant recipients. Otology and Neurotology, 26(5), 948–956.

van Eijl, R. H. M., Buitenhuis, P. J., Stegeman, I., Klis, S. F. L., & Grolman, W. (2017). Systematic review of compound action potentials as predictors for cochlear implant performance. Laryngoscope, 127(2), 476–487.

van den Honert, C., & Stypulkowski, P. H. (1986). Characterization of the electrically evoked auditory brainstem response (ABR) in cats and humans. Hearing Research, 21, 109–126.

Vanpoucke, F. J., Zarowski, A. J., & Peeters, S. A. (2004). Identification of the impedance model of an implanted cochlear prosthesis from intracochlear potential measurements. IEEE Transactions on Biomedical Engineering, 51(12), 2174–2183.

Vanpoucke, F. J., Boermans, P. B. P. B., & Frijns, J. H. (2012). Assessing the placement of a cochlear electrode array by multidimensional scaling. IEEE Transactions on Biomedical Engineering, 59(2), 307–310.

Versnel, H., Prijs, V. F., & Schoonhoven, R. (1992a). Round-window recorded potential of single-fibre

discharge (unit response) in normal and noise-damaged cochleas. Hearing Research, 59(2), 157–170.

Versnel, H., Schoonhoven, R., & Prijs, V. F. (1992b). Single-fibre and whole-nerve responses to clicks as a function of sound intensity in the guinea pig. Hearing Research, 59(2), 138–156. https://doi.org/10.1016/0378-5955(92)90111-Y

Walker, M., Kublin, J. G., & Zunt, J. R. (2009). Effect of stimulus and recording parameters on spatial spread of excitation and masking patterns obtained with the electrically evoked compound action potential in cochlear implants. 42(1), 115–125.

Zeng, F., & Shannon, R. V. (1994). Loudness coding mechanisms inferred from electric stimulation of the human auditory system. Science, 264, 564–56.

Chapter 2

An iterative deconvolution model to extract the temporal firing properties of the auditory nerve fibers in human eCAPs

Yu Dong, H. Christiaan Stronks, Jeroen J. Briaire and Johan H. M. Frijns

MethodsX (2021) 101240

Abstract

The electrically evoked compound action potential (eCAP) has been widely studied for its clinical value for the evaluation of the surviving auditory nerve (AN) cells. However, many unknowns remain about the temporal firing properties of the AN fibers that underlie the eCAP in CI recipients. These temporal properties may contain valuable information about the condition of the AN. Here, we propose an iterative deconvolution model for estimating the human evoked unitary response (UR) and for extracting the compound discharge latency distribution (CDLD) from eCAP recordings, under the assumption that all AN fibers have the same UR. In this model, an eCAP is modeled by convolving a parameterized UR and a parameterized CDLD model. Both the UR and CDLD are optimized with an iterative deconvolution fitting error minimization routine to minimize the error between the modeled eCAP and the recorded eCAP.

- This method first estimates the human UR from eCAP recordings. The human eCAP is unknown at the time of this writing. The UR is subsequently used to extract the underlying temporal neural excitation pattern (the CDLD) that reflects the contributions from individual AN fibers in human eCAPs.
- By calculating the CDLD, the synchronicity of AN fibers can be evaluated.

Keywords: Cochlear implants, sensorineural hearing loss, electrically evoked compound action potential; deconvolution, unitary response, temporal properties

2.1 Background

A cochlear implant (CI) is an intracochlear device that can restore hearing with direct electrical stimulation of the auditory nerve (AN). A CI can also be applied to measure electrically evoked AN responses using the reverse telemetry function. Typically, AN activity is evoked with short electrical pulses, and the response comprises the superposition of many action potentials from AN fibers over time. This response is called the electrically evoked compound action potential (eCAP). To date, single-fiber action potentials have not been recorded from the human AN.

ECAP recordings can provide information on the amplitude and latency of the evoked compound AN response, but they do not provide information about the underlying excitation patterns of individual AN fibers. Clinically, the eCAP is typically evaluated by examining the main peaks of the eCAP; i.e., the first negative peak (N1) and the first positive peak (P1) (Lai and Diller, 2000; Stypulkowski & van den Honert,1984). Previously, animal studies have reported that the eCAP waveform was dependent on both the number of action potentials and the degree of synchronicity in the AN fiber population (Versnel et al., 1992; Stypulkowski & van den Honert,1984; van den Honert & Stypulkowski, 1984). The temporal firing properties in eCAPs can potentially reflect additional, valuable information, such as the survival of AN fibers (Strahl et al., 2016; Stypulkowski & van den Honert,1984). However, extracting the temporal firing properties of single fibers directly from the eCAP is mathematically complex. As a result, these properties are often overlooked (Khan et al., 2005; Fayad et al., 2006; Ramekers et al., 2014; Seyyedi et al., 2017). Here we propose a method to extract the temporal firing properties of the AN fibers in eCAPs. The procedure is based on the findings of our previous study (Dong et al., 2020).

The action potential generated by a single fiber can be registered by a recording electrode and is called the unitary response (UR). The UR is generally thought to be constant, and all URs are assumed to contribute equally to the acoustically evoked CAP (Goldstein et al., 1958; Versnel et al., 1992). We assume this concept also holds for eCAPs (Strahl et al., 2016; van Gendt et al., 2019; Dong et al., 2020) because the eCAP also represents a superposition of a series of action potentials from individual AN fibers in response to an electric stimulus over time. Thus, based on these assumptions, we describe the eCAP as the convolution of many URs with a compound discharge latency distribution (CDLD), according to Eq. 2.1 (see also Fig. 2.1):

$$\mathrm{eCAP}(t) = \int_{-\infty}^{t} \mathrm{CDLD}(\tau) * \mathrm{UR}(t-\tau)\, d\tau \tag{2.1}$$

Here, the CDLD is the probability density function, *t* is time, and $\boldsymbol{\tau}$ is the variable of integration. The CDLD weighs all URs of each excited AN fiber across time and reflects the neural

synchronicity (i.e., the temporal properties). Thus, the temporal firing properties of the AN fibers in eCAPs can be captured from the CDLDs. Mathematically, the CDLD cannot assume negative values, and the area under a CDLD curve reflects the number of excited AN fibers.

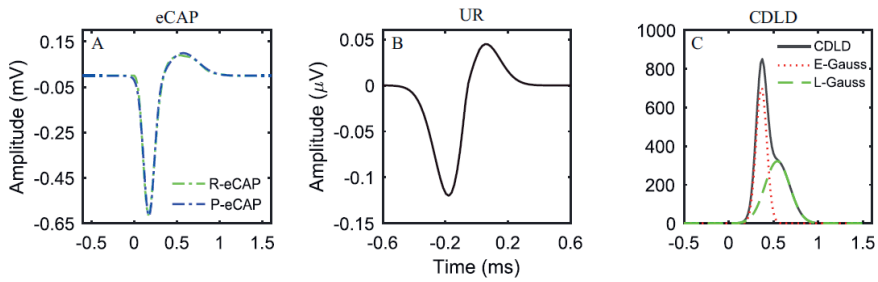

Fig.2. 1. An example of the deconvolution model. (A) According to Eq. 2.1, the recorded electrically evoked compound action potential (R-eCAP, green interrupted line) was predicted (P-eCAP, blue interrupted line) with the convolution of (B) a UR model (also see Eq. 2.3) and (C) a compound discharge latency distribution (CDLD) model (blue line, see Eq. 2.4), by implementing the deconvolution fitting error minimization routine. The CDLD model consists of two Gaussian components: the early Gaussian component (E-Gauss, red dotted line) and the late Gaussian component (L-Gauss, green dashed line).

The only study on the human CDLD was conducted by Strahl et al. (2016). They predicted the CDLD by a direct deconvolution of the human eCAP using the guinea pig UR (UR_{gp}) (Strahl et al., 2016). The deconvolution was performed with Eq. (2.2):

$$\mathrm{CDLD(t)} = \mathrm{F}^{-1}[\frac{\mathrm{F(eCAP(t))}}{\mathrm{F(UR(t))}}] \tag{2.2}$$

Here, *t* is time, *F* represents the Fourier transform, and $\boldsymbol{F^{-1}}$ represents the inverse Fourier transform. Strahl et al. observed a CDLD with two Gaussian components, which could be attributed to two separate groups of neural responses. However, when we reproduced their method on human patient data (see details in Dong et al., 2020) we obtained unrealistic CDLDs because they contained negative phases and high-frequency components. To suppress these negative phases and high-frequency components, Strahl et al. filtered the CDLD with a 2.5 kHz low-pass filter and shifted the CDLD upward. However, this post-processing might have

compromised the validity of the CDLD in its ability to reflect the temporal firing properties of the AN.

To facilitate a direct deconvolution of the human eCAP into a CDLD to describe the temporal firing properties of AN fibers underlying the eCAP, Strahl et al. used the UR_{gp}, because the human UR (UR_h) was, and still is unknown. However, there are several anatomical differences between the two species that potentially can affect the shape of the UR. There are differences in the size and shape of the cochlea (Nadol et al., 1988; Dong et al., 2020) and the spiral ganglion cell body is myelinated in guinea pigs, but not in humans (Rask-Andersen et al., 2015). Moreover, eCAP recordings in humans are usually performed at intracochlear sites, e.g., Strahl et al., 2016; van Gendt et al., 2019; Dong et al., 2020, whereas the UR_{gp} used in Strahl et al. (2016) was recorded at the round window niche (Versnel et al., 1992). The application of a direct deconvolution of the human eCAP into a CDLD using the UR_{gp} can thus be expected to yield a less valid CDLD.

To overcome these problems we propose an iterative deconvolution model to simulate the deconvolution computation. The recorded eCAPs are entered as input for this model to obtain the UR_h and the corresponding CDLDs. This model consists of a two-step procedure (Fig. 2.2). It estimates the UR_h in step one (Fig. 2.2A) and derives the temporal firing properties of AN fibers underlying the eCAP in step two (Fig. 2.2B), without the need for any post-processing of the CDLD. In both steps, an eCAP is modeled by convolving a UR model with a CDLD model. Then, the modeled eCAP is optimized by iteratively adjusting the variables in the parameterized UR and CDLD models, until the modeled eCAP matches the recorded eCAPs. In step one, the descriptive parameters of both the UR and CDLD model are variable. After optimization, an estimate of the UR_h and CDLD is obtained for each eCAP waveform available. A unified UR_h is subsequently estimated by averaging the available collection of individual UR_hs (Fig. 2.2A). Using the unified UR_h obtained in step one, a similar procedure is used in step two where only the CDLD parameters are iteratively varied (Fig. 2.2B). The resulting CDLDs can reveal the temporal firing properties of AN. More detailed information about the deconvolution model is

given in the below sections.

2.2 Model Construction

2.2.1 Construction of the UR and CDLD

According to Eq. 2.1, the UR and the CDLD are required to simulate the recorded eCAPs. At present, the UR_h has not been described with electrophysiological recordings. Because the UR_h might be different from the UR_{gp} (Nadol et al., 1988) or other animals, it is preferable to estimate the UR_h (Dong et al., 2020). As a starting point, we used the UR_{gp} function reported in Versnel et al. (1992) to estimate the UR_h. For this purpose, the UR was parameterized as shown in Eq. (2.3).

$$\mathrm{UR_p}(t) = \frac{U}{\sigma}(t - t_0)e^{[-\frac{(t-t_0)^2}{2\sigma^2}]} \tag{2.3}$$

The UR model consists of a negative (N) and positive (P) phase; the transition point between the negative component and the positive component is defined as $\boldsymbol{t_0}$. Hence, for $t < \boldsymbol{t_0}$, the magnitude, U (V), of the negative peak is $\boldsymbol{U_N}$, and the width, σ (sec), of the negative component is $\boldsymbol{\sigma_N}$; and for $t > \boldsymbol{t_0}$, the magnitude of the positive peak is $\boldsymbol{U_P}$ and the width of the positive component is $\boldsymbol{\sigma_P}$. Boundary limits for the variables in Eq. 2.3 are introduced to constrain the solutions (see details in step one, Fig. 2.2).

Earlier studies have observed eCAPs with two positive peaks, which might originate from two separate groups of neural responses (Stypulkowski & van den Honert,1984; Lai & Dillier 2000). Consistent with Strahl et al. (2016) our method implements a parameterization of the CDLD with a mixture of two Gaussian components, as shown in Eq. (2.4) (also see Fig. 2.1C).

$$\mathrm{CDLD_p} = \alpha_1 * \mathrm{N}(\mu_1, \sigma_1) + \alpha_2 * \mathrm{N}(\mu_2, \sigma_2) \tag{2.4}$$

where N is a Gaussian distribution; the variables $\boldsymbol{\alpha_1}, \mu_1$ and $\boldsymbol{\sigma_1}$ belong to the early Gaussian component (in time), and the variables, $\boldsymbol{\alpha_2}, \mu_2$ and $\boldsymbol{\sigma_2}$ belong to the late Gaussian component.

The variables $\boldsymbol{\alpha_1}$ and $\boldsymbol{\alpha_2}$ represent the peak amplitudes; $\mu_1$and μ_2 are the peak latencies; and $\boldsymbol{\sigma_1}$ and $\boldsymbol{\sigma_2}$ represent the peak widths. Similar to Eq. 2.3, boundary limits for the variables in Eq. 2.4 are set to constrain the solutions (see details in step one and two, Fig. 2.2). Details are given below.

2.2.2 Optimization routine

The procedure described here involves the application of a deconvolution fitting error minimization routine (DMR) in step one and two. The parameterized UR model (UR_p, Eq. 2.3) and the parameterized CDLD model ($CDLD_p$, Eq. 2.4) are used to predict a recorded eCAP waveform using indirect deconvolution. This indirect procedure uses a convolution step to estimate UR_h and CDLD by implementing DMR to optimize the match between $eCAP_p$ and the recorded eCAP. The initial values and boundary limits of the UR_p and $CDLD_p$ parameters must be assigned for the DMR to run. Then, the $eCAP_p$ and the baseline-corrected eCAP ($eCAP_c$) (see details in the next section), initial values and boundary limits of the UR_p and $CDLD_p$ parameters are used as input into the DMR. The DMR iteratively manipulates the parameters of the UR_p and the $CDLD_p$ in step one (Fig. 2.2A), or only the $CDLD_p$ in step two (Fig. 2.2B) within the boundary limits to minimize the fitting error (see Fig. 2.2) with the lsqcurvefit function provided in MATLAB (Mathworks 2016a, Natick, MA, USA). The fitting error refers to the difference between the $eCAP_p$ and the $eCAP_c$. Accordingly, the $eCAP_p$ gradually converges to the $eCAP_c$. When the fitting error reaches the minimum value (i.e., the $eCAP_p$ optimally approximates the $eCAP_c$), the DMR outputs the values of the UR_p and $CDLD_p$ parameters. With these values, the UR and CDLD (step one) and subsequently the final CDLD estimate (step two) can be generated. The MATLAB script of this DMR is attached in the supplementary material of this publication.

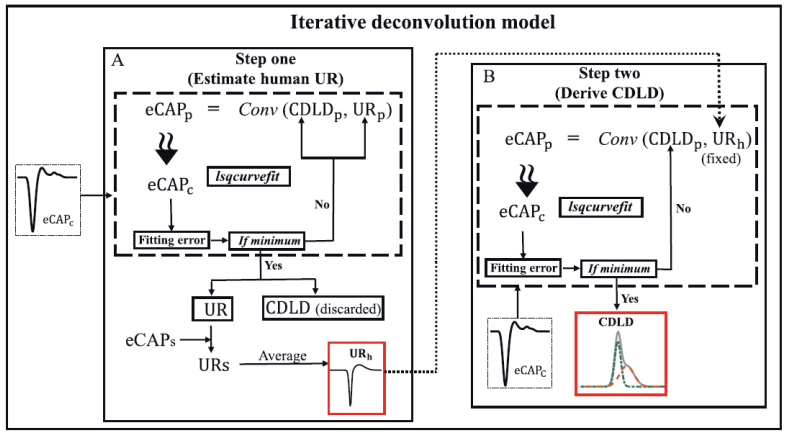

Fig. 2.2. Iterative deconvolution model workflow. The recorded electrically evoked action potential (eCAP) waveforms are pre-processed and used as the input for the deconvolution fitting error minimization routine (DMR, enclosed in the dashed square) in both step one and step two. This DMR is conducted by the lsqcurvefit function provided in MATLAB. In the DMR, the predicted eCAP ($eCAP_P$) is calculated by the convolution of the parameterized unitary response (UR) model (UR_p) with the parameterized compound discharge latency distribution (CDLD) model ($CDLD_p$). (A) In step one, both the UR_p and the $CDLD_p$ are optimized with the DMR to achieve an approximate match between the $eCAP_P$ and the baseline-corrected ($eCAP_C$). When the fitting error (i.e., the difference between the $eCAP_P$ and the $eCAP_C$) reaches the minimum, the UR and CDLD are obtained. In this step, each eCAP generates a UR. The URs are obtained from a series of eCAPs, and the average of these URs is defined as the human UR (UR_h, enclosed in the red square). (B) In step two, the UR_h is fixed, and only the $CDLD_p$ is iteratively adjusted with the DMR to generate the best fitting CDLD for each individual eCAP (CDLD, enclosed in the red square). Conv represents the convolution function in MATLAB.

2.2.3 Extraction of temporal AN firing properties from eCAPs

In this section, we will describe the workflow to calculate the CDLD from recorded eCAP waveforms. Before any analysis can be performed, the raw eCAP waveforms have to be pre-processed. First, a baseline correction is carried out. The eCAP tail can be used to determine the baseline, because neural responses and any remaining artifacts are not expected to be present in this part of the eCAP waveform. At approximately 1.5 ms after stimulus artifact a reliable baseline estimate can be obtained (de Sauvage et al., 1987; Dong et al., 2020). The baseline correction is performed by subtracting the average amplitude of the tail section from the eCAP

waveform. In addition, we have observed that performing a convolution on a finite-length signal typically introduces distortions at the leading and trailing ends of the signal. To prevent distortion of the eCAP waveforms, signal extensions can be deployed (Esfandiari & Bei 2018) by adding 50 samples to the start and end of each waveform. This is realized by performing a linear extrapolation to baseline. This extrapolation only affects the CDLD before and after the recording window (Versnel et al., 1992; Dong et al., 2020; Esfandiari & Bei 2018).

The two steps proposed for deriving the temporal firing properties of the AN from eCAPs are shown in Fig. 2.2. Before the CDLD can be determined, the UR_h has to be estimated from the available eCAP dataset with the DMR (Fig. 2.2A). In step one (Fig. 2.2A), the parameters of both the UR_p (Eq. 2.3) and the $CDLD_p$ (Eq. 2.4) are variable and will be optimized by the DMR. This ensures that the $eCAP_p$ optimally matches the baseline-corrected eCAP ($eCAP_c$). After the last iteration, the UR and CDLD of the optimal $eCAP_p$ are derived. In our data set Dong et al., 2020 a series of eCAPs were recorded at different electrode contacts with different stimulus levels from different subjects. According to the assumption that the UR is identical in all contributing AN fibers and across electrode contacts, stimulus levels and subjects (Strahl et al., 2016; van Gendt et al., 2019; Dong et al., 2020), a representative human UR can be estimated by averaging all these URs obtained from a series of eCAPs. The UR model and the CDLD model can interact freely in step one; thus, the temporal firing properties can be manifested in both the UR and the CDLD. Consequently, the resulting CDLDs do not accurately reflect the temporal information in eCAPs and these CDLDs are discarded and re-calculated by using a constant UR, as outlined below.

As mentioned in the Model Construction section, the initial values and boundary limits of the parameters have to be assigned before performing the DMR. Because the UR_h and UR_{gp} are expected to be similar (Briaire & Frijns 2005), we used the morphological parameters of the UR_{gp} as a reference for the UR_h (Versnel et al., 1992). Accordingly, the UR and CDLD outcomes were constrained with the following domain values Dong et al., 2020: U_N [0.02, 0.25], σ_N [0.02, 0.13], U_P [0, 0.12], σ_P [0.08, 0.25], t_0 [-0.25, 0.06], α_1 [0, 0.35], μ_1 [0.04, 1.3], σ_1

[0, 0.3], α_2 [0, 0.35], μ_2 [0.04, 1.3], σ_2 [0, 0.3]. Based on the parameters of UR_{gp}, the initial starting values of the DMR parameters are set to: U_N (0.12), σ_N (0.045), U_P (0.06), σ_P (0.12), t_0 (-0.06), α_1 (0.08), μ_1 (0.38), σ_1 (0.06), α_2 (0.05), μ_2 (0.5), σ_2 (0.14). Then, the parameters of the UR model (Eq. 2.3) and the CDLD model (Eq. 2.4) are iteratively manipulated simultaneously with the DMR, until they approximate the recorded eCAPs (Fig. 2.1, green line).

Setting appropriate starting values and boundaries for the DMR parameters is necessary, both to obtain a realistic UR_h and CDLD with the DMR and to converge to an optimal $eCAP_p$. An important factor to consider when setting the starting values and boundaries for the DMR parameters is the morphology of eCAP recordings, particularly the eCAP waveforms that have the maximal and minimal amplitudes in one's dataset. The morphological characteristics of eCAPs include, but are not limited to the main peak (i.e., the N1 and P1) and, maybe, a second peak (i.e., the N2 and P2) and the corresponding peak latencies (Stypulkowski & van den Honert, 1984; Dong et al., 2020). These parameters are influenced by extrinsic factors, including the stimulation level, intra-cochlear test electrode location, the separation between the stimulating and recording electrodes, stimulus polarity, artifact reduction methods, and implant designs (Ramekers et al., 2014; Stypulkowski & van den Honert, 1984). For instance, a larger eCAP main peak would most likely require wider boundaries for α_1 and α_2, and longer peak latencies would require wider boundaries for μ_1 and μ_2. Moreover, because the parameter estimates are sensitive to the initial values of the DMR parameters, they should be optimized manually, when needed, to achieve an adequate fit. The goodness of fit to overall data was evaluated by calculating the normalized root mean square error (NRMSE). Therefore, the initial values and boundaries might need to be optimized with different datasets. In Dong et al. (2020), the parameters of human UR were estimated: U_N = 0.155 μV, σ_N = 0.038 ms, U_P = 0.022 μV, σ_P = 0.155 ms, t_0 = -0.128. For the human dataset, this UR can be used directly for step two. Nevertheless, we strongly recommend that researchers should examine the consistency of human UR when using their own datasets.

In step two (Fig. 2.2B), the temporal firing properties of the AN in human eCAPs are extracted by calculating CDLDs (Fig. 2.2B). Due to the interaction between the UR_h and CDLD (see above), the CDLD calculation with the DMR must use a constant UR_h. With the fixed UR obtained in step one, the DMR can only adjust the parameters of the CDLD model (Eq. 2.3), with the recorded eCAPs as input. Consequently, because the fixed UR_h and CDLD model can no longer interact, all the temporal firing properties in eCAPs are driven into CDLDs. Thus, these CDLDs validly reflect the temporal firing properties in the eCAPs. Similar to step one, we constrain the domains for the variables in the CDLD model with the following values: α_1 [0, 0.35], μ_1 [0.15, 1.35], σ_1 [0, 0.45], α_2 [0, 0.35], μ_2 [0.15, 1.35], σ_2 [0, 0.45]. The starting values of the DMR parameters were set as follows: α_1 (0.08), μ_1 (0.59), σ_1 (0.06), α_2 (0.05), μ_2 (0.6), σ_2 (0.14). The combined boundary limits of these variables allow the model to produce CDLDs without negative phases; thus, unrealistic CDLDs can be avoided without any post-processing. Similar to step one, the starting values and the boundary limits for the CDLD parameters in Eq. 2.4 can be optimized manually, when needed, to achieve an adequate fit according to the morphology of eCAPs in different datasets.

2.3 Method validation

The validation of the method was discussed in detail in our previous study (Dong et al., 2020). In that study, the model presented here was applied to a relatively large data set of human eCAP growth function recordings. This data set consisted of 4982 eCAPs from 111 CI recipients who received a HiRes90K device (Advanced Bionics, Valencia, CA), either with a 1J or a Mid-Scala electrode array. The eCAPs were recorded measured on eight odd electrode contacts with stimulus levels from 50 to 500 current unit. We have validated both steps of the method.

First, we validated step one, namely the estimation of the UR_h, by comparing the resulting $eCAP_p$s obtained with our estimated UR_h (Dong et al., 2020) to the $eCAP_p$s obtained with UR_{gp} (Versnel et al., 1992) in step two. Based on the goodness of fit measure (NRMSE, the normalized root mean square error provided in MATLAB), the eCAPs achieved with UR_h were better than

those achieved with UR_{gp} (Dong et al., 2020). The UR_h reduced the fitting error for all eCAPs by approximately 18%. This result supported our assumption that the UR of human AN fibers differs from the UR_{gp} (Versnel et al., 1992). The assumption that the UR is constant may be contested, as it can hypothetically vary across subjects, electrodes and/or current levels. However, the assumption of UR constancy is necessary, because a fixed UR is needed to optimize the derivation of CDLD in step two. As such, the UR is used solely as a necessary intermediate step to extract a valid CDLD from the eCAP. While a fixed UR is necessary and sufficient for our goal, our deconvolution model can nonetheless be used to investigate whether the UR differs across subjects or different stimulus conditions by running the deconvolution model for each condition separately. However, to more conclusively resolve such questions, direct recordings of the UR_h are necessary.

Second, we validated the extraction of the CDLD with the fixed UR by evaluating the goodness of fit of the predicted eCAPs. In general, 93.6% of the recorded eCAPs were predicted accurately, with a >0.9 goodness of fit (NRMSE). Thus, these CDLDs provided a good picture of the temporal firing properties of the AN fibers in eCAPs. Importantly, realistic CDLDs were obtained that lacked any negative phases without any post-processing. The remaining 322 eCAPs had deviant waveforms, with relatively small N1 peaks and large P1 peaks; thus, they could not be predicted well with our model (NRMSE <0.9). This may have been caused by the use of a fixed UR that was based on the group-average. This unified UR consisted of a large negative phase and a small positive phase, with a strictly positive CDLD. A UR with this shape could not be used to model the deviant eCAP waveforms with the DMR method (for details, see Dong et al., 2020). However, those cases were fairly rare (6.4%).

Third, we validated the assumption that the CDLD model with two Gaussian components was the optimal model. We designed alternative CDLD models with 1-6 Gaussian components and simulated the recorded eCAPs with the DMR. When the number of Gaussian components increased from 1 to 2, the fitting error diminished substantially (by 78%). When the number of Gaussian components rose from 2 to 6, the fitting outcome remained fairly similar and showed

little benefit (error reduced by 7.6%; see Figure 2.7 in Dong et al., 2020). This result was consistent with the finding of Strahl et al. (2016), who also observed CDLDs with two Gaussian components. Taken together, these validations demonstrated that our method can validly unravel the temporal firing properties of the human AN fibers in eCAPs.

2.4 Conclusion

This study proposes an indirect iterative deconvolution model that provides an estimation of the human UR and derives the underlying neural excitation pattern that reflects the contributions from individual AN fibers to human eCAPs. The observed CDLD with two Gaussian components can be attributed to two separate neural response components, which cannot be easily identified in the raw eCAP waveforms.

References

Briaire, J. J., & Frijns, J. H. M. (2005). Unraveling the electrically evoked compound action potential. *Hearing Research*, *205*(1–2), 143–156.

de Sauvage, R. C., Aran, J. M., & Erre, J. P. (1987). Mathematical analysis of VIIIth nerve cap with a linearly-fitted experimental unit response. *Hearing Research*, *29*(2–3), 105–115.

Dong, Y., Briaire, J. J., Biesheuvel, J. D., Stronks, H. C., & Frijns, J. H. M. (2020). Unravelling the Temporal Properties of Human eCAPs through an Iterative Deconvolution Model. *Hearing Research*, *395*, 108037.

Fayad, J. N., & Linthicum, F. H. (2006). Multichannel cochlear implants: Relation of histopathology to performance. *Laryngoscope*, *116*(8), 1310–1320.

Goldstein, M. H., & Kiang, N. Y. S. (1958). Synchrony of Neural Activity in Electric Responses Evoked by Transient Acoustic Stimuli. *Jasa*, *30*(2), 107–114.

Khan, A. M., Whiten, D. M., Nadol, J. B., & Eddington, D. K. (2005). Histopathology of human cochlear implants: Correlation of psychophysical and anatomical measures. *Hearing Research*, *205*(1–2), 83–93.

Mohammad Seyyedi, Lucas M Viana, & Nadol, J. B. (2016). Within-Subject Comparison of Word Recognition and Spiral Ganglion Cell Count in Bilateral Cochlear Implant Recipients Mohammad. *Physiology & Behavior*, *176*(1), 139–148.

Nadol, J. B. (1988). Comparative anatomy of the cochlea and auditory nerve in mammals. *Hearing Research*, *34*(3), 253–266.

Ramekers, D., Versnel, H., Strahl, S. B., Smeets, E. M., Klis, S. F. L., & Grolman, W. (2014). Auditory-nerve responses to varied inter-phase gap and phase duration of the electric pulse stimulus as predictors for neuronal degeneration. *JARO - Journal of the Association for Research in Otolaryngology*, *15*(2), 187–202.

Rask-Andersen, H., & Liu, W. (2015). Auditory nerve preservation and regeneration in man: Relevance for cochlear implantation. *Neural Regeneration Research*, *10*(5), 710–712.

Strahl, S. B., Ramekers, D., Marjolijn M. B. Nagelkerke, K. E. S., Spitzer, P., Klis, S. F. L., Grolman, W., & Versnel, H. (2016). Assessing the Firing Properties of the Electrically Stimulated Auditory Nerve Using a Convolution Model. *Adv Exp Med Biol*, *894*.

Stypulkowski, P. H., & van den Honert, C. (1984). Physiological properties of the electrically stimulated auditory nerve. I. Compound action potential recordings. *Hearing Research*, *14*(3), 205–223.

van den Honert, C., & Stypulkowski, P. H. (1984). Physiological properties of the electrically stimulated auditory nerve. II. Single fiber recordings. *Hearing Research*, *14*(3), 225–243.

van Gendt, M. J., Briaire, J. J., & Frijns, J. H. M. (2019). Effect of neural adaptation and degeneration on pulse-train ECAPs: A model study. *Hearing Research*, *377*, 167–178.

Versnel, H., Prijs, V. F., & Schoonhoven, R. (1992). Round-window recorded potential of single-fibre discharge (unit response) in normal and noise-damaged cochleas. *Hearing Research*, *59*(2), 157–170.

Wai Kong Lai, & Dillier, N. (2000). A simple two-component model of the electrically evoked compound action potential in the human cochlea. *Audiology and Neuro-Otology*, *5*(6), 333–345.

Whiten, D. M. (Darren M. (2007). Electro-anatomical models of the cochlear implant.

Chapter 3

Unravelling the Temporal Properties of Human eCAPs through an Iterative Deconvolution Model

Yu Dong, Jeroen J. Briaire, Jan Dirk Biesheuvel, H. Christiaan Stronks and Johan H. M. Frijns

Hearing Research 395 (2020) 108037

Abstract

Objective: The electrically evoked compound action potential (eCAP) has been widely studied for its clinical value in evaluating cochlear implants (CIs). However, to date, single-fiber recordings have not been recorded from the human auditory nerve, and many unknowns remain about the firing properties that underlie the eCAP in patients with CIs. In particular, the temporal properties of auditory nerve fiber firing might contain valuable information that may be used to estimate the condition of the surviving auditory nerve fibers. This study aimed to evaluate the temporal properties of neural firing underlying human eCAPs with a new deconvolution model.

Design: Assuming that each auditory nerve fiber produces the same unitary response (UR), the eCAP can be seen as a convolution of a UR with a compound discharge latency distribution (CDLD). We developed an iterative deconvolution model that derived a two-component Gaussian CDLD and a UR from recorded eCAPs. The choices were based on a deconvolution fitting error minimization routine (DMR). The DMR iteratively minimized the error between the recorded human eCAPs and the eCAPs simulated by the convolution of a parameterised UR and CDLD model (instead of directly deconvolving recorded eCAPs). Our new deconvolution model included two separate steps. In step one, the underlying URs of all eCAPs were derived, and the average of these URs was called the human UR. In step two, the CDLD was obtained by using the DMR in combination with the estimated human UR. With this model, we investigated the temporal firing properties of eCAPs by analysing the CDLDs, including the amplitudes, widths, peak latencies, and areas of CDLDs. The differences of the temporal properties in eCAPs between children and adults were explored. Finally, we validated the two-Gaussian component CDLD model with a multiple-Gaussian component CDLD model.

Results: The estimated human UR contained a sharper, narrower negative component and a wider positive phase, compared to the previously described guinea pig UR. Furthermore, the eCAPs from humans could be predicted by the convolution of the human UR with a two-Gaussian component CDLD. The areas under CDLD (AUCD) reflected the number of excited

nerve fibers over time. Both the CDLD magnitudes and AUCDs were significantly correlated with the eCAP amplitudes. Furthermore, different eCAPs with the same amplitude could lead to greatly different AUCDs. Significant differences of the temporal properties of eCAPs between children and adults were found. At last, the two-Gaussian component CDLD model was validated as the most optimal CDLD model.

Conclusion: This study described an iterative method that deconvolved human eCAPs into CDLDs, under the assumption that auditory nerve fibers had the same electrically evoked UR. Based on human eCAPs, we found a human UR that was different from the guinea pig UR. Furthermore, we found that CDLD characteristics revealed age-related temporal differences between human eCAPs. This temporal information may contain valuable clinical information on the survival and function of auditory nerve fibers. In turn, the surviving nerve condition might have prognostic value for speech outcomes in patients with CIs.

Key words: Cochlear implants; Sensorineural hearing loss; eCAPs; Deconvolution; Unitary response; Temporal properties

3.1. Introduction

A cochlear implant (CI) is a device that restores hearing by directly applying electrical stimulation to the auditory nerve fibers inside the cochlea. A CI can also be used to record auditory nerve activity via a telemetry function; this recording yields the electrically evoked compound action potential (eCAP). The eCAP is an objective measure that can be used to assess the quality of the electrode-nerve interface (Zhu et al., 2002; Miller et al., 2008; Botros and Psarros, 2010) and the physiological status of the auditory nerve (Ramekers et al., 2014; Strahl at al., 2016). Clinically, the eCAP is generally evaluated by examining the main peaks, namely the first negative peak (N1) and the first positive peak (P1) (Stypulkowski and van den Honert, 1984; Lai and Dillier, 2000; Abbas et al., 1999; Kim et al., 2010; Alvarez et al., 2011, He et al., 2017). However, the temporal properties of the eCAP are often overlooked. It has been shown that the acoustically evoked compound action potential (CAP) amplitude was linearly correlated

with the number of activated nerve fibers (Goldstein and Kiang, 1958; Versnel et al., 1992a). It is generally assumed that the neural response of each single nerve fiber, called the unitary response (UR), is constant and that all URs contribute equally to the CAP (Goldstein and Kiang, 1958; Prijs, 1985; Versnel et al., 1992a). In this study, we assume that this unitary response concept also holds for the eCAPs (e.g., van Gendt et al., 2019), since the eCAP is the superposition of many action potentials from individual auditory nerve fibers in response to an electric stimulus over time. Hence, the eCAP can be described as the convolution of a UR with a compound discharge latency distribution (CDLD), according to equation (3.1):

$$\mathrm{eCAP}(t) = \int_{-\infty}^{t} \mathrm{CDLD}(\tau) * \mathrm{UR}(t-\tau)\, d\tau \tag{3.1}$$

where t is time, CDLD is a probability density function, and τ is the variable of integration. The CDLD weights all URs of each excited nerve fiber over time, and it reflects the synchronicity (i.e., the temporal properties) of the excited nerve fibers. The area under the CDLD (AUCD) indicates the exact number of excited fibers.

The temporal information contained in the CDLD can potentially reflect additional, valuable information that the eCAP amplitude does not show directly. For instance, in patients with CIs, speech perception has been related to auditory nerve fiber survival and function and the number of spiral ganglion cells (Khan et al., 2005; Fayad and Linthicum, 2006; Ramekers et al., 2014; Seyyedi et al., 2014). Consequently, the AUCD might serve as a predictor of the survival and function of auditory nerves. Additionally, the CDLD can be used to study the mechanisms underlying the double peaks in eCAPs (Stypulkowski and van den Honert, 1984; van de Heyning et al., 2016). In these double-peaked eCAPs, the identity of the firing neuron population remains unclear; i.e., it remains unknown whether each peak represents a distinct population or both peaks are evoked by the same group of neurons.

Several studies have reported that there is a relationship between acoustically evoked CAPs and the underlying single fiber discharge patterns. This relationship was found in CAPs recorded in guinea pigs with the convolution model given in equation 3.1 (e.g., Wang, 1979; Dolan et al.,

1983). From those recordings, the UR of guinea pigs was derived (Versnel et al. 1992a, 1992b, see also Fig. 3.1). In some studies, the inverse problem was studied; i.e., predicting the firing properties by directly deconvolving CAPs and eCAPs with a known UR (Charlet de Sauvage et al., 1987; Strahl et al., 2016). In the study by Strahl et al., this method was applied to investigate the CDLD of human eCAPs with the guinea pig UR, and a two-Gaussian component CDLD was derived. When we reproduced their method on human patient data, we found a physiologically unrealistic CDLD, with negative phases and sharp peaks (Fig. 3.2). Strahl et al. (2016) corrected the negative phases and the high-frequency components by filtering and shifting the CDLD. However, the collective URs that contribute to the eCAP dictate that the CDLD starts after the onset of the electric stimulus. Therefore, the CDLD should be strictly zero before the onset of the stimulus and positive after its onset. Alternatively, it would be better to improve the deconvolution model to obviate the need to post-process the CDLDs.

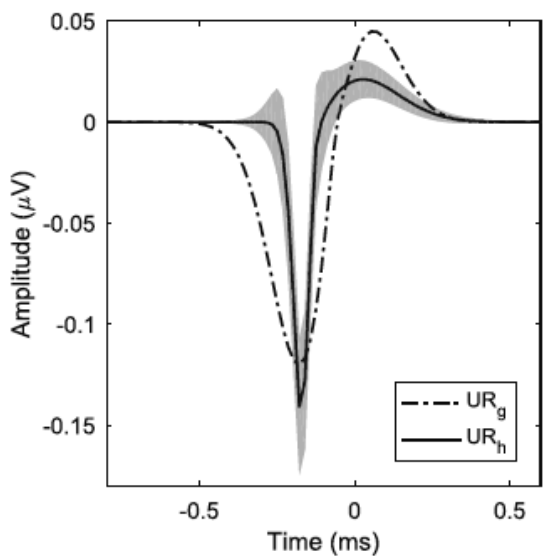

Fig. 3.1 The unitary responses derived from human eCAPs (UR_h) and recorded from guinea pig auditory single nerve fibers (UR_g). The UR_g is plotted in blue, and the UR_h (obtained in the present study) is plotted in green. The shaded area indicates the error bars (standard deviation).

Here, we present an iterative method to model the deconvolution computation. In this method, an eCAP, calculated by convoluting a UR model and a two-Gaussian component CDLD model,

was optimized to match a recorded eCAP by minimizing the fitting error. The recorded eCAPs were used as input for this iterative method to obtain the UR and CDLDs. Based on this method, two steps were performed to investigate the temporal information in human eCAPs: in the first step, human UR was investigated; in the second step, the two-Gaussian component CDLDs were derived. Some studies reported that the eCAP amplitude has a proportional relationship with the number of excited nerve fibers (e.g., Versnel et al., 1992a; Miller et al., 1998, 1999). However, the synchronicity of the excited nerve fibers could also affect the eCAP amplitude. In comparison to the eCAP amplitude, the AUCD, however, can more accurately reflect the number of the excited nerve fibers and give information on the synchronicity of the excited nerve fibers. Thus, we investigated whether the AUCD rises proportionally with the eCAP amplitude. The differences of the temporal information in eCAPs between children and adults were investigated. After the derivation of this CDLD model of Strahl et al. (2016), we further explored the optimal number of Gaussian components to parameterize the CDLD. To this end, we designed a multiple-Gaussian component CDLD model for predicting recorded eCAPs, and we varied the number of components.

Accordingly, in this study, we aimed to develop an iterative deconvolution model that did not depend on any CDLD post-processing to explore the temporal information contained in human eCAPs.

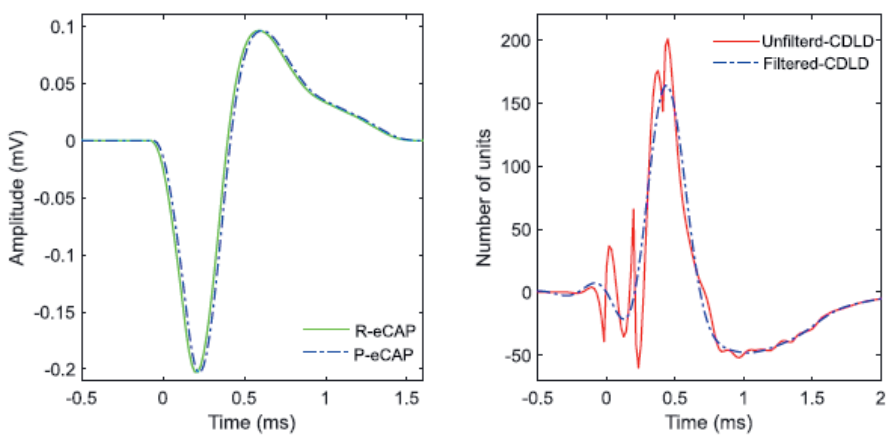

Fig. 3.2 Direct deconvolution of one example of an electrically evoked compound action potential (eCAP) with Strahl's direct deconvolution model. (Left) The recorded eCAP (R-eCAP, grey dashed line) and the corresponding predicted eCAP (P-eCAP, blue line). (Right) The compound discharge latency distribution (CDLD) that resulted from the direct deconvolution of this eCAP. Both the filtered (blue) and unfiltered (red) CDLDs are shown.

3.2. Materials and methods

3.2.1. Patients and recordings

The eCAPs used in this study were obtained intraoperatively from 111 patients that had undergone CI implantations at the Leiden University Medical Center (Table 3.1). These eCAPs were recorded as part of the clinical intraoperative routine to assess CI function. All patients received a HiRes90K device (Advanced Bionics, Sylmar, CA), either with a 1J or a Mid-Scala electrode array. These electrode arrays consisted of 16 electrode contacts (numbered from 1 to 16 in apical to basal order). The eCAPs were recorded with the forward masking paradigm provided in the Research Studies Platform Objective Measures (RSPOM) software program (Advanced Bionics, Sylmar, CA). The eCAPs were measured on eight odd electrode contacts with stimulus levels ranging from 50 to 500 CU. The eCAP signal analysis was performed automatically by the RSPOM program (for details, see Biesheuvel et al. 2017). In brief, the eCAPs were evoked using monopolar charge-balanced, biphasic pulses (32 µs/phase) and recorded with a sampling rate of 56 kHz and a gain of 300. Raw eCAP recordings were 1.7 ms in duration and were filtered with a zero-phase shift, low-pass filter, using a cut-off frequency of 8 kHz. The N1 peak was identified as the minimum over the period from 180 to 490 µs, and P1 as the maximum from 470 to 980 µs after the end of stimulation. The eCAP amplitude was defined as the voltage difference between P1 and N1. After an automated analysis, the identified N1 and P1 peaks were visually inspected.

The noise level was defined as the average of the tail section of the eCAP, i.e., the last 30 samples of the recorded eCAP. It was assumed that no possible remaining neural response or stimulus artifact was present in this tail section (Biesheuvel et al. 2017). Similarly, at a baseline level of

eCAPs, there is no neural response or remaining artifact such that this should be mathematically equal to zero (e.g., Prijs, 1985; Charlet de Sauvage et al., 1987). Thus, we used the average level of the tail section as the baseline of the recorded eCAPs. The signal-to-noise ratio (SNR) was defined as the eCAP amplitude divided by the noise amplitude. Then, the eCAP was verified using a semiautomatic method programmed using MATLAB (Mathworks, Natick, MA, USA) with two criteria: the eCAP amplitude was larger than 20 μV; the SNR of the eCAP exceeded +13 dB. If eCAP recordings did not meet these criteria, they were excluded.

The eCAP waveforms were pre-processed before we analysed them with the deconvolution model. The baseline of each recorded eCAP was corrected to zero. Then, 50 additional samples were added to the start and end of the eCAP waveforms by performing a linear extrapolation to zero, to ensure that the entire eCAP waveform was included in the deconvolution analysis and to avoid introducing distortion with the deconvolution algorithm. This extrapolation only influenced the CDLD before and after the recording window (Strahl et al., 2016). We analysed a total of 4982 eCAPs.

TABLE 3.1. Patient demographics

Number of Patients	111
Gender (n)	
Male	45
Female	66
Cochlea implant type (n)	
HiRes90K 1J	16
HiRes90K Mid-Scala	95
Age group (n)	
Children (< 12)	38
Adults	73
Mean age ± SD (years)	39 ±30

3.2.2. Deconvolution model

To explore the temporal information in eCAPs, according to Eq.3.1, we modelled the eCAPs as

the convolution of a UR model with a CDLD model. Because the human UR was thought to be similar to the guinea pig UR (Briaire and Frijns 2005; Whiten 2007), we applied a guinea pig UR model in the present study (Versnel et al. 1992a), as shown in equation 3.2.

$$\mathrm{UR}(t) = \frac{U}{\sigma}(t - t_0)e^{[-\frac{(t-t_0)^2}{2\sigma^2}]} \tag{3.2}$$

The UR consisted of a negative (N) and positive (P) phase. The transition point between the negative phase and the positive phase was defined as t_0. Thus, U = U_N and $\sigma = \sigma_N$ for t < t_0; and U = U_P and $\sigma = \sigma_P$ for t > t_0, where σ_N and σ_P described the widths (s) of the negative and positive phases of the UR, respectively. The U_N and U_P described the magnitudes (V) of the two peaks.

Consistent with Strahl et al (2016), the CDLD model consisted of two Gaussian components, as shown in equation 3.3.

$$\mathrm{CDLD} = \alpha_1 * N(\mu_1, \sigma_1) + \alpha_2 * N(\mu_2, \sigma_2) \tag{3.3}$$

where N represents a Gaussian distribution; the variables α_1, μ_1 and σ_1 belong to the early Gaussian component (in time), and the variables, α_2, μ_2 and σ_2 belong to the late Gaussian component. The α_1 and α_2 are the peak amplitudes; the $\mu_1$and μ_2 are the peak latencies; and the σ_1 and σ_2 are the peak widths.

Subsequently, the UR and CDLD were used to predict the recorded eCAP waveforms with a deconvolution fitting error minimization routine (DMR). The DMR iteratively optimized the parameters of both UR and CDLD by minimizing the fitting error with a least-squares curve fit using MATLAB. The UR had to be solved before the temporal information could be derived. To this end, we performed two steps, as shown in Figure 3.3.

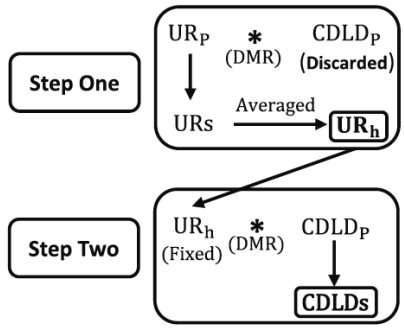

Fig. 3.3 Deconvolution model flow-chart. In step one, both the parameterised unitary response (UR) model (UR_p) and the parameterised compound discharge latency distribution (CDLD) model ($CDLD_p$) could be manipulated with the deconvolution fitting error minimization routine (DMR, asterisk). In this step, the URs of all eCAPs were derived, and the average of these URs was defined as the human UR (UR_h, black square). In step two, the UR_h was fixed, and only the $CDLD_p$ could be manipulated with the DMR. Then, the CDLDs of all eCAPs were calculated (CDLDs, black square).

3.2.2.1. The derivation of the human UR

In step one, a human UR was estimated. The parameters of the UR model (Eq. 3.2) and the CDLD model (Eq. 3.3) were simultaneously, iteratively adjusted with the DMR to approximate the recorded eCAPs (Fig. 3.3). To obtain realistic CDLDs and URs, the boundaries of the variables for the UR and CDLD models were iteratively varied to restrict the DMR. The boundary limits of the deconvolution model were based on the parameters of guinea pig UR: U_N [0.02, 0.25], σ_N [0.02, 0.13], U_P [0, 0.12], σ_P [0.08, 0.25], t_0 [-0.25, 0.06], α_1 [0, 0.35], μ_1 [0.04, 1.3], σ_1 [0, 0.3], α_2 [0, 0.35], μ_2 [0.04, 1.3], σ_2 [0, 0.3]. Assuming that the UR was constant for all contributing auditory nerve fibers and that the UR was identical between human subjects, we derived a human UR by averaging all the URs estimated from eCAPs, across subjects, electrode contacts, and stimulus levels.

3.2.2.2. The derivation of CDLDs

In step two, the temporal properties of eCAPs recorded in humans were analysed with our iterative deconvolution method. With a fixed human UR, as derived in step one (Fig. 3.3), we

could optimize the parameters of the CDLD model. Because of the fixed UR, the UR and CDLD models could not interact with each other, so that all the temporal information in eCAPs was forced into CDLDs. According to guinea pig UR, the boundaries of the variables of the CDLD model were set at the following values: α_1 [0, 0.35], μ_1 [0.15, 1.35], σ_1 [0, 0.45], α_2 [0, 0.35], μ_2 [0.15, 1.35], σ_2 [0, 0.45]. The 322 eCAP waveforms consist of an unusually large P1 and a small N1, and the ratio of the P1 to the N1 is larger than 1. These deviant eCAPs cannot be predicted by our deconvolution model, because the convolution of the human UR, consisting of a large negative phase and a small positive phase (green line, Fig. 3.1), with a strictly positive CDLD, cannot generate such eCAP waveforms. An example of the deviant eCAPs was shown in Fig. 3.4C (green line). Therefore, these 322 eCAPs were excluded.

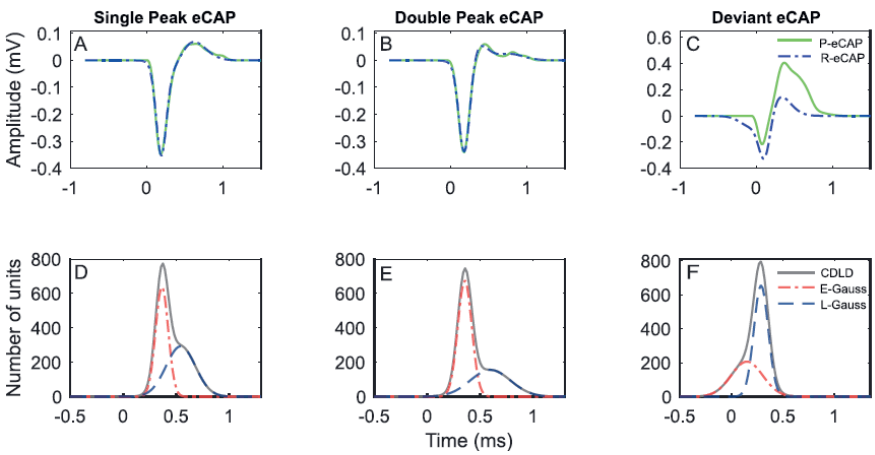

Fig. 3.4 Typical examples of electrically evoked compound action potentials (eCAPs) observed in this study. (Top row) The predicted eCAPs (blue dashed lines) and the recorded eCAPs (green solid lines); (bottom row) the corresponding compound discharge latency distributions (CDLDs). The columns show examples of a single-peak eCAP (A), a double-peak eCAP (B), and a deviant eCAP (C) and the corresponding CDLDs (D, E and F). R-eCAP: recorded eCAP; P- eCAP: predicted eCAP; E-Gauss: early Gaussian component; L-Gauss: late Gaussian component.

3.2.2.3. Analysis of the temporal information in eCAPs in CDLDs

As explained in section 1 (Introduction), we expected the temporal information in eCAPs to be

captured in CDLDs. First, the histograms of 6 CDLD parameters (in Eq. 3.4) derived from 4660 eCAPs were plotted individually in Figure 3.5. Second, because α indicated the CDLD magnitude, we assumed that α was positively associated with the eCAP amplitudes. Therefore, we evaluated the association between the α of the CDLD and the eCAP amplitude. Third, more excited nerve fibers led to both a larger eCAP amplitude and a larger AUCD. However, only the AUCD, which was calculated by integrating the CDLD over time, reflected the exact number of activated nerve fibers. Hence, we explored the AUCD as the best proxy for the exact number of activated nerve fibers over time. We also examined the correlation between the AUCD and the eCAP amplitude. The correlation analysis in this section was assessed using Pearson's coefficient using MATLAB.

3.2.2.4. Differences of the temporal information in eCAPs between children and adults

To explore the differences of the temporal information of the excited auditory nerve fibers between children and adults, we compared the differences of 6 CDLD parameters between child group (< 12 years) and adult group (>= 12 years) in Table 3.1 using the Wilcoxon Mann-Whitney U test. The significance level of each comparison was adjusted to 0.0083 using the Bonferroni correction (0.05 divided by 6 comparisons).

3.2.3 The validation of the two-Gaussian component CDLD model

We designed a multiple-Gaussian component CDLD model to determine whether the two-Gaussian component CDLD model was optimal. The formula for the CDLD model was:

$$\text{CDLD} = \sum_{n=1}^{m}(\alpha_n * N(\mu_n, \sigma_n)) \tag{3.4}$$

where *N* represents a Gaussian distribution, *m* represents the number of Gaussian components, α_n represents the amplitude, μ_n represents the peak latency, and σ_n represents the variance of the latencies in the Gaussian component *n*.

The fitting errors of simulations using different multiple-Gaussian component CDLD models were assessed by calculating the mean squares error (MSE) in MATLAB.

3.3.1 The unitary response of human auditory nerve fibers

To determine the human UR, we averaged all the URs obtained from the available 4982 eCAPs, by performing the DMR (step one in Fig. 3.3). Determined with Eq.3.2, the final parameters of the mean human UR with standard deviations were: $U_N = 0.155 \pm 0.003$ μV, $\sigma_N = 0.038 \pm 0.002$ ms, $U_P = 0.022 \pm 0.002$ μV, $\sigma_P = 0.155 \pm 0.009$ ms, $t_0 = -0.128 \pm 0.003$ ms (Fig. 3.2). Compared to the guinea pig UR (Versnel et al. 1992a, see Fig. 3.1), the σ_N of the negative phase of the human UR was 68% narrower, but 30% higher in magnitude, and the σ_P of the positive phase of the human UR was slightly broader, and 51% smaller in magnitude.

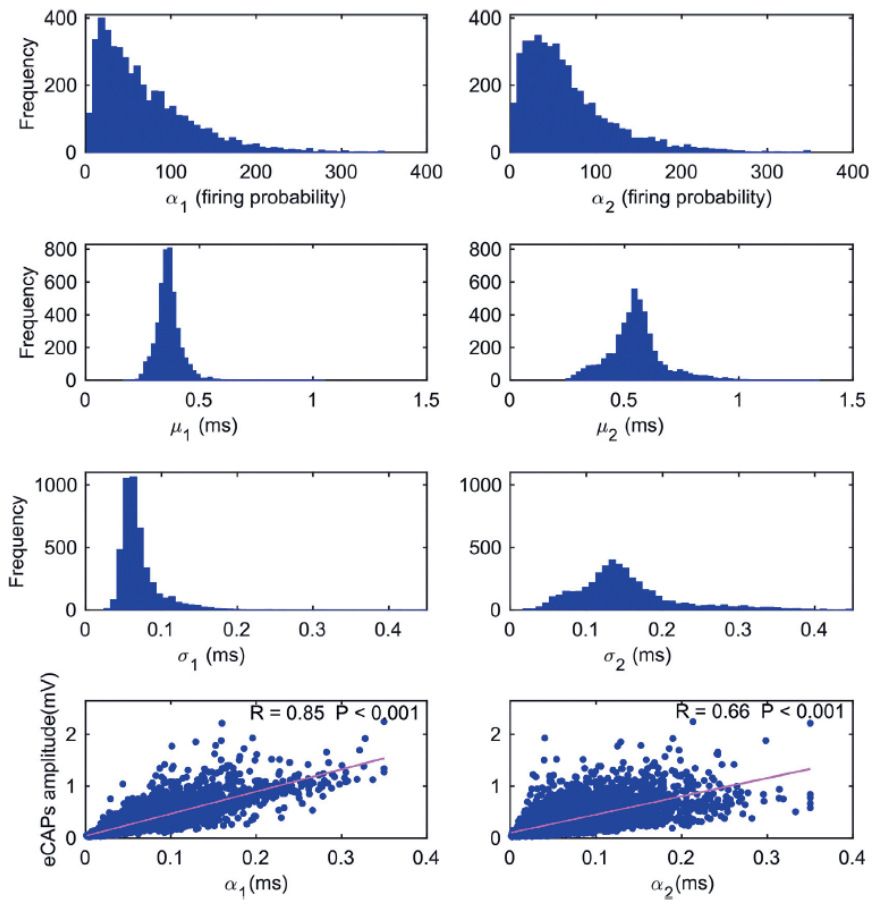

Fig. 3.5 The six parameters for compound discharge latency distributions (CDLDs) and their

associations with the corresponding electrically evoked compound action potential (eCAP) amplitudes. (Upper 3 rows) Distribution histograms of the six main CDLD parameters. (Bottom row) Scatterplots of eCAP amplitudes (y-axis) plotted against the corresponding α_1 *(left) and* α_2 *(right) values (x-axis).*

3.3. Results

3.3.2 Typical cases in the deconvolution model

With the DMR method and the human UR derived in step one, we could predict the recorded eCAPs (step two, Fig. 3.3). The morphological properties of the waveforms, 4660 eCAPs were classified according to visual inspection into two categories (Fig. 3.4), as described by Lai and Dillier (2000): single-peak eCAPs (75%) and double-peaked eCAPs (19%). Subsequently, we estimated the CDLDs from these eCAPs with the deconvolution model. We found 322 deviant eCAPs (6%), with a ratio of the P1 to N1 larger than 1. As explained above, they could not be predicted with our deconvolution model, and were excluded. The remaining 4660 eCAPs were used in subsequent analyses. Examples of these three eCAP categories (Fig. 3.4A, B and C) and the corresponding CDLDs (Fig. 3.4D, E and F, respectively) as predicted with the deconvolution model were shown.

3.3.3 Temporal properties of human eCAPs

3.3.3.1. The CDLD parameters

To investigate the synchronicity of the excited nerve fibers, we evaluated the distributions of all CDLD parameters for all eCAPs, recorded at different electrode contacts and different stimulus levels (Fig. 3.5). We found that all the distributions were skewed; that is, all the parameters of the early and late components (α_1 and α_2, μ_1 and μ_2, σ_1 and σ_2) were not normally distributed, based on a two-sample Kolmogorov-Smirnov test ($p < 0.001$). The median amplitudes of the two Gaussian components were slightly, but not significantly different ($p = 0.15$) using the Wilcoxon Mann-Whitney U test. The mean latency, μ_1 was significantly different from μ_2 ($p < 0.05$). Furthermore, μ_1 displayed a smaller degree of dispersion than μ_2

(standard deviations: 0.05 and 0.12 ms, respectively). The average width of the early Gaussian component of CDLDs was significantly different from the average width of the late Gaussian component using the Wilcoxon Mann-Whitney U test ($p < 0.01$), but the σ_1 displayed a smaller standard deviation than σ_2 (0.03 and 0.07 ms, respectively). Moreover, the two CDLD amplitude parameters (α_1, α_2) were correlated with the eCAP amplitudes using Spearman correlation coefficient (Fig. 3.5; linear regression, $r_1 = 0.85, p_1 < 0.001$; $r_2 = 0.66$, $p_2 < 0.001$). Table 3.2 shows the average (with standard deviation) and the median (with median deviation) of the 6 CDLD parameters.

3.3.3.2 Relationship between the eCAP amplitude and the AUCD

We investigated whether the AUCD increases proportionally with the eCAP amplitude. Figure 3.6 shows the AUCD plotted against the eCAP amplitude. As anticipated, the AUCD was significantly correlated with the eCAP amplitude ($r = 0.83$, $p<0.001$). Of note, different eCAPs with the same amplitudes could lead to very different CDLDs. For instance, two different eCAPs with the same amplitude (1 mV) had corresponding AUCDs that ranged from 200 to 500. This result indicated that the electrical stimulation did not necessarily activate the same number of nerve fibers each time, even when two eCAPs displayed the same amplitude.

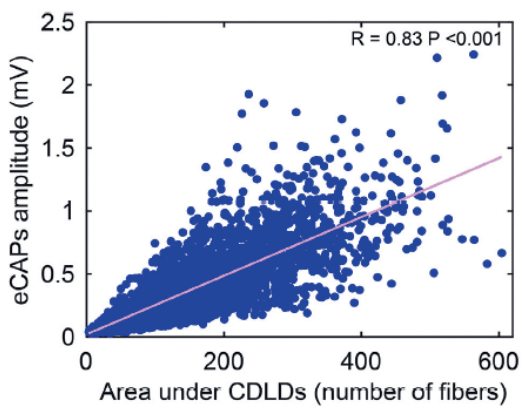

Fig. 3.6 Scatterplot showing the correlation between electrically evoked compound action potential (eCAP) amplitudes and the corresponding areas under the CDLD (AUCD) curves. CDLD: compound discharge latency distribution.

3.3.3.3 Temporal information in CDLDs between children and adults

We compared the differences of 6 CDLD parameters between the group of children and adults. The significance level of each comparison was corrected to 0.0083 using Bonferroni correction. Four CDLD parameters (α_1, μ_2, σ_1 and σ_2) showed significant differences between children and adults. We did not observe significant differences for the parameters α_2 and μ_1. The averages (with standard deviation) of CDLD parameters between the two groups are shown in Table 3.3.

TABLE 3.2. CDLD parameters for human eCAPs averaged over stimulation level

Parameters	α_1	α_2	μ_1 (sm)	μ_2 (sm)	σ_1 (sm)	σ_2 (sm)
Mean (SD)	0.069 (±0.054)	0.066 (±0.051)	0.36 (±0.055)	0.56 (±0.12)	0.073 (±0.031)	0.15 (±0.066)
Median (MD)	0.055 (±0.042)	0.054 (±0.038)	0.37 (±0.037)	0.55 (±0.085)	0.063 (±0.019)	0.14 (±0.047)

SD = Standard deviation; MD = Median deviation

TABLE 3.3. Comparison of child group and adult group: CDLD parameters averaged over stimulation level

Group	α_1	α_2	μ_1 (sm)	μ_2 (sm)	σ_1 (sm)	σ_2 (sm)
Adult group: mean(SD)	0.054 (±0.019)	0.059 (±0.024)	0.37 (±0.047)	0.58 (±0.09)	0.078 (±0.016)	0.17 (±0.053)
Child group: mean(SD)	0.075 (±0.029)	0.067 (±0.026)	0.36 (±0.024)	0.52 (±0.07)	0.068 (±0.01)	0.14 (±0.036)
p-value	0.0003*	0.13	0.27	0.008*	0.001*	0.002*

Adult group: patients >=12 years; Child group: (patients < 12 years). SD = Standard deviation. The significance level is 0.0083 using Bonferroni correction.
*Differences were significant.

3.3.3.4 Validation of the two-Gaussian component CDLD model

Next, we determined whether our two-Gaussian component CDLD model was the most optimal model. We tested models with 1 to 6 Gaussian components in the CDLD model (m in Eq. 3.4), and the fitting error after performing a DMR was evaluated for all the modelled eCAPs (mean squares error, MSE). It turned out that when the *m* was increased above 2, the fitting errors dropped just slightly (Fig. 3.7). Apparently, a multi-Gaussian component CDLD model gained no substantial benefit by increasing the number of components beyond 2, meaning that a two-Gaussian component CDLD (Eq. 3.3) was the best model.

3.4. DISCUSSION

In this study, a model was developed and tested that deconvolved human eCAPs into CDLDs, based on the UR assumption of auditory nerve fibers (Goldstein and Kiang,1958; Strahl et al.,

2016). As a part of this model, we estimated a human UR that proved to be different from the UR of guinea pigs (Versnel et al. 1992a). To the best of our knowledge, this study was the first to describe a human UR. We modelled the CDLDs underlying human eCAPs to describe the number of electrically excited auditory nerve fibers and their latency. Using the CDLD model, we were able to show differences in temporal characteristics of eCAPs between children and adults were found.

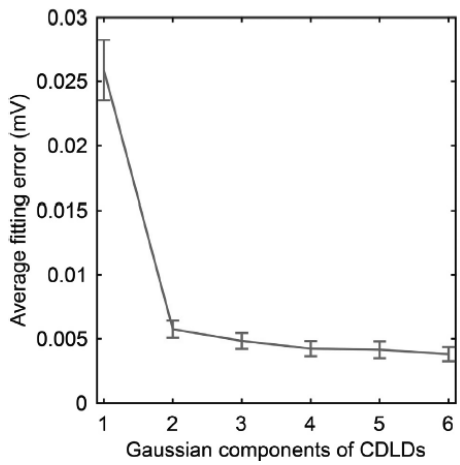

Fig. 3.7 Relationship between the Gaussian components of compound discharge latency distributions (CDLDs) and the average fitting error for all electrically evoked compound action potentials (y-axis) recorded in all patients. Error bars are MSEs (mean squares errors).

3.4.1 The UR of human auditory nerve fibers

To derive reliable CDLDs from human eCAPs through deconvolution, a representative human UR is critical (Kiang et al., 1976; Wang, 1979; Schoonhoven et al., 1989; Versnel et al., 1992a). However, the human UR waveform had not been previously published. To the best of our knowledge, no modelling studies or electrophysiological recordings have described the human UR in auditory nerve fibers. Previous studies assumed that the human UR was similar to that of guinea pigs (Briaire and Frijns 2005; Whiten 2007; Strahl et al., 2016). However, this may not hold true, given that the cochlea in guinea pigs is quite different in size and shape from the cochlea in humans (Nadol, 1988). In addition, the cell bodies of spiral ganglion cells are not

myelinated in humans, but they are in guinea pigs. These differences could lead to a different UR. Therefore, we aimed to derive a human UR based on human eCAPs. As a starting point, we used the UR function of guinea pigs published by Versnel et al. (1992a), in combination with wider boundary limits for fitting. We found that the human UR differed from the guinea pig UR. Hence, our modelled human UR was the first attempt to describe the UR of human auditory nerves. Compared to the guinea pig UR, the modelled human UR had a steeper negative component, but a slightly wider and shallower positive peak (Fig. 3.1). A possible explanation is that the absence of myelin in the human cell body can reduce the neural conduction velocities (Susuki 2010) and result in a delayed UR. Nadol (1988) has reported that the different cochlear morphology of cochlea in human and guinea pig, i.e., the size of the cochlea and the number of cochlear turns, may lead to different action potential waveforms. To further understand the differences of UR between human and guinea pig, more anatomical and electrophysiological studies are needed.

Of note, the assumption that URs are identical between fibers has not been fully validated. For instance, fibers have different fiber diameters, fiber-to-electrode distances, and response properties, which might trigger different URs, and these URs might contribute to eCAPs differently. However, some research has suggested that nerve fiber diameters were comparable at different locations in the cochlea (Liberman and Oliver,1984) and that the URs contributed by different fibers along the cochlea were not significantly different (Miller et al., 1999). In the present study, we found significant correlations between the eCAP amplitudes and the CDLD parameters α_1 and α_2, and between the eCAP amplitudes and the AUCD. These findings indicate that the eCAP amplitude increases when more auditory nerve fibers are excited by electrical stimulation and that these nerve fibers fire with a higher level of synchronicity. These outcomes are consistent with the assumption that the (e)CAP amplitude is linearly correlated with the number of activated nerve fibers (Goldstein and Kiang, 1958; Versnel et al., 1992a). In this study, the recorded eCAPs from children and adults were effectively predicted using the same UR. This finding supports the assumption that the UR is identical between fibers and across

subjects (e.g., Goldstein and Kiang, 1958; Prijs, 1985; Versnel et al., 1992a). Based on these observations, we cautiously assumed that the UR of human auditory nerve fibers was constant. To address this assumption further, more modelling studies or electrophysiological recordings studies on human auditory nerve fibers are required.

3.4.2 The temporal information of eCAPs contained in CDLDs

In this study, we validated that the two-Gaussian component CDLD was the best model. We constructed a multi-Gaussian component CDLD model (with 1 to 6 components) to predict the recorded eCAPs by performing DMR. When the number of Gaussian components (n, in Eq. 3.4) rose from 1 to 2, the fitting outcome showed a reduced fitting error (78%). When the n increased from 2 to 3, the fitting outcome showed that little additional benefit was gained (4%; Fig. 3.7). These results indicated that the two-Gaussian component CDLD was the best model. This finding is consistent with the findings of Strahl et al (2016), who also described a two-Gaussian component CDLD. The human UR and the CDLD could interact with each other in step one as the parameters of the UR and the CDLD were both manipulated. Consequently, the temporal information in eCAPs could be demonstrated both in URs and CDLDs and locally but not globally optimal parameters of the CDLD model were derived. Therefore, the CDLDs derived in step one cannot reliably reflect the temporal information in eCAPs. To address this issue, we performed our iterative deconvolution again using a fixed UR so that only the parameter of CDLD can be optimized in step two (Fig. 3.3). During this iterative procedure, all the temporal information was encoded into CDLDs and these CDLDs accurately reflected the temporal information in eCAPs.

Most of the eCAP waveforms, both the single peak eCAPs and the double peak eCAPs, in our study were fit better with a double Gaussian component CDLD model (Fig. 3.4) than with a single Gaussian component model. Our finding suggested that eCAP waveforms that appear to have a single peak could arise from a two-Gaussian component CDLD. If true, it follows that CDLDs might consist of two independent components that originate from two separate groups

of neural responses. This hypothesis was in line with the concept of double group neural responses proposed by Stypulkowski and van den Honert (1984) and with the simulations including a combination of neural responses arising from axons and peripheral processes (Lai and Diller, 2000). In their findings, the early Gaussian component of CDLDs could be attributed to direct excitation of the axonal process in the modiolus proximal to the spiral ganglion cell, and the late CDLD component could be attributed to the activation of the axon peripheral to the cell body of the bipolar ganglion cell. This hypothesis was supported by our finding that the time interval between μ_1 and μ_2 (0.2 ms, see in Fig. 3.5) was shorter than the absolute refractory period of these nerve fibers (approximately 0.45 ms), as reported by He et al. (2017). Therefore, we could rule out the possibility that the neural responses in the two-component of CDLD might have originated from the same group of auditory nerve fibers. A recent study, by Finley et al. (presented at CIAP 2019), indicated that multiple neural response sites with different waveform morphologies, latencies, magnitudes, and scalar distributions could contribute to differences in the eCAPs measured in the cochlea.

A limitation of our deconvolution model was that it relied on the eCAP waveforms. In some cases, the eCAPs had deviant waveforms that could not be simulated by our deconvolution model. However, those instances were rare (approximately 6%).

We determined the distributions of the CDLD parameters shown in Eq. 3.3. The distribution of the σ_1 showed smaller means and variations compared to the distributions of the σ_2. The average of α_2/α_1 (0.96) in our study was quite similar to that reported by Strahl in humans (apex: 0.96, middle: 0.86, base: 0.85). However, our μ_1 (0.36 ms), μ_2 (0.55 ms), σ_1 (0.071 ms), and σ_2 (0.15 ms) values were smaller than those reported by Strahl (on average: μ_1 = 0.52 ms, μ_2 = 0.9 ms, σ_1 = 0.14, and σ_2 = 0.27). When we used the guinea pig UR to derive the CDLD from our eCAPs, the μ_1 and μ_2 changed slightly in the direction of the value reported by Strahl et al. (2016): shifting from 0.36 ms and 0.55 ms to 0.41 ms and 0.69 ms, respectively, with a larger variance. This indicated that using a guinea pig UR leads to a poorer fitting of human CDLDs. Thus, these differences might be attributable to the UR used in Strahl's study,

which was derived from guinea pig eCAPs, rather than human eCAPs. The distance between the electrode contact and the nerve fibers may affect CDLDs. Previous studies reported that the perimodiolar electrode arrays can yield a lower threshold in comparison to electrodes located close to the outer wall (e.g., Frijns et al., 1995; Briaire et al., 2000). When an electrode is located closer to the modiolus, less current is required to excite the auditory nerve fibers (e.g., Kang et al., 2015). Therefore, a shorter distance to modiolus can lead to activation of more nerve fibers and a larger α_1, α_2 and AUCD can be obtained. Conversely, a larger distance could result in a smaller α_1, α_2 and AUCD.

We found that analysing CDLDs had at least two advantages over analysing eCAP amplitudes directly. First, when studying latency effects, the CDLD could more precisely reflect the latency of eCAPs over time than the N1 and P1 of eCAPs. Second, the AUCD (i.e., the integral of CDLD over time) could provide more accurate information about the number of excited nerve fibers. Because only healthy fibers can be activated, the AUCD might also reflect the survival of nerve fibers (Khan et al., 2005; Fayad and Linthicum, 2006). On the other hand, we found that eCAPs with equal amplitudes could lead to different AUCDs in the deconvolution model (Fig. 3.6), indicating that different eCAPs with same amplitude could arise from very different numbers of excited nerve fibers. Contrary to the unitary response concept, this would indicate that the eCAP amplitude could not accurately indicate the number of excited auditory nerve fibers.

In this study, significant differences of the temporal information between children and adults were revealed by calculating CDLDs using iterative deconvolution (Table 3.3). These differences may be attributable to the observation that auditory nerve fibers of hearing-impaired adults undergo significant degeneration over the years (e.g., Abbas et al., 1991). For instance, in comparison to the group of children, we observed larger peak widths (σ_1 and σ_2) in adults, presumably reflecting that the excited nerve fibers showed a lower level of synchronicity in this group. Compared with adults, a larger α_1 in the group of children may indicate that more nerve fibers can be excited in their central axon. A larger μ_2 observed in the adult group likely implies more severe degeneration of the peripheral process compared with the children.

The outcomes of the present study suggested some potential applications for future clinical practice. First, although many studies have investigated the relationship between speech performance and nerve fiber survival (Kawano et al., 1998; Khan et al., 2005; Fayad and Linthicum, 2006; Xu et al., 2012), the findings were inconsistent. A likely explanation might be that most investigators focused mainly on the eCAP magnitudes, which could not precisely indicate the number of activated nerve fibers and their latency. With our deconvolution model, it is possible to investigate the relationship between the temporal information in eCAPs and speech perception in patients with CIs. For instance, our deconvolution model provided the growth function of the AUCD and the threshold of the AUCD, which might associate well with speech perception in patients with CIs. Additionally, consistent with the finding by Strahl et al. (2016) that some of the CDLD parameters could indicate the degeneration of nerve fibers, we found that the AUCDs derived with our method might be more accurate than the eCAP amplitude for indicating nerve fiber survival in patients because only the AUCD indicates the number of excited nerve fibers. Furthermore, our deconvolution model has low computational complexity. With the estimated UR, the computation of each CDLD could be completed in 0.1 s from the recorded eCAP using our deconvolution model in MATLAB. Thus, our deconvolution could be potentially integrated into clinical software to derive the temporal information of eCAPs in near-real-time of CI recipients.

3.5 Conclusions

This study described an iterative deconvolution model, based on the UR hypothesis, to derive the CDLD from recorded human eCAPs. We estimated a human version of the UR, which was not available previously. Importantly, we found that the human UR differed from the guinea pig UR. With the estimated human UR, we derived the CDLDs of 4660 eCAPs. We demonstrated that CDLDs had advantages over the more commonly used eCAP amplitude because they better reflected the temporal properties of eCAPs. Therefore, CDLDs provided better estimates of the number of excited auditory nerve fibers and their firing latencies.

Acknowledgements

The first author of this study is financially supported by the China Scholarship Council.

References

Abbas, P. J., & Brown, C. J. (1991). Electrically evoked auditory brainstem response: Refractory properties and strength-duration functions. Hearing Research, 51(1), 139–147.

Abbas, P., Brown, C., Shallop, J., Firszt, J., Hughes, M., Hong, S., & Staller, S. (1999). Summary of results using the nucleus CI24M implant to record the electrically evoked compound action potential. Ear Hear.

Biesheuvel, J. D., Briaire, J. J., & Frijns, J. H. M. (2018). The Precision of eCAP Thresholds Derived From Amplitude Growth Functions. Ear and Hearing, 39(4), 701–711.

Bonci, A., Lupica, C. R., & Morales, M. (2015). Assessment of spectral and temporal resolution in cochlear implant users using psychoacoustic discrimination and speech cue categorization. HHS Public Access (Vol. 18).

Botros, A., & Psarros, C. (2010). Neural Response Telemetry Reconsidered : II . The Influence of Neural Population on the ECAP Recovery Function and Refractoriness. Ear & Hearing, 31(3), 380–391.

Briaire, J. J., & Frijns, J. H. (2000). Field patterns in a 3D tapered spiral model of the electrically stimulated cochlea. Hearing research, 148(1-2), 18-30.

Briaire, J. J., & Frijns, J. H. M. (2005). Unraveling the electrically evoked compound action potential. Hearing Research, 205(1–2), 143–156.

Charles C. Finley, Laura K. Holden, Timothy A. Holden, Jill B. Firszt. "Spatial Deconvolution of Intracochlear Potentials Supports Ectopic Electrical Stimulation Phpothesis". 2019 CIAP.

Charlet de Sauvage R., Aran, J. M., & Erre, J. P. (1987). Mathematical analysis of VIIIth nerve cap with a linearly-fitted experimental unit response. Hearing Research, 29(2–3), 105–115.

Dolan, D. F., Teas, D. C., & Walton, J. P. (1983). Relation between discharges in auditory nerve fibers and the whole-nerve response shown by forward masking: an empirical model for the AP. J Acoust Soc Am, 73(2), 580–591.

Fayad, J. N., & Linthicum, F. H. (2006). Multichannel cochlear implants: Relation of histopathology to performance. Laryngoscope, 116(8), 1310–1320.

Frijns, J. H. M., De Snoo, S. L., & Schoonhoven, R. (1995). Potential distributions and neural excitation patterns in a rotationally symmetric model of the electrically stimulated cochlea. Hearing research, 87(1-2), 170-186.

Goldstein, M. H., & Kiang, N. Y. S. (1958). Synchrony of Neural Activity in Electric Responses Evoked by Transient Acoustic Stimuli. Jasa, 30(2), 107–114.

He, S., Teagle, H. F. B., & Buchman, C. A. (2017). The Electrically Evoked Compound Action Potential: From Laboratory to Clinic. Frontiers in Neuroscience, 11(June), 1–20.

Heil, P., & Peterson, A. J. (2015). Basic response properties of auditory nerve fibers: a review. Cell and Tissue Research, 361(1), 129–158.

Hoke, M., Elberling, C., Hieke, D. and Bappert, E. (1979) Deconvolution of compound action potentials and nonlinear features of the PST histogram. Scand. Audiol. Suppl. 9, 141-154.

Kang, S., Chwodhury, T., Moon, I. J., Hong, S. H., Yang, H., Won, J. H., & Woo, J. (2015). Effects of electrode position on spatiotemporal auditory nerve fiber responses: A 3D computational model study. Computational and Mathematical Methods in Medicine, 2015.

Kawano, A., Seldon, H. L., Clark, G. M., Ramsden, R. T., & Raine, C. H. (1998). Intracochlear factors contributing to psychophysical percepts following cochlear implantation. Acta Oto-Laryngologica, 118(3), 313–326.

Khan, A. M., Whiten, D. M., Nadol, J. B., & Eddington, D. K. (2005). Histopathology of human cochlear implants: Correlation of psychophysical and anatomical measures. Hearing Research, 205(1–2), 83–93.

Kiang, N.Y.S., Moxon, E.C. and Kahn, A.R. (1976) The relationship of gross potentials recorded from the cochlea to single unit activity in the auditory nerve. In: R.J. Ruben, C. EIberling and G. Salomon (Eds.), Electrocochleography, University Park Press, Baltimore, pp. 95-115.

Kim, J., Abbas, P. J., Brown, C. J., Christine, P., Brien, S. O., & Kim, L. (2011). The Relationship between Electrically Evoked Compound Action Potential and Speech Perception : A Study in Cochlear Implant Users with Short Electrode Array, 31(7), 1041–1048.

Lai, W. K., & Dillier, N. (2000). A Simple Two-Component Model of the Electrically Evoked Compound Action Potential in the Human Cochlea. Audiology and Neurotology, 5(6), 333–345.

Liberman, M. C., & Oliver, M. E. (1984). Morphometry of Intracellularly Labeled Neurons of the Auditory Nerve: Correlations With Functional Properties, 176.

Miller, C. A., Abbas, P. J., Rubinstein, J. T., Robinson, B. K., Matsuoka, A. J., & Woodworth, G. (1998). Electrically evoked compound action potentials of guinea pig and cat: Responses to monopolar, monophasic stimulation. Hearing Research, 119(1–2), 142–154.

Miller, C. A., Brown, C. J., Abbas, P. J., & Chi, S. L. (2008). The clinical application of potentials evoked from the peripheral auditory system. Hearing Research, 242(1–2), 184–197.

Miller, C. A., Abbas, P. J., & Rubinstein, J. T. (1999). An empirically based model of the electrically evoked compound action potential. Hearing Research, 135(1–2), 1–18.

Nadol, J. B. (1988). Comparative anatomy of the cochlea and auditory nerve in mammals. Hearing Research, 34(3), 253–266.

Ramekers, D., Versnel, H., Strahl, S. B., Smeets, E. M., Klis, S. F. L., & Grolman, W. (2014). Auditory-nerve responses to varied inter-phase gap and phase duration of the electric pulse stimulus as predictors for neuronal degeneration. JARO - Journal of the Association for Research in Otolaryngology, 15(2), 187–202.

Schoonhoven, R., Versnel, H., Prijs, V.F. and Keijzer, J. (1989) The unit response and the relation between single fibre discharge patterns and the compound action potential. In: G. Cianfron, F. Grandori and D.T. Kemp (Eds.), 2rid Interuational Symposium on Cochlear Mechanics and Otoacoustic Emissions, 1989, Rome. ll Valsalva 54, Suppl.l, pp. 48-53.

Seyyedi, M., Viana, L. M., Eye, M., & Infirmary, E. (2015). Within-Subject Comparison of Word Recognition and Spiral Ganglion Cell Count in Bilateral Cochlear Implant Recipients, 35(8), 1446–1450.

Strahl, S.B., Ramekers, D., Nagelkerke, M.M.B., Schwarz, K.E., Spitzer, P., Klis, S.F.L., Grolman, W., Versnel, H. (2016). Assessing the firing properties of the electrically stimulated auditory nerve using a convolution model. Adv. Exp. Med. Biol. 894: 143-153.

Stypulkowski, P. H., & van den Honert, C. (1984). Physiological properties of the electrically stimulated auditory nerve. I. Compound action potential recordings. Hearing Research, 14(3), 205–223.

Susuki, K. (2010). Myelin: a specialized membrane for cell communication. Nat. Educ. 3:59.

van de Heyning, P., Arauz, S. L., Atlas, M., Baumgartner, W. D., Caversaccio, M., Chester-Browne, R., … Skarzynski, H. (2016). Electrically evoked compound action potentials are different depending on the site of cochlear stimulation. Cochlear Implants International, 17(6), 251–262.

van Gendt, M. J., Briaire, J. J., & Frijns, J. H. M. (2019). Effect of neural adaptation and degeneration on pulse-train ECAPs: A model study. Hearing Research, 377, 167–178.

Versnel, H., Prijs, V. F., & Schoonhoven, R. (1992a). Round-window recorded potential of single-fibre discharge (unit response) in normal and noise-damaged cochleas. Hearing Research, 59(2), 157–170.

Versnel, H., Schoonhoven, R., & Prijs, V. F. (1992b). Single-fibre and whole-nerve responses to clicks as a function of sound intensity in the guinea pig. Hearing Research, 59(2), 138–156.

Wang, Binseng. (2005). The Relation Between the Compound Action Potential and Unit Discharges in the Auditory Nerve. Thesis (Sc.D.)--Massachusetts Institute of Technology, Dept. of Electrical Engineering and Computer Science, 1979.

Westen, A. A., Dekker, D. M. T., Briaire, J. J., & Frijns, J. H. M. (2011). Stimulus level effects on neural excitation and eCAP amplitude. Hearing Research, 280(1–2), 166–176.

Whiten, D. M. (Darren M. 1977-. (2007). Electro-anatomical models of the cochlear implant.

Xu, H. X., Kim, G. H., Snissarenko, E. P., Cureoglu, S., & Paparella, M. M. (2012). Multi-channel cochlear implant histopathology: Are fewer spiral ganglion cells really related to better clinical performance? Acta Oto-Laryngologica, 132(5), 482–490.

Zhu, X., Cao, K., Pan, T., Yang, H., Wang, Y. Electrically evoked auditory nerve compound action potentials in Nucleus CI24M cochlear implant users. Lin Chuang Er Bi Yan Hou Ke Za Zhi. 2002 Jan;16(1):5–8.

Chapter 4

Predicting speech performance in individuals with cochlear implants, based on temporal firing properties of auditory nerve fibers derived from eCAPs

Yu Dong, Jeroen J. Briaire, H. Christiaan

Stronks and Johan H. M. Frijns

Ear and Hearing (under review)

Abstract

Objectives: Many studies have assessed the performance of individuals with cochlear implants (CIs) with electrically evoked compound action potentials (eCAPs). These eCAP-based studies have focused on the amplitude information of the response, without considering the temporal firing properties of excited auditory nerve fibers (ANFs). These temporal features have been associated with neural health in animal studies and, consequently, could be of importance to clinical CI outcomes. With a deconvolution method, combined with a unitary response, the eCAP can be mathematically unraveled into the compound discharge latency distribution (CDLD). The CDLD reflects both the number and the temporal firing properties of excited ANFs. The present study aimed to determine to what extent the temporal properties of eCAPs (quantitatively analyzed in the CDLD) are related to speech perception in individuals with CIs.

Design: This retrospective study acquired data on monosyllabic word recognition scores and intra-operative eCAP amplitude growth functions (AGFs) from 124 adult patients with post-lingual deafness that received the Advanced Bionics HiRes 90K device. The CDLD was determined for each recorded eCAP waveform by deconvolution. Each of the two Gaussian components of the CDLD was described by three parameters: the amplitude, the firing latency (the average latency of each component of the CDLD), and the variance of the CDLD components (an indication of the synchronicity of excited ANFs). The area under the CDLD curve (AUCD) was indicative of the total number of excited ANFs over time. The slope of the AUCD growth function indicated the increases in the number of excited ANFs in response to increasing stimulus levels. Associations between speech perception and each of these CDLD parameters were investigated with linear mixed modeling.

Results: In individuals with CIs, speech perception was significantly associated with the amplitudes of the two CDLD components: the AUCD and the slope of the AUCD growth function, but not with the CDLD latencies. In addition, speech perception was significantly associated with the latency variance in the early CDLD component, but not with the latency

variance in the late CDLD component. Compared to the eCAP amplitude and the slope of the AGF, the amplitude and variance of the first CDLD component, the AUCD and the slope of the AUCD growth function provided a similar explanation of the variance in speech perception but with a higher significance level.

Conclusions: The results demonstrated that both the number and the neural synchrony of excited ANFs, revealed by CDLDs, were indicative of post-implantation speech perception in individuals that received CIs. The CDLD-based parameters could provide a higher significance than the eCAP amplitude or the AGF slope. The authors concluded that CDLDs might serve as a clinical predictor of the survival of ANFs and postoperative speech perception performance. Thus, it would be worthwhile to incorporate the CDLD into eCAP measures in future clinical applications.

Keywords: Cochlear implants; Sensorineural hearing loss; Electrically evoked compound action potential; Temporal firing properties; Speech perception; Neural synchronicity

4.1 Introduction

A cochlear implant (CI) is an implantable device that can partially restore the hearing ability of patients with severe sensorineural hearing loss. Although speech perception capabilities of patients with CIs have improved dramatically over the years, speech outcomes of patients with CIs have been quite unpredictable and variable (van Dijk et al. 1999; Turner et al. 2002; van Eijl et al. 2017). An important factor that affects the speech outcomes of patients with CIs is the condition of the auditory nerve. The neural responses generated by auditory nerve fibers (ANFs) can be evaluated by measuring electrically evoked compound action potentials (eCAPs) in patients with CIs (Fayad & Linthicum 2006; Kim et al. 2010; Garadat et al. 2012; Ramekers et al. 2015; He et al. 2017). The eCAP is typically assessed by examining its amplitude; namely, the difference between the first negative peak (N1) and the first positive peak (P1) (e.g., Lai & Dillier 2000; Kim et al. 2010). This amplitude is thought to be approximately proportional to the

number of ANFs that responded to the stimulus pulse (e.g., McKay et al. 2013; Seyyedi et al. 2014).

Early studies have investigated whether eCAPs could be used to predict speech perception of patients with CIs after implantation. For instance, DeVries et al. (2016) reported that subjects with large eCAP amplitudes tended to show better speech perception scores. Some studies have looked at the slope of the eCAP amplitude growth function (AGF). Steeper AGF slopes, i.e., a faster rate of increase in eCAP amplitude with rising stimulus levels, were associated with a higher density of surviving ANFs (e.g., Kim et al. 2010; He et al. 2017). Moreover, some studies (Brown et al. 1990; Kim et al. 2010) found that steeper AGF slopes were associated with better speech performance, but in other studies, this result was not reproduced (Franck & Norton 2001; Turner et al. 2002; Cosetti et al. 2010). In most studies, the temporal firing properties of excited ANFs that underlie eCAPs were not taken into consideration. However, the eCAP waveforms reflect the temporal firing properties of the excited ANF population (e.g., Goldstein & Kiang 1958; Versnel et al. 1992; Miller et al. 1997). It has been suggested that these temporal firing properties may hold predictive value for anticipating future ANF survival and function (e.g., Miller et al. 1997; Strahl et al. 2016) and potential speech outcomes in individuals with CIs (Pichora-Fuller et al. 2007; Dong et al. 2020).

To extract the temporal firing properties from human eCAPs, an iterative deconvolution method was proposed (Dong et al. 2020, 2021), which assumed that all ANFs had the same unitary response (Fig. 4.1) (Goldstein & Kiang 1958; Versnel et al. 1992). In this method, each eCAP was reconstructed by convolving the unitary response with a parameterized compound discharge latency distribution (CDLD). The CDLD represents the sum of the unitary responses of all individual excited ANFs over time. The simulated eCAP was optimized to match the recorded eCAP by iteratively adjusting the variables in the parameterized CDLD. A two-Gaussian component CDLD was described, as shown in Eq. 4.1 (Fig. 4.1).

$$\mathrm{CDLD_p} = \alpha_1 * \mathrm{N}(\mu_1, \sigma_1) + \alpha_2 * \mathrm{N}(\mu_2, \sigma_2) \tag{4.1}$$

where N represents the Gaussian distribution; the variables α_1, μ_1 and σ_1 belong to the early Gaussian component (in time), and the variables α_2, μ_2 and σ_2 belong to the late Gaussian component. The α_1 and α_2 are the peak amplitudes; the μ_1 and μ_2 are the peak latencies, representing the average firing latencies of excited ANFs; and the σ_1 and σ_2 are the peak widths, which indicate the degree of synchronicity in excited ANFs. The early and late components of CDLDs may be attributed to the excitation of the proximal and peripheral axonal processes of ANFs, respectively (e.g., Stypulkowski & van den Honert 1984; Lai & Dillier 2000; Dong et al. 2020), or due to separate neural responses of part of the ANF population (Ramekers et al. 2015; Konerding et al. 2020). The CDLD can be used to reveal eCAP characteristics, in terms of the number and temporal firing properties of excited ANFs (Fig. 4.1). Specifically, the α_1 and α_2 indicate the neural firing density. These parameters are highly related to the number of excited ANFs and the eCAP amplitude (Strahl et al. 2016; Dong et al. 2020). The number of excited ANFs could be estimated with the area under the CDLD (AUCD) more accurately than with the eCAP amplitude (Dong et al. 2020). Similar to the AGF, the AUCD growth function (AUGF) can be calculated by plotting the AUCD as a function of the stimulus level. The slope of the AUGF indicates the rate of increase in the number of excited ANFs with rising stimulus levels. Previous studies have not considered these temporal firing properties in explorations of whether speech perception was associated with eCAPs after a CI implantation.

In the present study, we aimed to find out to what extent speech perception performance in individuals with CIs can be explained by the temporal firing properties of excited ANFs that are represented in eCAPs. To that end, the CDLD was determined from intraoperatively recorded eCAP waveforms, based on an iterative deconvolution method (Dong et al. 2021). We investigated whether the eight parameters of Eq. 4.1 were correlated with speech perception in individuals after CI implantation. To facilitate comparisons with existing literature, we also compared the predictive value of these eight parameters with the predictive values determined with conventional methods, based on the eCAP amplitude and the AGF slope. The results might provide a new clinical predictor of ANF survival and postoperative speech perception

performance.

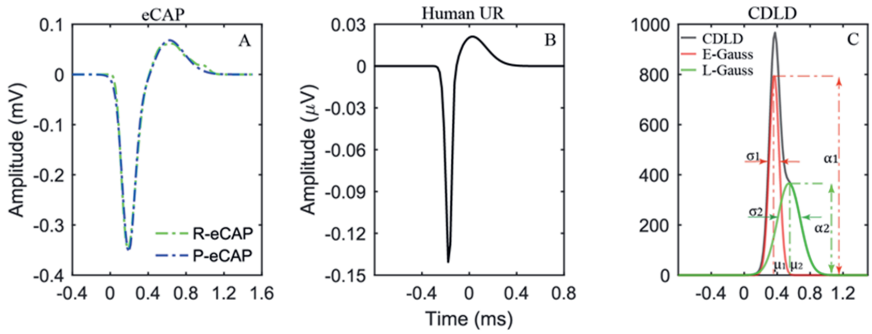

Fig. 4.1 Extraction of the temporal firing properties of excited auditory nerve fibers from eCAPs, based on an iterative deconvolution method proposed by Dong et al. (2020, 2021). In this method, an eCAP (A, blue line) was calculated by convoluting a human unitary response (UR) (B) and a parameterized CDLD (C), optimized to match a recorded eCAP (A, green line), and iteratively minimizing the fitting error. This CDLD (C) consists of early and late Gaussian components; the parameters of the early component (α1, μ1, and σ1) and the late component (α2, μ2, and σ2) reflect the temporal firing properties. eCAP: electrically evoked compound action potential; R-eCAP: recorded eCAP; P-eCAP: predicted eCAP; CDLD: compound discharge latency distribution; E-Gauss: early Gaussian component; L-Gauss: late Gaussian component.

4.2 MATERIAL AND METHODS

4.2.1 Patient Population

This retrospective study included AGF recordings from 134 adult patients with post-lingual deafness that had undergone CI implantation at the Leiden University Medical Center between June 2012 and March 2019. The AGF was recorded as part of the standard clinical routine for assessing CI function intraoperatively. All patients received unilateral implants with a HiRes90K device, with either a HiFocus-1J or a HiFocus Mid-Scala electrode array (Advanced Bionics, Valencia, CA). These electrode arrays consisted of 16 electrode contacts (numbered from 1 to 16, in apical to basal order). According to the inclusion criteria of eCAPs, 10 patients were

excluded (see Data Recordings). Therefore, the remaining 124 patients were included in the analysis. Table 4.1 shows the characteristics of the included patients.

TABLE 4.1. Characteristics of patients with cochlear implants due to post-lingual deafness

Characteristic	Patients (n = 124)
Sex	
Male	49
Female	75
Cochlear implant type	
HiRes90K 1J	19
HiRes90K Mid-Scala	105
Mean age at implantation, years	61.3 ± 19.2
Mean duration of deafness, years	14.1±13.7
Etiology	
Ototoxic Medication	3
Meniere's disease	2
Meningitis	8
Otosclerosis	7
Usher syndrome	2
Congenital/Hereditary (non-specified)	37
Other/Unknown	65
Monosyllabic word scores at 1 year, % correct	60.8 ± 21.1

Values are the number of patients or mean ± SD, as indicated.

4.2.2 Data Recordings

4.2.2.1 Test Procedure for AGFs

The AGFs were recorded on all odd electrode contacts with the forward-masking paradigm

provided in the Research Studies Platform Objective Measures software program (Advanced Bionics, Sylmar, CA). The electrical stimulus for the masker and probe was a monopolar, cathodic-first, charge-balanced, biphasic pulse (32 µs/phase). The interval between the masker and probe pulses was fixed at 400 µs. The eCAP response was recorded at a sampling rate of 56 kHz and a gain of 300. For each eCAP, 32 averages were performed. Each AGF was based on ten different current levels, ranging from 50 to 500 clinical units (CU). Additional details on the recordings were described previously (Biesheuvel et al. 2017; Dong et al. 2020).

The N1 and P1 peaks of eCAP waveforms were defined as the minimum and maximum amplitudes, respectively, measured across the 180 to 490 µs and the 470 to 980 µs intervals after the end of stimulation. The eCAP amplitude was defined as the voltage difference between P1 and N1 (mV). The noise level of the recording was determined from the last 30 samples of the recording, with the assumption that no remaining neural response or stimulus artifact was present in this section (for details, see Dong et al. 2021). The signal-to-noise ratio of the eCAP was calculated as the eCAP amplitude divided by the root mean square of the noise segment. Valid eCAPs were selected using a semiautomatic method programmed in MATLAB (Mathworks 2019a, Natick, MA, USA), which included two criteria: the eCAP amplitude had to be larger than 25 µV, and the signal-to-noise ratio had to exceed +15 dB. eCAPs that did not meet both of these criteria were excluded. As a result, we included 5612 eCAPs obtained from 920 AGFs originating from 124 patients (3588 recordings were excluded) for further analysis.

We performed linear regression on the AGF data to extract the slope of the best-fit regression line (µV/CU). The intercept of the line with the x-axis is defined as the eCAP threshold (for details see Biesheuvel et al. 2017). An example of an AGF and its underlying recordings is shown in Fig. 4.2.

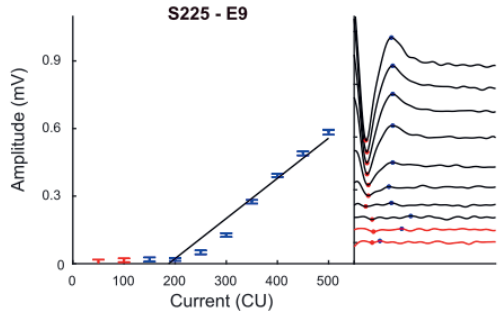

Fig. 4.2 Example of an AGF from the subject S225, obtained at electrode 9. The AGF (left) shows the eCAP amplitude as a function of stimulus intensity. The corresponding eCAPs (right) are plotted from low (bottom) to high (top) stimulus intensity. Data points that did not show true eCAP responses are shown in red, and points included in the AGF are shown in blue. Error bars reflect the variance in eCAP amplitude. AGF: amplitude growth function; eCAP: electrically evoked compound action potential.

4.2.2.2 Extraction of the Temporal Firing Properties in eCAPs

To deduce the temporal firing properties of excited ANFs from eCAPs, we calculated CDLDs from eCAP waveforms with an iterative deconvolution method (for details see Dong et al. 2020, 2021). Before we calculated CDLDs, the eCAP waveforms of AGFs were pre-processed. First, the baseline was corrected to zero, with the noise level as a reference. Second, to circumvent mathematical problems, due to the convolutions, 50 additional samples were added to the start and end of the recorded waveforms by performing a linear extrapolation to zero. Then, the pre-processed eCAPs were entered as input into the iterative deconvolution procedure to obtain CDLDs. Specifically, we simulated the eCAPs as the convolution of the human unitary response calculated by Dong et al. (2020) with a parameterized CDLD (Eq. 4.1), with a deconvolution fitting error minimization routine (Fig. 4.1). In this routine, the human unitary response was constant and the simulated eCAP was optimized by iteratively adjusting the variables in the parameterized CDLD, until the simulated eCAP converged to the recorded eCAP. We validated the goodness of fit by calculating the normalized root mean square error. Then, the temporal firing properties were revealed, based on the CDLD parameter values, as shown in Equation 4.1.

To estimate the number of excited ANFs, the AUCD was calculated by taking the integral of CDLDs over time. We applied linear regression techniques to the AUCD data and extracted the slope of the AUGF (number of fibers/CU) from the best-fit regression line. All signal processing was performed offline, with MATLAB (Mathworks 2019a, Natick, MA, USA).

4.2.3 Evaluation of Speech Perception

Speech perception was evaluated at predetermined intervals during a standard clinical follow-up. In this study, we analyzed the word recognition score, obtained in a quiet environment, at 1 year after implantation. Speech material comprised the standard Dutch speech test of the Dutch Society of Audiology. It consisted of phonetically balanced monosyllabic (CVC) word lists (Bosman & Smoorenburg, 1995), presented at 65 dB SPL in a quiet listening environment. To enhance test reliability, four lists (44 words) per condition were performed. All speech testing was conducted in a soundproof room, with a calibrated sound-speaker, with the patient in a frontal position at a meter distance. All patients used the HiRes processing strategy from Advanced Bionics.

4.2.4 Statistical Analysis

LMMs were constructed with the lme4 package in R (R version 3.6.1, The R Foundation for Statistical Computing, 2020). Word recognition outcomes were assumed to be the sum of fixed and random effects. Because random effects often introduce correlations between cases, they should be taken into account to elucidate the fixed effects, which affect the population. The LMM allowed the inclusion of potential confounding factors (Brauer & Curtin 2017; Bolker et al. 2009). Moreover, the LMM design accounted for missing data (Fitzmaurice et al. 2004; Netten et al. 2017).

LMMs were used to test the relationship between the word recognition score and the metrics based on CDLDs obtained from Eq. 4.1, the AUCD, and the slope of AUGF. Our dataset included only a single word recognition score per patient, but multiple eCAP measurements were obtained

in each patient (see Data Recordings). Therefore, each of the eight CDLD-related metrics was entered as the dependent variable in a separate LMM. In each of these models, the word recognition score was entered as a fixed covariate. Five additional fixed factors were included that could potentially affect the word recognition score and the CDLD-related parameters, including (1) the implant design, (2) the contact location along the electrode array, (3) the current level, (4) the age at implantation, and (5) the duration of deafness. The duration of deafness was defined as the time, in years, between the age at implantation and the age at which patients had experienced severe hearing loss, either in both ears or in the second ear. Data on the duration of deafness were available for 93 patients. The subject IDs were entered as random categorical variables, including a random intercept (Brauer & Curtin 2017). A p-value < 0.05 was considered to reflect a statistically significant difference.

To compare the CDLD-related parameters to the eCAP amplitude and the AGF slope in their abilities to explain the variance in word recognition scores, the corresponding R^2 was required. However, the LMMs did not produce an R^2 estimate. Thus, we performed simple linear regression, and we calculated the R^2 as the square of the coefficient of correlation (Neter et al. 1996; Khan et al. 2005). In these analyses, the parameters were averaged across all odd electrodes and/or suprathreshold current levels within each patient, as described in previous studies (e.g., Franck & Norton 2001; He et al. 2017).

To provide visual representations, word recognition scores were plotted against the corresponding CDLD-related parameters, the eCAP amplitude, and the AGF slope, which were averaged across electrodes and/or current levels within each patient. Of note, these plots did not completely match the analyses performed with LMMs, because the models took into account missing data points and random effects.

4.3 RESULTS

4.3.1 Derivation of CDLDs

We derived the CDLD from each eCAP waveform. Figure 4.3 shows three examples of eCAP waveforms and their corresponding CDLDs, each with two Gaussian components. Overall, the 95% confidence intervals of the goodness of fit (i.e., the normalized root mean square error) ranged from 0.91 to 0.96. Table 4.2 shows the mean values (with standard deviations) of the CDLD parameters.

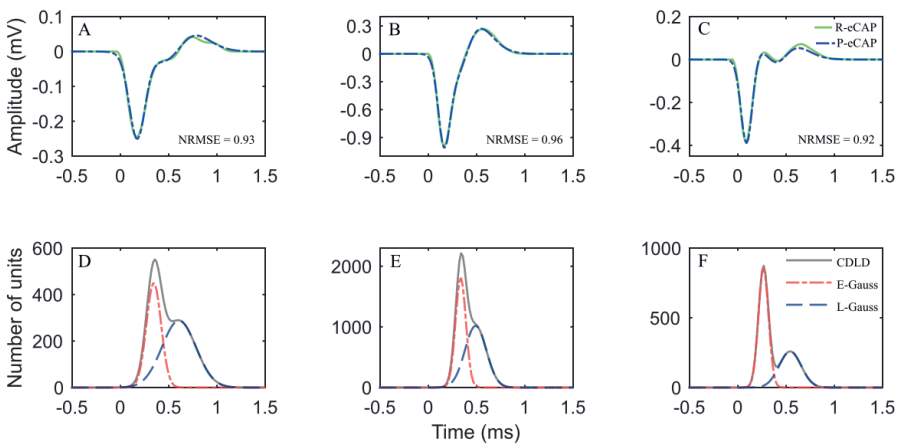

Fig. 4.3 Examples of eCAPs with different morphologies (upper row) and corresponding CDLDs (lower row). eCAP: electrically evoked compound action potential; R-eCAP: recorded eCAP; P-eCAP: predicted eCAP; CDLD: compound discharge latency distribution; E-Gauss: early Gaussian component; L-Gauss: late Gaussian component. NRMSE: normalized root mean square error.

4.3.2 Relationship between CDLDs and Speech Perception

At one year of follow-up, the average monosyllabic word score for the 124 adult patients with CIs was 60.8% ± 21.1% correct. Table 4.3 shows the parameter estimates for the eight LMMs, with the word recognition score as the independent variable and the CDLD parameters as dependent variables.

The LMM analysis revealed significant positive associations between α_1 and α_2 and the word recognition score (F (1, 117.1) = 8.7, p = 0.003; F (1, 117) = 5.6, p = 0.01, respectively). These outcomes suggested that patients with a higher word recognition score tended to have larger α_1 and α_2 values. Among the remaining factors, the implant design, current, and contact location showed a significant effect on α_1 and α_2 ($p < 0.05$), but the duration of deafness and age at implantation did not affect α_1 (p = 0.07; p = 0.25) or α_2 (p = 0.17; p = 0.51).

TABLE 4.2. CDLD parameters for eCAPs in patients with cochlear implants

Parameters	α_1	α_2	μ_1 (ms)	μ_2 (ms)	σ_1 (ms)	σ_2 (ms)	AUCD (number of fibers)	AUGF slope (number of fibers/CU)
Mean	710	553	0.37	0.59	0.076	0.16	484	0.52
SD	46	69	0.049	0.1	0.03	0.066	142	0.07

Means represent averaged values over all electrodes and/or over all stimulation levels and for all patients; CDLD: compound discharge latency distribution; eCAPs: evoked compound action potentials; AUCD: area under the CDLD curve; AUGF: the AUCD growth function.

The AUCD, an estimate of the number of excited ANFs in each recorded eCAP, was significantly correlated with the word recognition score (F (1,122.1) = 8.1, p = 0.005). This result indicated that when more ANFs were excited, better speech perception was achieved. The implant design, current level, and contact location showed significant effects on the AUCD (all $p < 0.01$), but the duration of deafness and age at implantation did not affect the AUCD (all $p > 0.2$).

The slope of the AUGF was significantly correlated with the word recognition score (F (1,122.1) = 8.7, p = 0.004). The AUGF slope was significantly affected by the electrode location ($p < 0.001$), but not by the other factors (all $p > 0.05$).

We found that the μ_1 and μ_2, reflecting the average firing latencies of excited ANFs, were not significantly associated with the word recognition score (F (1, 116) = 0.87, p = 0.82; F (1, 113.6) = 1.6, p = 0.2, respectively). The contact location showed a significant effect on μ_1 and μ_2 (both $p < 0.001$). The age at implantation had a positive effect on μ_2 (p = 0.02), but not on μ_1

(p = 0.53). The duration of deafness and the current level did not significantly affect μ_1 (p = 0.17 and p = 0.06, respectively) or μ_2 (p = 0.3 and p = 0.09, respectively).

The σ_1 and σ_2 represented the degree of neural synchronicity. The LMMs showed that σ_1 was significantly negatively associated with the word recognition score (F (1, 107.7) = 6.5, p = 0.01). However, σ_2 was not significantly associated with the word recognition score (F (1,113) = 3.5, p = 0.06). The implant design, current level, electrode location, and deafness duration showed significant effects on σ_1 and σ_2 (all p < 0.05). The age at implant showed a significant effect on σ_2 (p < 0.001), but not on σ_1 (p = 0.1).

TABLE 4.3. Parameter estimates from LMMs, with the word recognition score as the independent variable, and the CDLD parameters as dependent variables

Dependent variable	Estimate	SD	F	p-value
α_1	+18	5.6	8.7	0.003*
α_2	+13	5.4	5.6	0.01*
μ_1	-0.011	0.057	0.07	0.82
μ_2	-0.07	0.06	1.02	0.2
σ_1	-0.09	0.039	6.5	0.01*
σ_2	-0.1	0.052	3.5	0.06
AUCD	+15	5.1	8.1	0.005*
AUGF slope	+0.18	0.06	8.7	0.004*

*LMM: linear mixed model; CDLD: compound discharge latency distribution; AUCD: area under the CDLD curve; AUGF: the AUCD growth function; SD: standard deviation; *Significant difference.*

4.3.3 Abilities of CDLD Parameters, eCAP Amplitude, and AGF Slope to Explain the Variance in Speech Perception

We performed simple linear regression analyses to determine whether the CDLD-related

parameters explain R^2, the variability in the word recognition score better than the eCAP amplitude, and the slope of AGF (Table 4.4). For these analyses, the CDLD parameters were calculated for each individual patient as the average of all available eCAPs, across different electrode contacts and current levels. α_1 and α_2 showed R^2 values of 0.102 and 0.05, respectively (Fig. 4.4). The AUCD showed an R^2 value of 0.12 (Fig. 4.5A). The AUGF slope showed an R^2 value of 0.09 (Fig. 4.5B). μ_1 and μ_2 revealed small R^2 values, 0.0009 and 0.015, respectively. σ_1 showed a moderately high R^2 of 0.09 (Fig. 4.6A), but σ_2 showed a low value of 0.04 (Fig. 4.6B).

The eCAP amplitude, calculated for each individual patient as the average of all available eCAPs across different electrode contacts and current levels, showed an R^2 of 0.06 (Fig. 4.7A). The AGF slope showed an R^2 of 0.07 (Fig. 4.7B). It was calculated for each patient as the average of all available AGFs across different contacts.

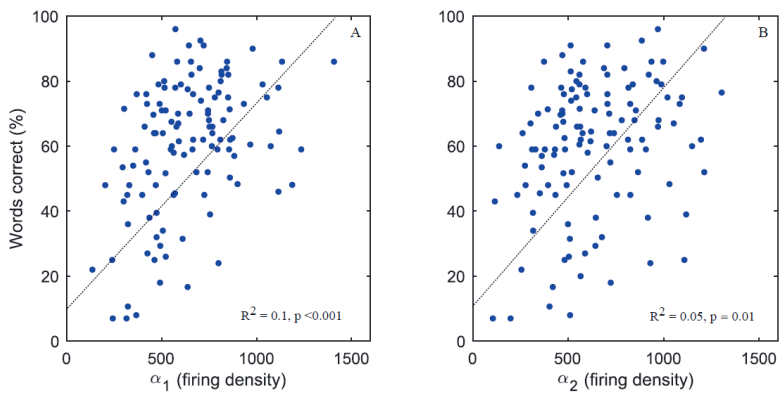

Fig. 4.4 Correlations between word recognition scores and firing density parameters. The percentage of words recognized by each individual patient are plotted against the corresponding α_1 (A) and α_2 (B) values, averaged across all contacts and all current levels. R^2 values are derived from the linear regressions (dotted lines).

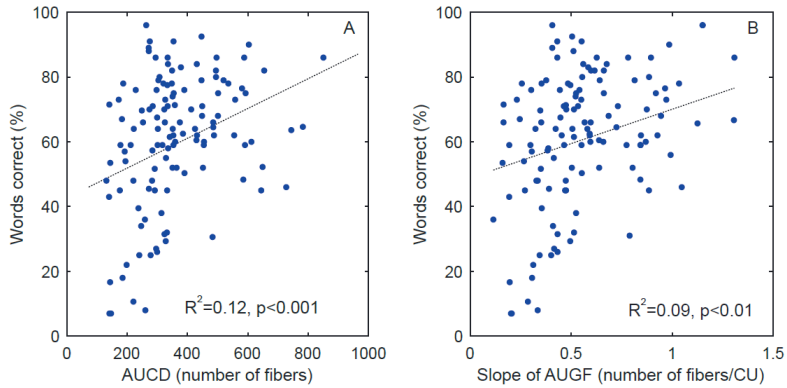

Fig. 4.5 Correlations between word recognition scores and the number of ANFs and AUGF slope. The percentage of words recognized by each individual patient are plotted against the corresponding AUCD (A) and AUGF slope (B), averaged across all contacts and/or all current levels. R^2 values are derived from the linear regressions (dotted lines). ANF: auditory nerve fiber; AUCD: area under the CDLD curve; CDLD: compound discharge latency distribution; AUGF: the AUCD growth function.

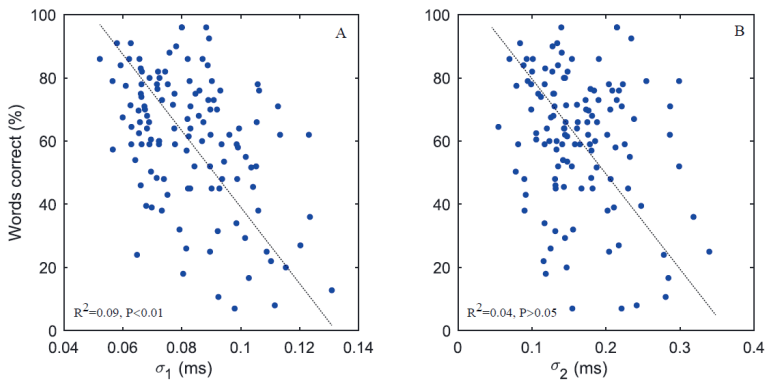

Fig. 4.6 Correlations between word recognition scores and neural synchronicity parameters. The percentage of words recognized by each individual patient are plotted against the corresponding σ_1 (A) and σ_2 (B) values, averaged across all contacts and all current levels. R^2 value is derived from the linear regression (dotted line).

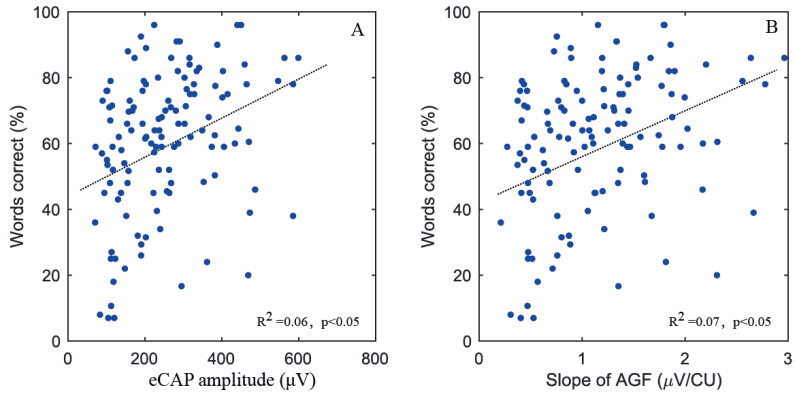

Fig. 4.7 Correlations between word recognition scores and eCAP parameters. The percentage of words recognized by each individual patient are plotted against the corresponding eCAP amplitude (A) and AGF slope (B), averaged across all electrodes and/or current levels. R^2 values are derived from the linear regressions (dotted lines). eCAP: electrically evoked compound action potential; AGF: amplitude growth function.

TABLE 4.4. Comparison of the abilities of different parameters to explain (R^2) the variance in speech performance in patients with cochlear implants

Parameters	R^2
α_1	0.1
α_2	0.05
μ_1	0.0009
μ_2	0.015
σ_1	0.09
σ_2	0.04
AUCD	0.12
AUGF slope	0.09
eCAP amplitude	0.06
AGF slope	0.07

AUCD: the area under the CDLD curve; CDLD: compound discharge latency distribution; AUGF: the AUCD growth function; eCAP: electrically evoked compound action potential; AGF: the eCAP amplitude growth function. R2 values are derived from the linear regressions.

4.4 DISCUSSION

This study was the first to test whether the CDLD (i.e., the number and the temporal firing

properties of excited ANFs in human eCAPs) was correlated with speech understanding. We showed that speech perception performance was significantly associated with the CDLD parameters related to the number of excited ANFs (α_1, α_2, AUCD), with the AUGF slope (i.e., the speed of the increase of the number of excited ANFs with increasing stimulus), and with early neural synchronicity (σ_1). The other three parameters (μ_1, μ_2 and σ_2) were not significantly correlated with speech recognition. Moreover, we found that the CDLD-based AUCD, AUGF slope, and the α_1 and σ_1 parameters provided a higher significance level than the two classically applied measures of eCAP (the amplitude and the AGF slope), in terms of predicting speech perception.

Results from post-mortem studies have suggested that patients with a greater number of surviving ANFs tended to perform better in speech recognition tests (e.g., Otte et al. 1978; Kawano et al. 1998; Khan et al. 2005; Seyyedi et al. 2014). After studies showed that eCAPs could be indicative of neural survival, interest increased in using eCAP measurements to evaluate correlations with speech perception (e.g., Shepherd & Javel 1997; He et al. 2017). However, needless to say, a direct comparison between the eCAP amplitude and the number of surviving ANFs in individuals with CIs was impossible. In this study, the temporal firing properties of excited ANFs extracted from the CDLD metrics in eCAPs (α_1, α_2, AUCD) provided a more accurate estimate of the number of functional ANFs than the eCAP amplitude (Dong et al. 2020), and the AUGF slope provided a more accurate rate of the increase of the number of excited ANFs with increasing stimulus than AGF slope. The significant associations between the word recognition score and these four metrics (Table 4.3) supported the notion that more functional fibers would provide better speech perception. According to the results in the present study, combined with those in previous animal studies, we conclude that the number of surviving ANFs played a significant role in speech perception performance. In other words, a larger number of healthy spiral ganglion cells could potentially lead to higher speech perception scores after cochlea implantation in a given patient.

Earlier studies have suggested that a decline in the synchronicity of the auditory neural response

might adversely influence speech understanding (e.g., Hellstrom & Schmiedt 1990; Pichora-Fuller et al. 2007). This theoretical expectation was substantiated for the first time in our study. Specifically, we showed that the σ_1 was negatively associated with speech perception (Table 4.3), that is, a more synchronous ANF response in the early CDLD peak (lower σ_1) was associated with better speech understanding. Moreover, although the σ_2 was not significantly associated with speech perception (p=0.06), a similar trend was observed (Fig. 4.6B). Our findings were consistent with previous findings that showed that a decline in the synchronicity of excited ANFs was associated with different factors (e.g., the duration of deafness, auditory nerve abnormalities, and myelin disorders) (Shepherd & Javel 1997; Rance 2005), and in turn, these factors may lead to a deterioration in CI speech outcomes. Our analysis of σ suggested that different eCAP waveforms with the same amplitudes, but different shapes could have clinical implications about neural synchrony and speech performance. That is, patients with narrower eCAP waveforms tended to have greater neural synchrony and better speech performance than those with wider eCAP waveforms.

To our knowledge, no previous study has reported that the peak latency of eCAPs was associated with speech perception performance in patients with CIs. Also in our study, we did not observe significant associations between the average firing latencies of excited ANFs in CDLDs (μ_1 and μ_2) and speech perception outcomes indicating that firing latencies of excited ANFs had little effect on speech perception (Table 4.3).

Previous studies have reported that patients with larger eCAP amplitudes and steeper AGF slopes tended to show better speech perception than their counterparts (e.g., Brown et al. 1990; Kim et al. 2010; DeVries et al. 2016). In line with their findings, we found that eCAP amplitudes and steeper AGF slopes were significantly associated with speech perception (Fig. 4.7). Compared with the eCAP amplitude and AGF slope we found that a similar proportion of the variance in speech perception could be explained by the α_1, AUCD, AUGF slope and σ_1 (Table 4.4), but because of the higher significance levels (Table 4.3 and Fig. 4.7), α_1, AUCD, AUGF slope and σ_1 might be better predictors of CI outcomes than the traditionally used eCAP amplitude and

AGF slope.

Of note, the CDLD parameters showed relatively low abilities to explain the variance in speech perception. Although this finding did not diminish the importance of the number and neural synchrony of excited ANFs, nevertheless, it suggested that a good number of nerves and good neural synchronicity alone would not be sufficient to guarantee a good CI outcome, because other factors must also play a role in speech recognition, including but not limited to the duration of deafness and cognitive ability (e.g., Fayad et al. 2006; He et al. 2017; Pisoni et al. 2017). In our data, we also observed that patients who have undergone a longer period of deafness showed significantly poorer speech perception performance than their counterparts. In these cases, the number of surviving peripheral fibers would be less relevant with speech recognition.

A reliable derivation of the temporal firing properties of ANFs in eCAPs was highly related to the shape of the human unitary response, as stated in Dong et al. (2020). The human unitary response has not been recorded in humans, and the one used in this study was estimated with iterative deconvolution by Dong et al. (2020, 2021) (Fig. 4.1B). In addition, the CDLD provides a valid estimate of the number of excited ANFs, only when the two components of CDLDs originate from two different groups of ANFs. However, this issue remains controversial, because the two CDLD components may, to some extent, originate from the same group of spiral ganglion cells (Ramekers et al. 2015; Konerding et al. 2020). For instance, the origin of the early component of CDLDs may be attributable to the direct excitation of the axonal process in the modiolus proximal to the spiral ganglion cell; and the origin of the late component of CDLDs may be attributable to the activation of the axonal process peripheral to the soma of the bipolar ganglion neuron (e.g., Stypulkowski & van den Honert 1984; Lai & Dillier 2000). Further anatomical and electrophysiological studies are warranted to obtain insight into the physiological mechanism underlying the unitary response and the CDLD. This knowledge could provide a deeper understanding of how the two CDLD components affect speech performance in individuals with CIs.

To date, eCAP measurements have proven to be useful in diagnosing and managing CI failures, although some discrepancies have been reported (Gantz et al. 1988; Hughes et al. 2004; van Eijl et al. 2017; DeVries et al. 2016; He et al. 2017). Our results demonstrated that the extraction of CDLDs from eCAP waveforms can provide additional clinical information, including the number and synchronicity of excited ANFs and how they affect speech understanding after cochlear implantation. Therefore, integrating the extraction of CDLDs into eCAP measurements may provide a potential predictor of CI outcomes.

4.5 CONCLUSIONS

The results of this study showed that, in individuals with CIs, speech perception after implantation was significantly associated with the number and synchronicity of excited ANFs, measured in eCAPs. We found that the CDLD-related parameters could explain a similar variance in speech perception but with a higher significance than the eCAP amplitude and the AGF slope. We conclude that eCAP-derived CDLD measurements, which reflect the temporal features of excited ANFs, could potentially serve as additional predictors of speech perception performance in individuals with CIs.

ACKNOWLEDGMENTS

The first author of the present study was financially supported by the China Scholarship Council. There are no conflicts of interest, financial, or otherwise.

Yu Dong designed and conducted experiments, analyzed data, and wrote the manuscript; Jeroen J. Briaire designed experiments, discussed the results and implications, and provided critical revision. H. Christiaan Stronks discussed the results and implications and provided critical revision; Johan H. M. Frijns discussed the results and implications and provided critical revision.

We are grateful to Nicolaas. R. A. van Groesen and Stefan Boehringer at the Leiden University Medical Center for statistical consultations on the data analysis. We would also like to thank Jan Dirk Biesheuvel for his assistance with preprocessing the raw eCAP data.

REFERENCES

Abbas, P. J., & Brown, C. J. (1991). Electrically evoked auditory brainstem response: refractory properties and strength-duration functions. *Hearing research*, *51*(1), 139-147.

Biesheuvel, J. D., Briaire, J. J., & Frijns, J. H. (2018). The precision of eCAP thresholds derived from amplitude growth functions. *Ear and hearing*, *39*(4), 701-711.

Bolker, B. M., Brooks, M. E., Clark, C. J., Geange, S. W., Poulsen, J. R., Stevens, M. H. H., & White, J. S. S. (2009). Generalized linear mixed models: a practical guide for ecology and evolution. *Trends in ecology & evolution*, *24*(3), 127-135.

Bosman, A. J., & Smoorenburg, G. F. (1995). Intelligibility of Dutch CVC syllables and sentences for listeners with normal hearing and with three types of hearing impairment. *Audiology*, *34*(5), 260-284.

Brauer, M., & Curtin, J. J. (2018). Linear mixed-effects models and the analysis of nonindependent data: A unified framework to analyze categorical and continuous independent variables that vary within-subjects and/or within-items. *Psychological Methods*, *23*(3), 389.

Brown, C. J., Abbas, P. J., & Gantz, B. (1990). Electrically evoked whole‐nerve action potentials: Data from human cochlear implant users. *The Journal of the Acoustical Society of America*, *88*(3), 1385-1391.

Cosetti, M. K., Shapiro, W. H., Green, J. E., Roman, B. R., Lalwani, A. K., Gunn, S. H., ... & Waltzman, S. B. (2010). Intraoperative neural response telemetry as a predictor of performance. *Otology & Neurotology*, *31*(7), 1095-1099.

DeVries, L., Scheperle, R., & Bierer, J. A. (2016). Assessing the electrode-neuron interface with the electrically evoked compound action potential, electrode position, and behavioral thresholds. *Journal of the Association for Research in Otolaryngology*, *17*(3), 237-252.

Dong, Y., Briaire, J. J., Biesheuvel, J. D., Stronks, H. C., & Frijns, J. H. M. (2020). Unravelling the Temporal Properties of Human eCAPs through an Iterative Deconvolution Model. *Hearing Research*, *395*, 108037.

Dong, Y., Stronks, H. C., Briaire, J. J., & Frijns, J. H. M. (2021). An iterative deconvolution model to extract the temporal firing properties of the auditory nerve fibers in human eCAPs. MethodsX, 8, 101240.

Fayad, J. N., & Linthicum, F. H. (2006). Multichannel cochlear implants: Relation of histopathology to performance. *Laryngoscope*, *116*(8), 1310–1320.

Fitzmaurice, G. M., Laird, N. M., & Ware, J. 2. (2004). Linear mixed effects models. *Applied longitudinal*

analysis, *1*, 187-236.

Franck, K. H., & Norton, S. J. (2001). Estimation of psychophysical levels using the electrically evoked compound action potential measured with the neural response telemetry capabilities of Cochlear Corporation's CI24M device. *Ear and Hearing*, *22*(4), 289-299.

Gantz, B. J., Tyler, R. S., McCabe, B. F., Tye-Murray, N., Lansing, C., Kuk, F., Knutson, J. F., Hinrichs, J., Woodworth, G., Abbas, P., & Brown, C. (1988). Evaluation of five different cochlear implant designs: Audiologic assessment and predictors of performance. In *Laryngoscope* (Vol. 98, Issue 10, pp. 1100–1106).

Garadat, S. N., Zwolan, T. A., & Pfingst, B. E. (2012). Across-site patterns of modulation detection: Relation to speech recognition. *The Journal of the Acoustical Society of America*, *131*(5), 4030–4041.

Goldstein, M. H., & Kiang, N. Y. S. (1958). Synchrony of Neural Activity in Electric Responses Evoked by Transient Acoustic Stimuli. *Jasa*, *30*(2), 107–114.

Hall, R. D. (1990). Estimation of surviving spiral ganglion cells in the deaf rat using the electrically evoked auditory brainstem response. *Hearing research*, *49*(1-3), 155-168.

He, S., Teagle, H. F. B., & Buchman, C. A. (2017). The electrically evoked compound action potential: From laboratory to clinic. *Frontiers in Neuroscience*, *11*(JUN), 1–20.

Hellstrom, L. I., & Schmiedt, R. A. (1990). Compound action potential input/output functions in young and quiet-aged gerbils. *Hearing research*, *50*(1-2), 163-174.

Hughes, M. L., Brown, C. J., & Abbas, P. J. (2004). Sensitivity and specificity of averaged electrode voltage measures in cochlear implant recipients. *Ear and hearing*, *25*(5), 431-446.

Khan, A. M., Handzel, O., Burgess, B. J., Damian, D., Eddington, D. K., & Nadol Jr, J. B. (2005). Is word recognition correlated with the number of surviving spiral ganglion cells and electrode insertion depth in human subjects with cochlear implants? *The Laryngoscope*, *115*(4), 672-677.

Kawano, A., Seldon, H. L., Clark, G. M., Ramsden, R. T., & Raine, C. H. (1998). Intracochlear factors contributing to psychophysical percepts following cochlear implantation. *Acta Oto-Laryngologica*, *118*(3), 313–326.

Kim, J. R., Abbas, P. J., Brown, C. J., Etler, C. P., O'Brien, S., & Kim, L. S. (2010). The relationship between electrically evoked compound action potential and speech perception: a study in cochlear implant users with short electrode array. *Otology & neurotology: official publication of the American Otological Society, American Neurotology Society [and] European Academy of Otology and Neurotology*, *31*(7), 1041.

Konerding, W., Arenberg, J. G., Kral, A., & Baumhoff, P. (2020). Late electrically-evoked compound

action potentials as markers for acute micro-lesions of spiral ganglion neurons. *Hearing Research*, 108057.

McKay, C. M., Chandan, K., Akhoun, I., Siciliano, C., & Kluk, K. (2013). Can ECAP measures be used for totally objective programming of cochlear implants?. *Journal of the Association for Research in Otolaryngology*, *14*(6), 879-890.

Miller, C. A., Abbas, P. J., & Robinson, B. K. (1994). The use of long-duration current pulses to assess nerve survival. *Hearing research*, *78*(1), 11-26.

Miller, C. A., Abbas, P. J., Rubinstein, J. T., Robinson, B. K., & Matsuoka, A. J. (1999). The neurophysiological effects of simulated auditory prosthesis stimulation.

Nadol Jr, J. B., Burgess, B. J., Gantz, B. J., Coker, N. J., Ketten, D. R., Kos, I., ... & Shallop, J. K. (2001). Histopathology of cochlear implants in humans. *Annals of Otology, Rhinology & Laryngology*, *110*(9), 883-891.

Neter, J., Kutner, M. H., Nachtsheim, C. J., & Wasserman, W. (1996). Applied linear statistical models.

Netten, A. P., Dekker, F. W., Rieffe, C., Soede, W., Briaire, J. J., & Frijns, J. H. (2017). Missing data in the field of otorhinolaryngology and head & neck surgery: need for improvement. *Ear and hearing*, *38*(1), 1-6.

Otte, J., Schuknecht, H. F., & Kerr, A. G. (1978). Ganglion cell populations in normal and pathological human cochleae. Implications for cochlear implantation. *The Laryngoscope*, *88*(8), 1231-1246.

Pfingst, B. E., Sutton, D., Miller, J. M., & Bohne, B. A. (1981). Relation of psychophysical data to histopathology in monkeys with cochlear implants. *Acta oto-laryngologica*, *92*(1-6), 1-13.

Pisoni, D. B., Kronenberger, W. G., Harris, M. S., & Moberly, A. C. (2017). Three challenges for future research on cochlear implants. *World journal of otorhinolaryngology-head and neck surgery*, *3*(4), 240-254.

Ramekers, D., Versnel, H., Strahl, S. B., Klis, S. F. L., & Grolman, W. (2015). Recovery characteristics of the electrically stimulated auditory nerve in deafened guinea pigs: Relation to neuronal status. *Hearing Research*, *321*, 12–24.

Rance, G. (2005). Auditory neuropathy/dys-synchrony and its perceptual consequences. *Trends in amplification*, *9*(1), 1-43.

Pichora-Fuller, M. K., Schneider, B. A., MacDonald, E., Pass, H. E., & Brown, S. (2007). Temporal jitter disrupts speech intelligibility: A simulation of auditory aging. *Hearing research*, *223*(1-2), 114-121.

Seyyedi, M., Viana, L. M., & Nadol Jr, J. B. (2014). Within-subject comparison of word recognition and spiral ganglion cell count in bilateral cochlear implant recipients. *Otology & neurotology: official*

publication of the American Otological Society, American Neurotology Society [and] European Academy of Otology and Neurotology, *35*(8), 1446.

Shepherd, R. K., & Javel, E. (1997). Electrical stimulation of the auditory nerve. I. Correlation of physiological responses with cochlear status. *Hearing Research*, 108(1–2), 112–144.

Strahl, S. B., Ramekers, D., Marjolijn M. B. Nagelkerke, K. E. S., Spitzer, P., Klis, S. F. L., Grolman, W., & Versnel, H. (2016). Assessing the Firing Properties of the Electrically Stimulated Auditory Nerve Using a Convolution Model. Adv Exp Med Biol, 894.

Stypulkowski, P. H., & van den Honert, C. (1984). Physiological properties of the electrically stimulated auditory nerve. I. Compound action potential recordings. Hearing Research, 14(3), 205–223. https://doi.org/10.1016/0378-5955(84)90051-0

Turner, C., Mehr, M., Hughes, M., Brown, C., & Abbas, P. (2002). Within-subject predictors of speech recognition in cochlear implants: A null result. *Acoustics Research Letters Online*, *3*(3), 95-100.

van de Heyning, P., Arauz, S. L., Atlas, M., Baumgartner, W. D., Caversaccio, M., Chester-Browne, R., ... & Skarzynski, H. (2016). Electrically evoked compound action potentials are different depending on the site of cochlear stimulation. *Cochlear implants international*, *17*(6), 251-262.

van den Honert, C., & Stypulkowski, P. H. (1984). Physiological properties of the electrically stimulated auditory nerve. II. Single fiber recordings. *Hearing Research*, *14*(3), 225–243.

van der Beek, F. B., Briaire, J. J., & Frijns, J. H. (2012). Effects of parameter manipulations on spread of excitation measured with electrically-evoked compound action potentials. *International journal of audiology*, *51*(6), 465-474.

van Dijk, J. E. van Olphen, A. F. Langereis, M. C. Mens, L. H. M. Brokx, J. P. L. & Smoorenburg, G. F. (1999). Predictors of cochlear implant performance. International Journal of Audiology, 38(2), 109–116.

van Eijl, R. H., Buitenhuis, P. J., Stegeman, I., Klis, S. F., & Grolman, W. (2017). Systematic review of compound action potentials as predictors for cochlear implant performance. *The Laryngoscope*, *127*(2), 476-487.

Versnel, H., Prijs, V. F., & Schoonhoven, R. (1992). Round-window recorded potential of single-fibre discharge (unit response) in normal and noise-damaged cochleas. *Hearing Research*, *59*(2), 157–170.

Chapter 5

Short and long-latency components of the eCAP reveal different refractory properties

Yu Dong, Jeroen J. Briaire, H. Christiaan

Stronks and Johan H. M. Frijns

Submitted to Hearing Research

Abstract

Background: The refractory recovery function (RRF) measures the electrically evoked compound action potential (eCAP) in response to a second pulse (probe) after masking by a first pulse (masker). This RRF is usually used to assess the refractory properties of the electrically stimulated auditory nerve (AN) by recording the eCAP amplitude as a function of the masker probe interval. Instead of assessing eCAP amplitudes only, recorded waveforms can also be described as a combination of a short-latency component (S-eCAP) and a long-latency component (L-eCAP). It has been suggested that these two components originate from two different AN fiber populations with differing refractory properties. The main objective of this study was to explore whether the refractory characteristics revealed by S-eCAP, L-eCAP, and the raw eCAP (R-eCAP) differ from each other. For clinical relevance, we compared these refractory properties between children and adults and examined whether they are related to cochlear implant (CI) outcomes.

Design: In this retrospective study, the raw RRF (R-RRF) was obtained from 121 Hi-Focus Mid-Scala or 1J cochlear implant (Advanced Bionics, Valencia, CA) recipients. Each R-eCAP of the R-RRF was split into an S-eCAP and an L-eCAP using deconvolution to produce two new RRFs: S-RRF and L-RRF. The refractory properties were characterized by fitting an exponential decay function with three parameters: the absolute refractory period (T); the saturation level (A); and the speed of recovery from nerve refractoriness (τ), i.e., a measure of the relative refractory period. We compared the parameters of the R-RRF (T_R, A_R, and τ_R) with those obtained from the S-RRF (T_S, A_S, and τ_S) and L-RRF (T_L, A_L, and τ_L) and investigated whether these parameters differed between children and adults. In addition, we examined the associations between these parameters and speech perception in adults with CI. Linear mixed modeling was used for the analyses.

Results: We found that T_R was significantly longer than T_S and T_L, and T_S was significantly longer than T_L. A_R was significantly larger than A_S and A_L, and A_S was significantly larger

than A_L. Also, τ_S was significantly longer in comparison to τ_R and τ_L, but no significant difference was found between τ_R and τ_L. Children presented a significantly larger A_S and A_L and a shorter T_R and T_S in comparison to adults. Shorter τ_S was significantly associated with better speech perception in adult CI recipients, but other parameters were not.

Conclusion: We demonstrated that the two components of the eCAP have different refractory properties and that these also differ from those of the R-eCAP. In comparison with the R-eCAP, the refractory properties derived from the S-eCAP and L-eCAP can reveal additional clinical implications in terms of the refractory difference between children and adults as well as speech performance after implantation. Thus, it is worthwhile considering the two components of the eCAP in the future when assessing the clinical value of the auditory refractory properties.

Keywords: Cochlear implants, auditory nerve, sensorineural hearing loss, refractory recovery, electrically evoked action potential, speech perception

5.1 Introduction

A cochlear implant (CI) is an intracochlear device that can partially restore the hearing functionality of patients with severe-to-profound hearing loss. A CI transforms a sound signal into electrical stimuli that directly activate the auditory nerve (AN) inside the cochlea (Hughes, 2012). Previous studies reported that the neural refractoriness of the AN can affect its capability of accurately encoding temporal information (e.g., Gray, 1967; Wilson et al., 1994; Brown et al., 1990; Boulet et al., 2015; He et al., 2017) and is relevant to the functionality of the AN as well as speech perception (e.g., Stypulkowski and van den Honert, 1984; Wilson et al., 1994; He et al., 2017).

A common approach to exploring the refractory characteristics of the AN is to measure the refractory recovery function (RRF) of the electrically evoked compound action potential (eCAP) using a masker-probe artifact cancellation paradigm. In this paradigm, two pulses are applied, and the eCAP in response to the second pulse (the probe) is measured as a function of the masker

probe interval (MPI). The RRF can be obtained by plotting the eCAP amplitudes as a function of MPI (Miller et al., 2000; Morsnowski et al., 2006; Hey et al., 2017). Refractoriness arising from the first pulse (the masker) results in a masking of the eCAP triggered by the probe. In this paradigm, the eCAP is characterized by the amplitude of the main peaks, namely the difference between the first negative peak (N1) and the first positive peak (P1). The refractory properties of the AN can be obtained by fitting the RRF with an exponential function using three parameters: (1) the absolute refractory period (T); (2) the eCAP amplitude at the maximum saturation level (A); and (3) the relative refractory period (τ), which refers to the speed of recovery from relative refractoriness (e.g., Morsnowski et al., 2006; Botros and Psarros, 2010; He et al., 2017).

However, the method used in previous studies to assess the AN refractoriness is controversial (e.g., Miller et al., 2000; Morsnowski et al., 2006), because in this paradigm, the eCAP is characterized only by the amplitude of the main peaks. In considering the morphology of eCAPs, previous studies have observed two different types of eCAP waveforms (e.g., Van den Honert and Stypulkowski, 1984; Lai and Diller, 2000; Ramekers et al., 2015; van de Heyning et al., 2016; Dong et al., 2020). These waveforms can consist of either one negative and one positive peak or of two positive peaks that are similar in shape but differ in latencies (P1 and P2) (e.g., Lai and Dillier, 2000; He et al., 2017). The raw eCAP waveform (R-eCAP) can be described as a combination of a short-latency component (S-eCAP) and a long-latency component (L-eCAP). They may be attributed to a separate neural response of part of the AN fiber (ANF) population (Ramekers et al., 2015; Strahl et al., 2016; Konerding et al., 2020; Dong et al., 2020). This two-component concept was also supported by a single-fiber recording study in cats (Van den Honert and Stypulkowski, 1984). More importantly, the two groups of neural responses can be related to the survival and functional conditions of the AN. For instance, Strahl et al. (2016) suggested that the ratio between S-eCAP and L-eCAP can potentially indicate the survival condition of the AN. Stypulkowski and van den Honert (1984) reported that the refractory characteristics from the L-eCAP may be indicative of degeneration of the peripheral processes of the AN fibers based on their results recorded in cats. However, previous studies have not investigated whether the S-

eCAP and L-eCAP reveal different auditory refractory properties. We assumed that these two components arise from two different populations of ANFs, and therefore they may exhibit different refractory characteristics. Thus, in this study, we investigated the auditory refractory properties of the AN underlying the S-eCAP and L-eCAP.

Variation in terms of refractory characteristics of the AN between individuals and between different etiologies of deafness has been previously reported (e.g., Gantz et al., 1994; Fulmer et al., 2011; Van Eijl et al., 2017; He et al., 2017). Due to factors such as the duration of deafness and the maturation of the AN, differences in auditory refractory characteristics may be expected between young and adult CI users. For instance, in an animal study, the absolute refractory period of individual rat auditory neurons increased with the duration of deafness (Shepherd et al., 2001, 2004). Thus, a shorter absolute refractory period in children was anticipated, as children usually underwent a shorter duration of deafness in comparison to adults. To our knowledge, this has only been investigated by Carvalho et al. (2015), who reported no difference in refractory characteristics between children and adults except for the maximum saturation level. More importantly, earlier studies have not explored whether the auditory refractory characteristics underlying S-eCAP and L-eCAP in adults differ from or are the same as those in children.

Previous studies have attempted to explore whether the AN's speed of recovery from refractoriness is associated with the speech outcomes of adult CI recipients. These studies have not reported the effects of the absolute refractory period and saturation level on speech recognition, and results on the speed of recovery have been inconsistent. Some studies have reported that faster recovery from refractoriness derived from R-eCAP associates with better speech performance scores (Brown et al., 1990; Kiefer et al., 2001; Battmer et al., 2005; Fulmer et al., 2010), while other studies did not find such a relation (Abbas et al., 1991; Turner et al., 2002; Batter et al., 2005; Lee et al., 2012). One likely reason behind the incongruity is that previous studies only focused on the R-eCAP without considering the S-eCAP and L-eCAP separately.

Based on the above considerations, the first goal of the present study was to explore whether different refractory properties could be identified for the two components of the R-eCAP waveforms. To this end, the eCAP waveforms of the raw RRFs (R-RRFs) in a large group of CI patients were split into an S-eCAP and L-eCAP using iterative deconvolution (Dong et al., 2021). Using this method, two derived RRFs (S-RRF and L-RRF) were obtained from the R-RRFs, and the T, A, and τ parameters of the R-RRF, S-RRF and L-RRF were compared. Then, we investigated the potential clinical relevance of these refractory parameters, including (1) whether the parameters of the S-RRF, L-RRF, and R-RRF in children differed from those obtained from adult CI recipients and (2) whether these parameters can be indicative of speech outcomes in adult CI recipients.

5.2 MATERIAL AND METHODS

5.2.1 Patients

This retrospective study included 121 patients from the Leiden University Medical Centre (Leiden, the Netherlands) who received a CI between January 2010 and December 2015, and from whom intraoperative RRF recordings were available. These patients received a HiRes90K device (Advanced Bionics, Valencia, CA), either with a Mid-Scala or a 1J electrode array. Sixteen patients were excluded because of poor signal quality of eCAPs and failure of RRF fitting (see Data Recordings and Analysis) and the remaining 105 patients were included for further analyses. Table 5.1 shows the characteristics of the included patients.

5.2.2 Data recordings

The RRF recordings were conducted using a masker-probe artifact cancellation paradigm (Miller et al., 2000), which was provided by the Research Studies Platform Objective Measures software (Advanced Bionics, Valencia, CA). A schematic of this paradigm is shown in Figure 5.1. In this method, the masker-probe interval (MPI) systematically varies from 300 to 8000 μs. The evoked

eCAP response to the partially masked probe (trace A) is recorded by a contact that is two electrodes apical to the stimulus. As the MPI increases, the AN gradually recovers from the refractory status induced by the masker, which leads to larger eCAPs at longer MPIs in trace A. The neural response and artifact evoked by the masker are measured (trace B). The artifact and the eCAP evoked by the probe pulse are derived by subtracting trace B from trace A (i.e., A-B). The reference MPI is set to minimize the neural response evoked by the probe pulse (trace C) (Morsnowski et al., 2006). Subtracting trace D from trace C (i.e., C-D) yields the artifact induced by the probe. The difference between the two derived traces (i.e., (A-B)-(C-D)) is the eCAP evoked by the first probe. The RRF was obtained by plotting the eCAP amplitudes as a function of MPIs. In the present study, the RRF recording was obtained using 13 MPIs (300, 398, 538, 721, 969, 1293, 1734, 2327, 3114, 4181, 5603, 750, 7995 µs).

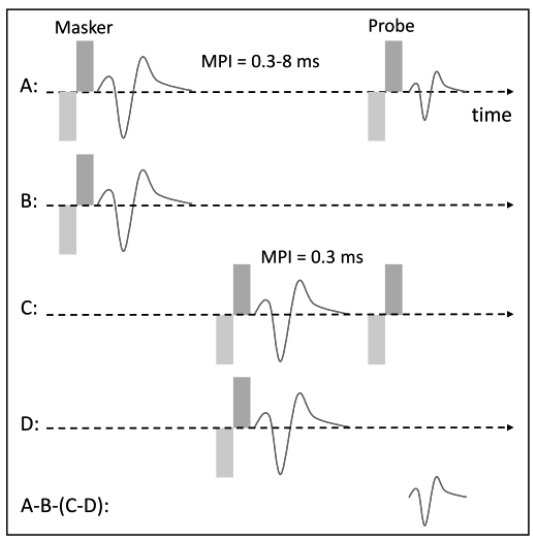

Fig. 5.1. A schematic illustration of the masker-probe artifact cancellation paradigm for measuring the eCAP refractory recovery function. Red solid lines indicate eCAP response. Colored rectangles indicate biphasic current pulses. Adapted from Miller et al. (2000). eCAPs: electrically evoked compound action potentials. MPI: masker probe interval.

The electrode arrays used in this study consisted of 16 contacts that were numbered from 1 to 16 in apical-to-basal order. RRF measurements were obtained at an apical electrode (E3), a middle

position (E8), and a basal position (E14). Due to time constraints in the operating theater, not all contacts could be recorded in all patients. Three stimulation electrode sites were recorded for 64 patients, two stimulation electrode sites (E3, E8) were recorded for 29 patients, and one stimulation site (E3) was recorded for 28 patients. The eCAPs were evoked using monopolar, charge-balanced, cathodic-first biphasic pulses (32 µs/phase) and recorded with a sampling rate of 56 kHz and a gain of 300. Raw eCAP recordings were low-pass filtered with a cutoff frequency of 8 kHz. N1 was defined as the minimum within the period from 180 to 490 µs, and P1 was the maximum from 470 to 980 µs after the end of stimulation. The eCAP amplitude was defined as the voltage difference between P1 and N1. The noise level was set to the average of the tail section of the recorded eCAP, i.e., the last 30 samples of the response. The signal-to-noise ratio was defined as the eCAP amplitude divided by the noise (Biesheuvel et al., 2017). eCAPs were in-or excluded using a semiautomatic method programmed using MATLAB (Mathworks 2019a, Natick, MA, USA), including two criteria: the eCAP amplitude had to be larger than 30 µV and the SNR had to exceed +15 dB. If the eCAPs did not meet both of these criteria, they were excluded. To ensure reliability, a stimulation site was excluded if more than 3 out of 13 eCAP waveforms of each R-RRF sequence did not meet these two criteria. As a result, 35 stimulation sites were excluded and the remaining 243 R-RRFs were used for extracting the S-RRF and L-RRF (see below).

5.2.3 Analysis

5.2.3.1 Extracting the S-eCAP and L-eCAP from the recorded eCAP

Under the assumption that each ANF generates the same unitary response, the R-eCAP can be described as a convolution of the unitary response with a compound discharge latency distribution consisting of two Gaussian components (for details, see Dong et al., 2021). The two Gaussian components represent the discharge latency distribution of the S-eCAP and the L-eCAP, respectively. To extract the S-eCAP and L-eCAP from the R-eCAP, two steps were performed. First, combined with a human unitary response, the compound discharge latency distribution was

derived from the R-eCAP using an iterative deconvolution model (Dong et al., 2020, 2021). Second, the S-eCAP and L-eCAP were simulated by convolving the first and second components of the compound discharge latency distribution with the human unitary response, respectively. The summation between the S-eCAP and L-eCAP mathematically equals the R-eCAP. We examined if this summation can accurately simulate the R-eCAP waveform by calculating the normalized root mean square error using MATLAB (Mathworks 2019a, Natick, MA, USA). Then, we determined the amplitudes of the S-eCAP and L-eCAP in the same manner as the R-eCAP amplitude. The S-RRF and L-RRF were obtained by plotting the amplitudes of S-eCAP and L-eCAP as a function of MPIs.

5.2.3.2 Deriving the refractory properties from R-RRF, S-RRF, and L-RRF

An exponential decay function was used to characterize the R-RRF, S-RRF, and L-RRF (e.g., Matsuoka et al., 2001; Morsnowski et al., 2006; Fulmer et al., 2010; Boulet et al., 2015).

$$RRF\ (MPI) = A * (1 - e^{(-\frac{(MPI-T)}{\tau})}) \quad (1)$$

T is the absolute refractory period (in μs), i.e., the minimum MPI for which an eCAP can be triggered by the probe. The amplitude recovers to the saturation level A (in μV) with a speed-of-recovery time constant τ (in μs). That is, τ represents the relative refractory period, reflecting the speed of recovery from relative refractoriness. T_R, A_R, and τ_R denote the parameters of R-RRF; T_S, A_S, and τ_S are those of S-RRF; and T_L, A_L, and τ_L are those of L-RRF. These parameters were calculated by fitting the R-RRF, S-RRF, and L-RRF using a least-squares curve fit with the Levenberg-Marquart algorithm using MATLAB (Mathworks 2019a, Natick, MA, USA). As the absolute refractory period cannot be shorter than 0 μs, a stimulation site was excluded if any one of the parameters (T_R, T_S, or T_L) was smaller than 0 μs, indicating a fitting error. As a result, 28 stimulation sites were excluded, and the remaining 215 sites originating from 105 patients were included for further statistical analyses.

5.2.4 Speech perception

Speech perception, defined as the word and phoneme recognition score obtained one year after implantation, was routinely evaluated for the adult CI recipients. The HiRes processing strategy from Advanced Bionics was applied to all patients. The speech material was presented at 65 dB SPL in a quiet listening environment. All speech testing was conducted in a soundproof room, using a calibrated sound speaker in a frontal position at a meter distance. The standard Dutch speech test of the Dutch Society of Audiology, consisting of phonetically balanced monosyllabic (CVC) word lists, was applied (Bosman & Smoorenburg, 1995). To enhance test reliability, four lists of 11 CVC words were administered. The number of words and phonemes that were correct was determined.

5.2.5 Statistics

In the present study, we used linear mixed modeling (LMM) for statistical analysis, because (1) LMMs have the advantage that they can account for random effects (e.g., between-subject variability), and (2) LMMs can also account for missing data that do not have to be random (Molenberghs et al., 1997; Fitzmaurice et al., 2004). We first tested whether the short and long-latency components of the eCAP reveal different refractory characteristics and whether they differ from those revealed by the raw eCAP waveform. To this end, three LMMs were constructed with each of the refractory parameters (i.e., T, A, and τ) as the dependent variable. To test whether the parameters derived from S-RRF and L-RRF differ from each other and from the ones obtained from R-RRF, a categorical fixed factor was introduced that reflected whether T, A, and τ were obtained from R-RRF, S-RRF, or L-RRF. An example model for parameter A is given as follows:

$$A = RSL + contact + 1|subject\ ID \qquad (5.2)$$

where A is the dependent variable; RSL is the categorical variable with three levels (R, S, and L)

corresponding to R-RRF, S-RRF, and R-RRF; the contact with the levels (E3, E8, and E14) is entered as a fixed-effect variable; and subject ID is entered as a random categorical variable, including a random intercept (Brauer and Curtin, 2018). The significance level of each comparison was adjusted to 0. 017 using post hoc Bonferroni-corrected multiple comparisons t-testing (0.05 divided by 3 comparisons).

Then, we evaluated the clinical relevance of the refractory parameters derived from R-RRF, S-RRF, and L-RRF. To compare the refractory characteristics between children and adults, nine LMMs were constructed that incorporated the following dependent variables: T_R, A_R, τ_R, T_S, A_S, τ_S, T_L, A_L, and τ_L. In these analyses, the 106 patients were classified into a child group (<=16 years, n=42) and an adult group (>16 years, n=64) by age (see Table 5.1). This categorical variable was entered as a fixed effect factor with two levels (i.e., pediatric and adult). The electrode contact number and subject ID were entered in the same way as Eq. (5.2).

In addition, we investigated whether the refractory parameters obtained from R-RRF, S-RRF, and L-RRF are related to the speech perception of adult CI recipients. Again, nine LMMs were constructed in which the adults' speech performance was compared with the refractory parameters T_R, T_S, T_L, A_R A_S, A_L, τ_R, τ_S, and τ_L, respectively. In our data set, only a single speech score was available, but we had multiple measures for the refractory metrics. We used reverse LMM constructions; that is, T_R, T_S, T_L, A_R A_S, A_L, τ_R, τ_S, and τ_L were entered as the dependent variable and the monosyllabic word score was entered as a fixed covariate in each model. The electrode contact and subject ID were included as a fixed-effect variable and a random variable, respectively (see Eq. (5.2)). Additionally, the relationship between phoneme score and the refractory parameters was evaluated in the same way. LMM analyses were carried out using the lme4 package in R (R version 3.6.1, The R Foundation for Statistical Computing, 2020).

TABLE 5.1. Patient demographics

Number of Patients	105
Cochlear implant type (n)	
HiRes90K 1J	14
HiRes90K Mid-Scala	91
Age (years)	
Children (<16 years)	42
Mean age ± SD (years)	5.2±3.6
Adults (> =16 years)	63
Mean age ± SD (years)	61.8 ±15.9
Etiology (n)	
Medication	1
Meningitis	7
Otosclerosis	2
Congenital/Hereditary	35
Other/Unknown	60

SD represents standard deviation.

5.3 RESULTS

5.3.1 Extraction of S-eCAP and L-eCAP from R-eCAP

Each of the 2188 R-eCAP waveforms from 215 R-RRFs was split into an S-eCAP and an L-eCAP using iterative deconvolution. To test the validity of the deconvolution routine, the R-eCAPs were reconstructed from the S-eCAP and the L-eCAP by summation. The sum of the S- and L-eCAPs accurately reconstructed the R-eCAP, with median goodness of fit (i.e., the normalized root-mean-square error) of 91.7% (95% confidence interval: 89.5%–95.7%). A typical example of the extraction of the S-eCAP and L-eCAP is shown in Fig. 5.2. In this example, the summation of the S-eCAP and the L-eCAP matched the R-eCAP with a goodness of fit of

92.4%. One can directly see from this example that the latencies from the S-eCAP and L-eCAP are different, but also that the amplitude is far from that of the R-eCAP waveform. This illustrates that part of the response is canceled out of the summation of the responses due to the latency differences.

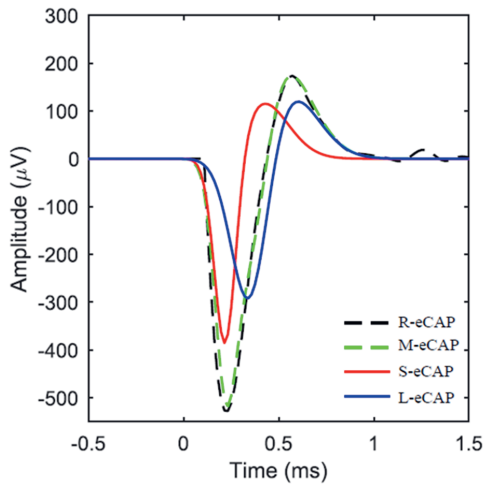

Fig. 5.2. A typical example of extracting the short-latency component (S-eCAP, the red solid line) and long-latency component (L-eCAP, the blue solid line) from the raw eCAP (R-eCAP, the black dashed line) of the raw eCAP refractory recovery function (R-RRF). The modeled eCAP (M-eCAP, the green dashed line) indicates the summation of the S-eCAP and the L-eCAP. eCAP: electrically evoked compound action potential.

5.3.2 The refractory parameters derived from the R-RRF, S-RRF, and L-RRF

Table 5.2 shows a descriptive analysis of the refractory parameters extracted from the R-RRF, S-RRF, and L-RRF, including measurements of central tendency (mean and median), and dispersion (median deviation). An example of the exponential fitting of the R-RRF, S-RRF, and L-RRF is shown in Fig. 5.3.

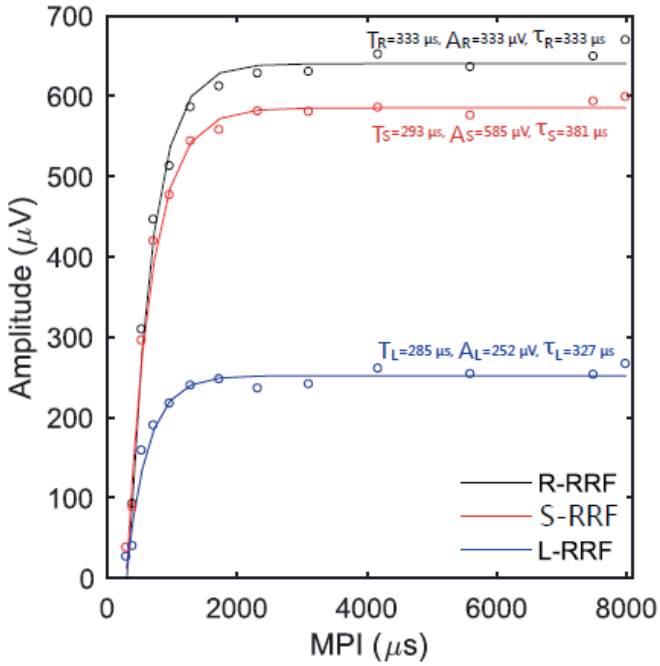

Fig. 5.3. Fitting the exponential model to the R-RRF, S-RRF, and L-RRF. R-RRF represents the recorded eCAP refractory recovery function; S-RRF and L-RRF represent the refractory recovery function of the short-latency and long-latency components in eCAPs. T is the absolute refractory period (in μs); A is the maximum eCAP amplitude at the maximum saturation level (in μV), and τ is the recovery time constant during the relative refractory period (in μs). T_R, A_R, and τ_R are for the R-RRF; T_S, A_S, and τ_S are for the S-RRF; T_L, A_L, and τ_L are for the L-RRF. MPI: the masker-probe interval. R-eCAP, S-eCAP, and L-eCAP are the same as for Fig. 5.1.

To test whether the refractory parameters derived from R-RRF, S-RRF, and L-RRF differed from each other, three LMMs were constructed for which T, A, and τ were entered as the dependent variable, respectively. In addition, a fixed variable was included that indicated whether R-RRF, S-RRF, or L-RFF was tested. All three LMMs showed a significant main effect of this fixed, categorical variable (T: $F(2, 547)=81.2$, $p<0.0001$; A: $F(2, 536)=299$, $p<0.0001$; and τ: $F(2,537)=4.1$, $p=0.004$, respectively). The contact number showed a significant effect on parameter T ($p=0.04$), A ($p<0.0001$) and τ ($p=0.02$).

Table 5.2. Descriptive statistics of the refractory parameters of the R-RRF, S-RRF, and L-RRF.

R-RRF, S-RRF, and L-RRF are the same as for Fig. 5.3. T_R, A_R, and τ_R are for the R-RRF; T_S, A_S, and τ_S are for the S-RRF; T_L, A_L, and τ_L are for the L-RRF. MD represents the median absolute deviation.

Refractory variables	Mean	Median	MD
T_R (μs)	368	366	85
T_S (μs)	306	300	29
T_L (μs)	285	229	38
A_R (μV)	432	390	159
A_S (μV)	426	385	164
A_L (μV)	220	184	105
τ_R (μs)	427	272	85
τ_S (μs)	529	338	211
τ_L (μs)	430	274	251

To compare how the refractory parameters T, A, and τ differed between the R-RRF, S-RRF, and L-RRF (see Eq. (5.2)), we used a post hoc t-test where the significance level was Bonferroni corrected to 0.017 (0.05 divided by 3 comparisons). For the absolute refractory period, $\mathbf{T_R}$ was significantly longer than $\mathbf{T_S}$ ($p<0.001$) and $\mathbf{T_L}$ ($p<0.001$), and $\mathbf{T_S}$ was significantly longer than $\mathbf{T_L}$ ($p<0.001$). Regarding saturation level, $\mathbf{A_R}$ was significantly larger than $\mathbf{A_S}$ ($p=0.011$) and $\mathbf{A_L}$ ($p<0.0001$), and $\mathbf{A_S}$ was significantly larger than $\mathbf{A_L}$ ($p<0.0001$). For the speed of recovery, we found that $\boldsymbol{\tau_S}$ was significantly longer than $\boldsymbol{\tau_R}$ ($p<0.01$) and $\boldsymbol{\tau_L}$ ($p<0.01$), and no significant difference was observed between $\boldsymbol{\tau_R}$ and $\boldsymbol{\tau_L}$ ($p=0.87$).

5.3.3 Comparisons of refractory parameters between children and adults

Table 5.3 shows the results of the descriptive analyses of the parameters between the two groups. We tested whether children and adults had different refractory characteristics by constructing nine LMMs with T_R, A_R, τ_R, T_S, A_S, τ_S, T_L, A_L, and τ_L entered as a dependent variable. For the absolute refractory period, T_R and T_S in children are significantly shorter than those in adults (T_R: $F(1, 92.3) = 10.4$, $p = 0.002$;), except for T_S ($F(1, 94.7) = 0.3$, $p = 0.9$) and T_L ($F(1, 95) = 0.19$, $p = 0.66$). Also, the saturation levels in children were significantly larger than those

of adults (A_R: F(1, 96.5) = 5.0, p = 0.03; A_S: F(1, 97.8) = 4.4, p = 0.04) except for A_L (F(1, 102) = 4.1, p = 0.046). Regarding the relative refractory period, no significant difference was observed between the two groups (τ_R: F(1, 102.8) = 3.9, p = 0.05; τ_S: F(1, 101) = 0.8, p = 0.38; and τ_L: F(1, 105) = 0.9, p = 0.35). The contact number showed a significant effect on parameters A_R, A_S, A_L (p<0.0001) and τ_R (p=0.02) but not on parameters T_R, T_S, τ_S, T_L, and τ_L (all p>0.05).

Table 5.3. Descriptive results of the refractory parameters of children and adults. The parameters are the same as for Table 5.2. MD represents the median absolute deviation.

Variables	Children			Adults		
	Median	Mean	MD	Median	Mean	MD
T_R (μs)	349	334	101	392	392	92.5
T_S (μs)	352	353	93.3	397	401	70.5
T_L (μs)	370	360	110	405	428	85.8
A_R (μV)	446	470	67	353	393	178
A_S (μV)	438	452	118	339	375	181
A_L (μV)	224	218	71.9	157	181	63.7
τ_R (μs)	286	438	210	294	350	199
τ_S (μs)	208	347	273	237	229	182
τ_L (μs)	209	389	245	276	332	224

5.3.4 Relations between refractory parameters and speech perception

Nine LMMs were constructed to evaluate the association between speech perception and the refractory parameters (T_R, T_S, T_L, A_R A_S, A_L, τ_R, τ_S, and τ_L) in adult CI recipients by entering them as the dependent variable and the speech score as a fixed covariate in each model, respectively. The average word recognition score at the one-year follow-up in the 40 adult patients with CI was 58% words correct (range from 17% to 92%) and 72% phonemes correct (range from 46% to 98%). We found that only τ_S was significantly and negatively associated with word recognition score (F(1, 53.2) = 6.5, p = 0.017) and phoneme score (F(1, 51.2) = 3.1,

p = 0.04), taking contact location along the electrode array into consideration (Fig. 5.4). That is, patients with a higher speed of recovery of the S-eCAP tend to have better speech perception. However, regarding the remaining parameters, no significant associations were observed (all p>0.2). In these LMMs, the contact number showed a significant effect on parameters A_R, A_S, and A_L (p<0.001) but not on the other parameters (all p>0.1).

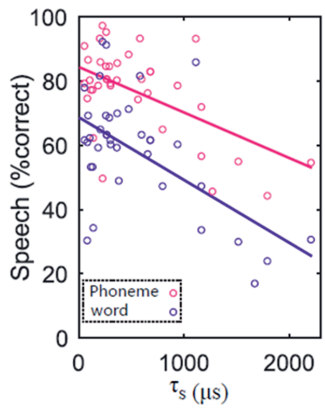

Fig. 5.4. Correlations between speech performance and the speed of recovery, τ_S. Scatterplots of recovery time constants (x-axis) plotted against the speech performance (y-axis).

5.4 DISCUSSION

Earlier studies suggested that human eCAPs include a short-latency component and a long-latency component, which are thought to arise from two different populations of ANFs. In the present study, we corroborated these findings by demonstrating the presence of two separate components in the human eCAP that have refractory characteristics that differ significantly from each other and from the raw eCAP. The refractory properties derived from S-RRF and L-RRF turned out to be of clinical relevance, because they differed significantly between children and adults and were significantly correlated with speech perception after cochlear implantation.

5.4.1 The refractory properties derived from the R-RRF, S-RRF, and L-RRF

We observed that the mean value of T_R was 368 μs and the mean value of τ_R was 427 μs

(Table 5.2). Previous studies reported mean or median values of T_R and τ_R ranging from 276 to 650 μs and from 410 to 1480 μs, respectively (Dynes, 1996; Bruce et al., 1999; Boulet et al., 2015; Viemes et al., 2016; Carvalho et al., 2020); thus, we conclude that our results fall within the ranges reported in the existing literature. The refractory parameters of the S-eCAP and L-eCAP were significantly different from each other, and importantly, they were significantly different from those obtained from the R-RRF, except for τ_R and τ_L. These findings support the notion that the short-latency and long-latency components of the eCAP can be attributed to two different populations of ANFs with different refractory characteristics. According to the above, compared with S-eCAP and L-eCAP, the use of the directly measured R-eCAP is not likely to give a meaningful representation of the refractory properties of the AN which may obscure potential clinical implications.

5.4.2 Refractory characteristics of the AN in children and adults

The current study demonstrated a significantly shorter T_R and a significantly larger A_R in children than in adults, but there were no differences in τ_R between these groups. Our results were partially comparable with Carvalho et al. (2015), who found a significantly larger A_R in children than in adults. They did not find significant differences in T_R and τ_R between the two groups. Our results demonstrated that R-eCAP contains two different components with different refractory characteristics, and using S-eCAP and L-eCAP can lead to more accurate estimates of the refractory parameters. Thus, we further compared the refractory properties derived from the S-eCAP and L-eCAP between children and adults. Specifically, we only observed significant differences between the two groups for the S-RRF; namely, A_S was significantly larger in children. No significant differences between the two groups were observed for other parameters (T_S, T_L, A_L, τ_S, and τ_L). The result for A_S in our study was in line with the findings by Dong et al. (2020), who reported that a larger short-latency component of the compound discharge latency distribution, which is highly correlated to the eCAP amplitude, was observed in children. Gordon et al. (2002) also found higher eCAP amplitudes, i.e., 'A' values, in children compared with post-lingual adults. A possible explanation for the difference is that children have a larger

number of healthy ANFs involved in S-eCAP than adults.

In terms of speed of recovery, children did not demonstrate significant differences compared to adults (τ_S and τ_L) in our study. Our results did not support the finding by others that children tend to show a higher speed of recovery than adults (e.g., Xi et al., 2004). We believe that the inconsistent results observed in our study may have resulted from several factors, such as the different maturation of the ANFs and different duration of deafness between children and adults. Specifically, the AN in children is less mature than that in adults, such that children with CIs would undergo electrical impulses on the immature AN, and this might affect the maturation of the AN by the stimulation (e.g., Xu et al., 1997). In addition, hearing loss is usually age-related in adults, they tend to have suffered from deafness longer than children. As a consequence, adults have a greater risk of more extended nerve degeneration than children (e.g., Xi et al., 2004), and adults would expectedly have a lower speed of recovery. However, Botros and Psarros (2010) proposed that a larger neural ANF population, rather than a longer duration of deafness, would result in a lower speed of recovery. Thus, the existing literature is not in agreement on the presence of differences in the speed of recovery. The lack of any difference in our study may be caused by the mixture of the opposing influences of the maturation state, ANF population, and duration of deafness on the speed of recovery.

Shepherd et al. (2004) found that the absolute refractory period of individual rat auditory neurons increased with increasing duration of deafness. Our result of the T_S and T_L appear not to be in line with this expectation, i.e., adults do not show a longer absolute refractory period than children although adults usually suffered from longer periods of deafness. However, as stated above, we cannot rule out that the difference may be caused by the different populations and maturation of ANFs underlying S-eCAP and L-eCAP between the two groups. To further address if the refractory properties of ANFs of children differ from adults, maturation state, ANF population, and duration of deafness need to be taken into account in future studies.

5.4.3 Effects of auditory refractory properties on speech perception

In the present study, we observed that the τ_R did not show a significant relationship with speech perception. Previous literature reports equivocal results in terms of the importance of τ_R for speech recognition outcomes with a CI (e.g., He et al., 2017). We argue that the derived measures of the speed of recovery, S-RRF and L-RRF, are better estimates than the R-RRF measures, as we found a significant association between τ_S and speech perception. One possible explanation was that two components in the eCAP originated from different populations of ANFs in terms of degenerative state, maturation, and refractory characteristics. For instance, the S-eCAP may arise from a healthier group of fibers and the L-eCAP from a more degenerated group, representing different surviving and functional statuses (e.g., Ramekers et al., 2015; Konerding et al., 2020). Therefore, the two populations of ANFs can affect speech perception differently, namely, the speed of recovery derived from the S-eCAP contributes significantly more to speech performance than that from L-eCAP. Importantly, the speed of recovery obtained by the conventional R-RRF using the raw eCAP amplitude does not predict performance, while considering the S- and L-eCAP separately proved to yield a more useful indicator for the CI outcomes. Furthermore, the results that the T and A parameters of R-RRF, S-RRF, and L-RRF did not correlate to speech perception suggested that they appear not to be essential factors for speech performance. Therefore, we advise the use of the derived S-RRF and L-RRF components instead of R-RRF in future clinical practice to predict speech performance after implantation.

A limitation of this study is that realistic refractory parameters of 29 RRFs (13.9%) could not be derived due to fitting errors. Morsnowski et al. (2005) also reported that 9 of 71 (12%) stimulation sites resulted in fitting errors. We believe that the possible reasons behind the failure may be the recording technique, as parameter estimates are likely to be sensitive to the number of data points; the MPI axis values; and the ANF density (Shepherd et al., 2004; Cohen, 2009; Boulet et al., 2015; He et al., 2017). The stability and validity of the exponential decay fitting of RRF (Eq. (5.1)) are sensitive to the number of data points and the MPI axis values, especially within the relative refractory period. For instance, when eCAPs cannot be detected due to

background noise in the recording, the missing data likely result in a parameter discrepancy. It is possible that future studies, especially with additional MPIs within the relative refractory period, may refine the present estimates of the refractory characteristics of the whole nerve. In addition, uncertainty remains regarding the origins of the S-eCAP and L-eCAP (e.g., Strahl et al., 2016; Dong et al., 2020) and the physiological mechanism of the different refractory properties underlying the S-eCAP and L-eCAP. To further understand these issues, future studies with electrophysiological measures of the AN are warranted.

5.5 CONCLUSIONS

In the current study, we demonstrated that the short-latency and long-latency components of the eCAP have different auditory refractory properties. The refractory properties of the two eCAP components differed between children and adults. Importantly, the speed of recovery, as obtained by the classical RRF method using the raw eCAP, did not predict speech performance. However, evaluating the two components of the eCAP separately proved to be indicative of speech performance after implantation. The collective results suggest that consideration should be given to the two components of the eCAP separately when the AN refractory characteristics are evaluated for clinical purposes.

ACKNOWLEDGMENTS

The first author of the present study is financially supported by the China Scholarship Council. There are no conflicts of interest, financial or otherwise.

Yu Dong designed and performed experiments, analyzed data, and wrote the paper; Jeroen J. Briaire designed experiments, discussed the results and implications, and provided critical revision; H. Christiaan Stronks and Johan H. M. Frijns discussed the results and implications and provided critical revision.

REFERENCES

Abbas, P. J., & Brown, C. J. (1991). Electrically evoked auditory brainstem response: refractory properties and strength-duration functions. Hearing research, 51(1), 139-147.

Battmer, R. D., Lai, W. K., Dillier, N., Pesch, J., Killian, M. J., & Lenarz, T. (2005). Correlation of NRT recovery function parameters and speech perception results for different stimulation rates. In Abstracts of the Fourth International Symposium and Workshops on Objective Measures in Cochlear Implants (p. 21).

Biesheuvel, J. D., Briaire, J. J., & Frijns, J. H. (2018). The precision of eCAP thresholds derived from amplitude growth functions. Ear and hearing, 39(4), 701-711.

Bosman, A. J., & Smoorenburg, G. F. (1995). Intelligibility of Dutch CVC syllables and sentences for listeners with normal hearing and with three types of hearing impairment. Audiology, 34(5), 260-284.

Botros, A., & Psarros, C. (2010). Neural Response Telemetry Reconsidered: II. The Influence of Neural Population on the ECAP Recovery Function and Refractoriness. Ear & Hearing, 31(3), 380–391.

Boulet, J., White, M., & Bruce, I. C. (2016). Temporal Considerations for Stimulating Spiral Ganglion Neurons with Cochlear Implants. JARO - Journal of the Association for Research in Otolaryngology, 17(1), 1–17.

Brauer, M., Curtin, J. J. (2018). Linear mixed-effects models and the analysis of nonindependent data: A unified framework to analyze categorical and continuous independent variables that vary within-subjects and/or within-items. Psychol Methods, 23, 389-411.

Brown, C. J., Abbas, P. J., & Gantz, B. (1990). Electrically evoked whole-nerve action potentials: Data from human cochlear implant users. The Journal of the Acoustical Society of America, 88(3), 1385–1391.

Bruce, I. C., Irlicht, L. S., White, M. W., O'Leary, S. J., Dynes, S., Javel, E., & Clark, G. M. (1999). A stochastic model of the electrically stimulated AN: pulse-train response. IEEE Transactions on Biomedical Engineering, 46(6), 630-637.

Cohen, S. M., & Svirsky, M. A. (2019). Duration of unilateral auditory deprivation is associated with reduced speech perception after cochlear implantation: A single-sided deafness study. Cochlear Implants International, 20(2), 51–56.

Dong, Y., Briaire, J. J., Biesheuvel, J. D., Stronks, H. C., & Frijns, J. H. M. (2020). Unravelling the Temporal Properties of Human eCAPs through an Iterative Deconvolution Model. Hearing Research, 395, 108037.

Dong, Y., Stronks, H. C., Briaire, J. J., & Frijns, J. H. (2021). An iterative deconvolution model to extract the temporal firing properties of the auditory nerve fibers in human eCAPs. MethodsX, 8, 101240.

Dynes, S. B. C. (1996). Discharge characteristics of auditory nerve fibers for pulsatile electrical stimuli (Doctoral dissertation, Massachusetts Institute of Technology).

Fitzmaurice, G. M., Laird, N. M., & Ware, J. 2. (2004). Linear mixed effects models. Applied longitudinal analysis, 1, 187-236.

Fulmer, S. L., Runge, C. L., Jensen, J. W., & Friedland, D. R. (2011). Rate of neural recovery in implanted children with auditory neuropathy spectrum disorder. Otolaryngology-Head and Neck Surgery, 144(2), 274–279.

Gantz, B. J., Brown, C. J., & Abbas, P. J. (1994). Intraoperative measures of electrically evoked AN compound action potential. The American journal of otology, 15(2), 137-144.

Gray, P. R. (1967). Conditional probability analyses of the spike activity of single neurons. Biophysical Journal, 7(6), 759-777.

Gordon, K. A., Gilden, J. E., Ebinger, K. A., & Shapiro, W. H. (2002). Neural response telemetry in 12- to 24-month-old children. Annals of Otology, Rhinology & Laryngology, 111(5_suppl), 42-48.

He, S., Teagle, H. F. B., & Buchman, C. A. (2017). The electrically evoked compound action potential: From laboratory to clinic. Frontiers in Neuroscience, 11(JUN), 1–20.

Kiefer, J., Hohl, S., Stürzebecher, E., Pfennigdorff, T., & Gstöettner, W. (2001). Comparison of speech recognition with different speech coding strategies (SPEAK, CIS, and ACE) and their relationship to telemetric measures of compound action potentials in the nucleus CI 24M cochlear implant system. International Journal of Audiology, 40(1), 32–42.

Lai, W. K., & Dillier, N. (2000). A Simple Two-Component Model of the Electrically Evoked Compound Action Potential in the Human Cochlea. Audiology and Neurotology, 5(6), 333–345.

Lee, E. R., Friedland, D. R., & Runge, C. L. (2012). Recovery from forward masking in elderly cochlear implant users. Otology and Neurotology, 33(3), 355–363.

Matsuoka, A. J., Rubinstein, J. T., Abbas, P. J., & Miller, C. A. (2001). The effects of interpulse interval on stochastic properties of electrical stimulation: models and measurements. IEEE transactions on biomedical engineering, 48(4), 416-424.

Miller, C. A., Abbas, P. J., & Brown, C. J. (2000). An improved method of reducing stimulus artifact in the electrically evoked whole-nerve potential. In Ear and Hearing (Vol. 21, Issue 4, pp. 280–290).

Miller, C. A., Abbas, P. J., & Robinson, B. K. (2001). Response properties of the refractory AN fiber. JARO - Journal of the Association for Research in Otolaryngology, 2(3), 216–232.

Molenberghs, G., Bijnens, L., Shaw, D. (1997) Linear Mixed Models and Missing Data. In: Linear Mixed Models in Practice. Lecture Notes in Statistics, vol 126. Springer, New York, NY. https://doi.org/10.1007/978-1-4612-2294-1_5

Morsnowski, A., Charasse, B., Collet, L., Killian, M., & Müller-Deile, J. (2006). Measuring the refractoriness of the electrically stimulated AN. Audiology and Neurotology, 11(6), 389–402.

Ramekers, D., Versnel, H., Strahl, S. B., Klis, S. F. L., & Grolman, W. (2015). Recovery characteristics of the electrically stimulated AN in deafened guinea pigs: Relation to neuronal status. Hearing Research, 321, 12–24.

Shepherd, R.K. & Hardie, N.A. (2001). Deafness-induced changes in the auditory pathway: implications for cochlear implants. Audiol. Neurootol., 6, 305–318.

Shepherd, R. K., Roberts, L. A., & Paolini, A. G. (2004). Long-term sensorineural hearing loss induces functional changes in the rat auditory nerve. European Journal of Neuroscience, 20(11), 3131-3140.

Strahl, S. B., Ramekers, D., Nagelkerke, M. M., Schwarz, K. E., Spitzer, P., Klis, S. F., ... & Versnel, H. (2016). Assessing the firing properties of the electrically stimulated auditory nerve using a convolution model. In Physiology, Psychoacoustics and Cognition in Normal and Impaired Hearing (pp. 143-153). Springer, Cham.

Stypulkowski, P. H., & van den Honert, C. (1984a). Physiological properties of the electrically stimulated AN. I. Compound action potential recordings. Hearing Research, 14(3), 205–223.

van den Honert, C., & Stypulkowski, P. H. (1984b). Physiological properties of the electrically stimulated auditory nerve. II. Single fiber recordings. Hearing Research, 14(3), 225–243.

Versnel, H., Prijs, V. F., & Schoonhoven, R. (1992). Round-window recorded potential of single-fibre discharge (unit response) in normal and noise-damaged cochleas. Hearing Research, 59(2), 157–170. https://doi.org/10.1016/0378-5955(92)90112-Z

Turner, C., Mehr, M., Hughes, M., Brown, C., & Abbas, P. (2002). Within-subject predictors of speech recognition in cochlear implants: A null result. Acoustic Research Letters Online, 3, 95–100.

van de Heyning, P., Arauz, S. L., Atlas, M., Baumgartner, W. D., Caversaccio, M., Chester-Browne, R., et al. (2016). Electrically evoked compound action potentials are different depending on the site of cochlear stimulation. Cochlear Implants Int. 17, 251–262.

Van Eijl, R. H. M., Buitenhuis, P. J., Stegeman, I., Klis, S. F. L., & Grolman, W. (2017). Systematic review of compound action potentials as predictors for cochlear implant performance. Laryngoscope, 127(2), 476–487.

Wilson, B. S., Finley, C. C., Lawson, D. T., and Zerbi, M. (1994). Speech Processors for Auditory Prostheses. NIH Project N01-DC-2-2401. Seventh Quarterly Progress Report.

Xi, X., Ji, F., Han, D. Y., Huang, D. L., Hong, M. D., & Yang, W. Y. (2004). Refractory recovery function of electrical auditory on the survival auditory nerve in cochlear implant recipients. Zhonghua er bi yan hou ke za zhi, 39(2), 77-80.

Xu, J., Shepherd, R. K., Millard, R. E., & Clark, G. M. (1997). Chronic electrical stimulation of the auditory nerve at high stimulus rates: a physiological and histopathological study. Hearing research, 105(1-2), 1-29

Chapter 6

Detection of Translocation of Cochlear Implant Electrode Arrays by Intracochlear Impedance Measurements

Yu Dong, Jeroen J. Briaire, Michael Siebrecht, H. Christiaan Stronks and Johan H. M. Frijns

Ear and Hearing (2021; 42; 1397–1404)

Abstract

Objectives: Misplacement of the electrode array is associated with impaired speech perception in patients with cochlear implants (CIs). Translocation of the electrode array is the most common misplacement. When a CI is translocated, it crosses the basilar membrane from the scala tympani into the scala vestibuli. The position of the implant can be determined on a postoperative CT scan. However, such a scan is not obtained routinely after CI insertion in many hospitals, due to radiation exposure and processing time. Previous studies have shown that impedance measures might provide information on the placement of the electrode arrays. The electrode impedance was measured by dividing the plateau voltage at the end of the first phase of the pulse by the injected current. The access resistance was calculated using the so-called access voltage at the first sampled time point after the start of the pulse divided by the injected current. In our study, we obtained the electrode impedance and the access resistance to detect electrode translocations using electrical field imaging. We have investigated how reliably these two measurements can detect electrode translocation, and which method performed best.

Design: We calculated the electrode impedances and access resistances using electrical field imaging recordings from 100 HiFocus Mid-Scala CI (Advanced Bionics, Sylmar, CA) recipients. We estimated the normal values of these two measurements as the baselines of the implant placed in the cochlea without translocation. Next, we calculated the maximal electrode impedance deviation and the maximal access-resistance deviation from the respective baselines as predictors of translocation. We classified these two predictors as translocations or nontranslocations based on the bootstrap sampling method and receiver operating characteristics curves analysis. The accuracy could be calculated by comparing those predictive results to a gold standard, namely the clinical CT scans. To determine which measurement more accurately detected translocation, the difference between the accuracies of the two measurements was calculated.

Results: Using the bootstrap sampling method and receiver operating characteristics–based optimized threshold criteria, the 95% confidence intervals of the accuracies of translocation

detections ranged from 77.8% to 82.1% and from 89.5% to 91.2% for the electrode impedance and access resistance, respectively. The accuracies of the maximal access-resistance deviations were significantly larger than that of the maximal electrode impedance deviations. The location of the translocation as predicted by the access resistance was significantly correlated with the result derived from the CT scans. In contrast, no significant correlation was observed for the electrode impedance.

Conclusions: Both the electrode impedance and access resistance proved reliable metrics to detect translocations for HiFocus Mid-Scala electrode arrays. The access resistance had, however, significantly better accuracy and it also reliably detected the electrode-location of translocations. The electrode impedance did not correlate significantly with the location of translocation. Measuring the access resistance is, therefore, the recommended method to detect electrode-array translocations. These measures can provide prompt feedback for surgeons after insertion, improving their surgical skills, and ultimately reducing the number of translocations. In the future, such measurements may allow near-real-time monitoring of the electrode array during insertion, helping to avoid translocations.

Keywords: Cochlear implants, Sensorineural hearing loss, Deafness, Electrode translocation, Electrode impedance, Access resistance, Electrical field imaging

6.1 Introduction

A cochlear implant (CI) is an intracochlear device that can restore hearing through direct electrical stimulation of the auditory nerve. Severely-to-profoundly deaf people with sensorineural hearing loss can benefit from a CI (Hughes 2012). However, speech perception outcomes show large variability (Firszt et al. 2004; Holden et al. 2013). An important factor determining speech perception is the placement of the electrode array. Misplacement is typically associated with poorer speech performance (Aschendorff et al. 2007; Finley & Skinner 2009; Gifford et al. 2013; Holden et al. 2013; Wanna et al. 2014; Carlson et al. 2015; O'Connell et al. 2016). The shift of an electrode array from the scala tympani to the scala vestibuli through the

basilar membrane is called a translocation (Finley & Skinner 2009; Holden et al. 2013; O'Connell et al. 2016; Dhanasingh & Jolly 2017). Translocation is the most common type of electrode misplacement in patients with CIs, although the incidence rates reported in the literature vary widely, from as little as 4% to as high as 54% in a couple of research groups across different electrode array types (Holden et al. 2013; Wanna et al. 2014; O'Connell et al. 2016; Dhanasingh & Jolly 2017). It is possible to detect translocations on a CT scan (Wanna et al. 2014). However, radiology is not routinely applied because it requires additional work, and leads to radiation exposure of patients. As a consequence, insertion trauma often goes unnoticed. In addition, radiological measures cannot be easily applied to monitor the insertion during surgery. For these reasons, an alternative tool is needed to detect translocations.

One promising alternative is the use of impedance measurements. Impedance is a measure of the resistance of current flow through a medium. Clinically, electrode impedance (clinical impedance) recordings are supported by the state-of-the-art cochlear implant systems from all the current implant providers, e.g., Advanced Bionics, Med-EL, Cochlear Ltd and Oticon Medical (Hughes 2012; Dang et al. 2015). Earlier studies found that electrode impedance can be indicative of the endocochlear environment adjacent to the electrode contacts (Agnew et al. 1983; Suesserman & Spelman 1993; Saunders et al. 2002; Tykocinski et al. 2005; Giardina et al. 2017). However, they have not yet been deployed for the detection of electrode translocations. Electrode impedances can be indicative of the endocochlear environment adjacent to the electrode contacts (Agnew et al. 1983; Saunders et al. 2002; Tykocinski et al. 2005; Giardina et al. 2017). Translocation presents the electrode contacts with new medium and tissue characteristics. Due to the differences in resistivity of different tissues and media (Frijns et al. 1995), the impedance in the vicinity of the translocation might also change.

Two different impedance measurements can potentially detect electrode translocation, i.e., the electrode impedance and the access resistance. These two metrics can be obtained using electrical field imaging (EFI) method (Vanpoucke et al. 2004a; Hughes 2012). EFI involves the recording of a matrix of voltages across the measuring electrodes. EFIs are usually recorded by

stimulating one electrode and recording the voltage back with all electrodes. These are commonly converted to impedances to reflect a conductivity map of the intracochlear tissues by dividing the voltages by the current injected by the stimulating electrode (Vanpoucke et al. 2004a; Mens 2007). When translocation occurs, this conductivity map may change accordingly. Within this EFI impedance matrix, the off-diagonal impedances reflect the resistive component of the tissue and fluid between the stimulating and return electrodes (Clark et al. 2003; Vanpoucke et al. 2004b; Hughes 2012). The decay of the off-diagonal impedance as a function of distance has been modeled with various decay functions because exponential decays are not necessarily constant from the base toward the apex in the cochlea (e.g., Vanpoucke et al. 2004a, b; 2012).

The diagonal impedances within the EFI matrix refer to the electrode impedances where the stimulating electrode was also used as the recording contact. In earlier studies, these diagonals were omitted since the higher potential densities in the vicinity of the electrodes cannot be appropriately described by an exponential decay (e.g., Jolly et al. 1996; Briaire et al. 2000; Mens et al. 2003; Vanpoucke et al. 2004a). Nevertheless, these electrode impedances may be useful for detecting electrode translocation due to the access resistance component which can presumably increase when electrode translocation occurs. (Clark et al. 2003; Vanpoucke et al. 2004b; Hughes 2012). Specifically, the access resistance depends on the size and type of metal in the electrode contact and lead wire, and the resistivity of the surrounding fluid and tissue in cochlear implants (e.g., perilymph, fibrous tissue, bone; Clark et al. 2003; Tykocinski et al. 2005). The access resistance can be extracted by simulating the electrode impedance as an electrical circuit model as shown in Figure 6.1. This model combines a serial resistor (representing the access resistance, $\mathrm{R_a}$) with the polarization impedance ($\mathrm{Z_P}$) of the electrode-electrolyte interface, which is modeled as a parallel circuit with polarization resistance ($\mathrm{R_f}$) and capacitance ($\mathrm{C_w}$). In this model, the $\mathrm{R_a}$ arises from the resistivity of the bulk-surrounding of the intracochlear electrode array; the polarization impedance (Z_p) is determined by the electrochemical electrode-electrolyte interface between the charged metal electrode surface and the surrounding fluid or tissue. C_w results from the capacitive effect of the interface between the stimulating electrode

and surrounding tissue medium, whereas R_f is the charge transfer resistance (Clark & Richter 2004;; Vanpoucke et al. 2004b; Tykocinski et al. 2005; Hughes 2012). The access resistance component in Figure 6.1 would change upon translocation, which can place the electrode contact in a different tissue environment. As a consequence, the access resistance near the translocation site will deviate from the normal value, and hence may be an indicator of translocation. Given that the electrode impedance contains the access resistance component, we hypothesized the electrode impedance may also be feasible for detecting electrode translocations. However, how a translocation affects the polarization impedance (Z_P) component of the electrode impedance is still uncertain. This polarization component may contaminate the effect of the electrode impedances in reflecting translocation. Thus, we further hypothesized that the access resistance (R_a) could be more capable of detecting translocations than the electrode impedance. This study aimed to assess whether the electrode impedance (the combination of the R_a and Z_P) and the R_a can be used to detect electrode translocation, and which metric is more viable.

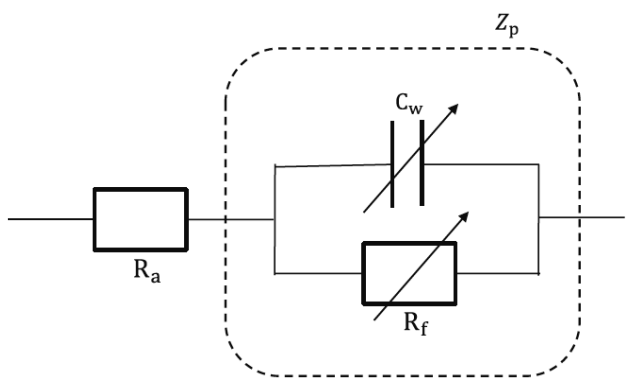

Fig. 6.1 Electrical circuit diagram for contact impedance (Vanpoucke et al. 2004b; Hughes 2012). R_a represents the access resistance (electrode contact, electrode lead wire, fluid/tissue medium). C_w represents the capacitance of the electrode-tissue interface between the electrode surface and the surrounding fluid or tissue. R_f represents potential faradic resistance that transfers charges via chemical reactions. Z_p represents the polarization impedance at the electrode-electrolyte interface by modelling the C_w and R_f in parallel.

6.2 MATERIAL AND METHODS

6.2.1 Subjects

The electrode impedances and the access resistances used in the present retrospective study were obtained from 106 patients who consecutively received a HiRes90K Mid-Scala electrode array (Advanced Bionics, Sylmar, CA) between June 2012 and September 2018. This electrode array consists of 16 platinum contacts with 0.9 mm spacing (1 to 16 in apical-to-basal order). Preoperative and postoperative multi-slice computed tomography scans (Aquilion; Toshiba Medical Systems, Otowara, Japan) were performed according to the standard protocol for cochlear implant patients at the Leiden University Medical Centre (van der Jagt et al. 2017a). According to the CT image, we excluded patients with pre-operative characteristics that may affect the electrode array trajectory, such as a single case of cochlear ossifications, and two patients who underwent a re-implantation. Patients with high noisy impedance measurements (i.e., the electrode impedance was larger than 25 kOhm) (n = 3) were excluded. Therefore, a total of 100 patients were included in the analysis (Table 6.1).

TABLE 6.1. Patient demographics

Number of Patients	100
Gender (n)	
Male	41
Female	56
Mean age ± SD (years)	41 ±26
Etiology (n)	
Meningitis	4
Meniere's disease	1
Otosclerosis	0
Congenital/Hereditary	39
Other/Unknown	56

6.2.2 Data recording

The EFI recordings were performed immediately after the insertion of the electrode array just after the round window closure using the electrical field imaging and modeling (EFIM) tool from Advanced Bionics (for details, see Vanpoucke et al. 2004b). In brief, all 16 contacts were sequentially recorded from apex to base using monopolar recording mode. The reference electrode was the implant casing in the mastoid bone. The CI processor has a built-in amplifier with an analog-to-digital converter that operates at a sample rate of 56 kHz. Each electrode contact is driven by a separate current source, and a blocking capacitor is present in the internal device electronics to prevent DC stimulation. Current passed through the blocking capacitor and the lead wire to the contact. At a recording contact, the difference of potentials between this contact and the reference electrode was recorded. In EFI, each time the intracochlear potential was measured at all contacts with biphasic pulses with an amplitude of 40 µA lasting 66.45 µs per phase. The diagonal voltages in EFI were used to calculate the electrode impedances and the access resistances.

To calculate the electrode impedances expressed in Ohm units, the potentials recorded at the end of the first phase of the pulse were divided by the injected current. Figure 6.2A shows an example of an EFI for a patient (S73) with translocation and an example of an EFI for a patient (S10) without translocation is given in Figure 6.2B. Only the electrode impedances marked by circles were used for analysis.

The approach used to extract access resistance was described by Tykocinski et al. (2005) and Giardina et al. (2017). In brief, the CI electrode-electrolyte interface was modeled as shown in Figure 6.1. The response waveform to a stimulus pulse includes two sources of voltage increase consistent with this model: an immediate jump in voltage from the frequency-independent resistive elements between the contact and the ground (i.e., access resistance), and a slowly increasing limb voltage representing a charge accumulation at the electrode-electrolyte interface (polarization voltage). The access resistances were calculated using the access voltage at the first sampled time point divided by the injected current pulse amplitude.

6.2.3 Translocation detection from CT imaging

We used the results from CT images as the gold standard. The pre- and postoperative CT images were used to visually assess them side by side to confirm if electrode translocation occurred, as described in detail by Van der Jagt et al. (2017b). According to their CT image outcome, we identified 25 of the 100 patients included in the present study in whom the array was translocated and the other 75 patients in whom it was contained within the scala tympani.

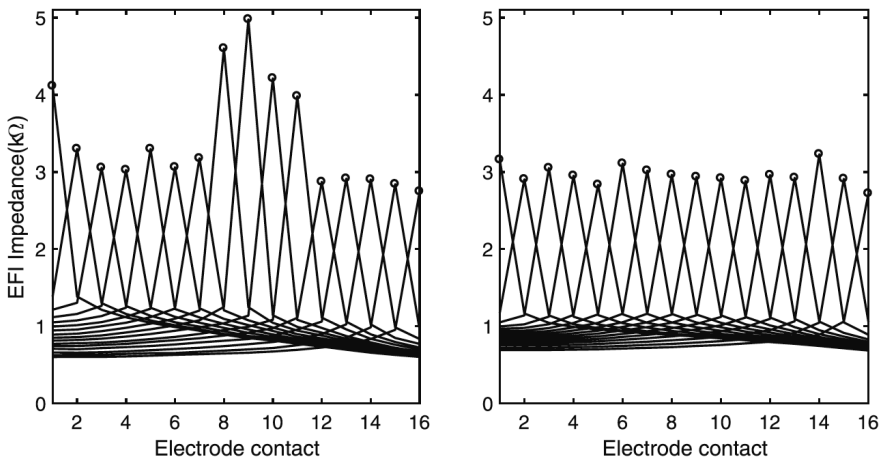

Fig. 6.2 Two typical EFI maps recorded with biphasic pulses 40-µA, lasting 66.45 µs per phase. Contact 1 (16) is the most apical (basal) one. Each of the 16 spread curves shows the intracochlear impedance profile generated when a single contact is stimulated. A, EFI map with a translocation (S73). B, EFI map without a translocation (S10). The electrode impedances (circles) were used for further analysis.

6.2.4 Analysis

6.2.4.1 Translocation detection from electrode impedances and access resistances

We performed three steps to generate the predictors of translocation based on the electrode impedances. We hypothesized that translocation changes the electrode impedances of nearby contacts. To calculate this deviation, we fitted the baselines of the 16 electrode impedances with a straight line to obtain a measure of normal baseline impedances (in Fig. 6.3, green solid lines).

To this end, we used robust linear regression with the bisquare weighting function (robustfit, MATLAB, Mathworks 2016a, Natick, MA) to minimize the influence of any outliers on the baseline fit. The outliers are expected to include those electrode impedances near a translocation. With these baseline values, we obtained the deviations of the 16 electrode impedances by calculating their distances from the electrode impedance to their baseline. We used the maximal EFI electrode impedance deviation of these 16 deviations to identify the most likely candidates for electrode translocation (in Fig. 6.3C, blue solid lines).

In the same manner, we used robust fitting to obtain the baseline of the 16 access resistances. The distances from the access resistances to this baseline were calculated, and the maximal access-resistance deviation of these 16 values (in Fig. 6.3, blue solid lines) was used to identify the most likely candidate for electrode translocation.

6.2.4.2 Estimating the thresholds and accuracies of the electrode impedance deviations and the access resistance deviations for predicting a translocation

To estimate the thresholds and the accuracies of translocation detections, we used bootstrapping by randomly selecting subgroups of 80% of the patients that were used to predict the translocations in the remaining 20% of patients. To improve reliability, 500 random selections were performed using the bootstrapping method. This sampling method has been described by Harrell et al. (1996). Receiver operating characteristics (ROC) curves were generated to graphically display the performance (Schisterman et al. 2005; Brown & Davis 2006). The weight of a false positive and false negative result was identical. The ROC curves were used to estimate the thresholds for the maximal electrode impedance deviations and the maximal access-resistance deviations using the CT image as the gold standard. The thresholds were used as criteria for translocation detection of the remaining 20% of patients. In the latter group, translocations were determined (true positives) as well as non-translocations (true negatives). Similarly, false positives (type Ⅰ error) and false negatives (type Ⅱ error) were determined. The accuracies refer to the percentage of the true positives and the true negatives for each measure

relative to the total number of samples (i.e., the remaining 20% of patients) of the electrode impedance and the access resistance can be calculated for the remaining 20%.

The confidence intervals of the accuracies and thresholds of the two measures from the 500 selections were calculated. To determine which measurement was better at detecting translocation, we compared the accuracies of the two measurements using the Wilcoxon rank-sum test.

6.2.4.3 Predicting the location of translocations using the electrode impedance and the access resistance

We further investigated if the two measurements were able to predict the location of translocations. To this end, we defined the electrode contact where the maximal electrode impedance deviation and the maximal access-resistance deviation appeared as the location of translocation. We correlated the location of translocation (true positive cases) by the two measurements with the contact where translocation occurred according to CT images using Pearson's correlation coefficient.

6.3 RESULTS

Figure 6.3 illustrates the principle of translocation detection with EFI. Figures 6.3A and B show two three-dimensional (3D) reconstructions of 2 patients' cochleas with and without a translocation obtained using a custom-made MATLAB software routine (Siebrecht et al. 2019). In the translocation case, the electrode array pierces the basilar membrane from the scala tympani to the scala vestibuli near electrode 8 (Fig. 6.3A). The outcomes of the maximal electrode impedances and the maximal access resistances of the cochlea with a translocation are shown in Figures 6.3C and E. In these two panels, the maximal electrode impedance deviation and the maximal access-resistance deviation exceed the optimal threshold near electrode 8, and hence accurately reflect the translocation. Similarly, Figure 6.3B shows the 3D reconstruction of the

cochlea without translocation, in which the whole electrode array is contained within the scala tympani. Figures 6.3D and F show the corresponding electrode impedances and access

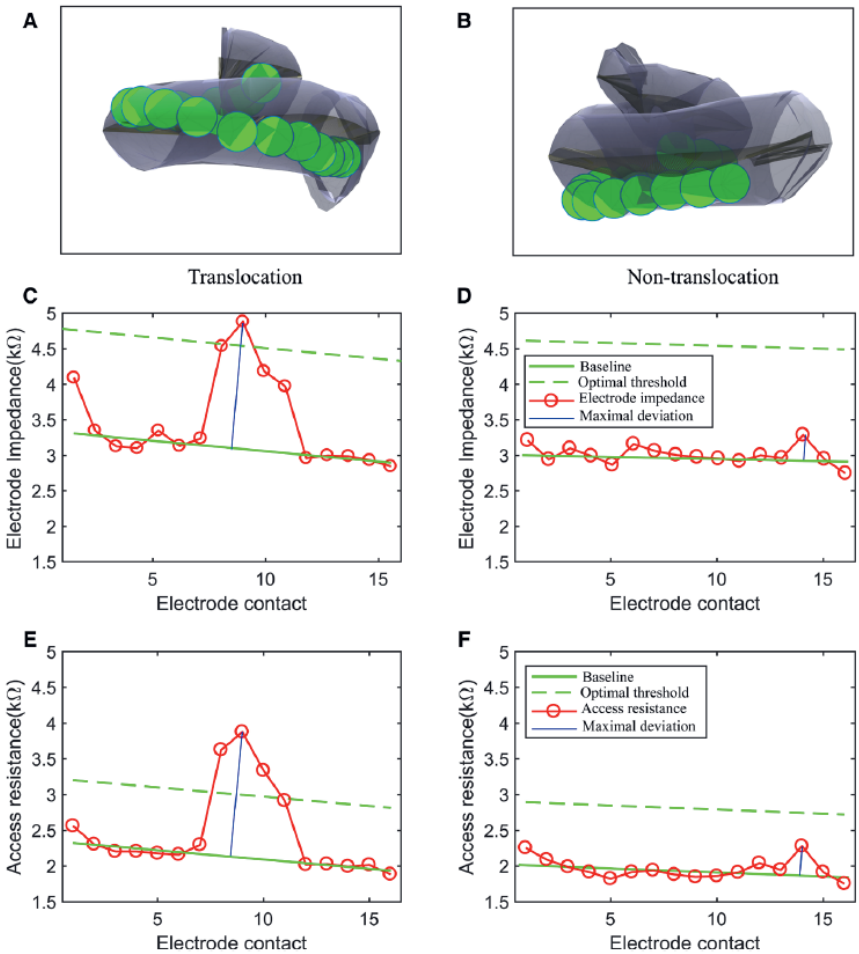

Fig. 6.3 Examples of translocation (A, C, E; S73) and non-translocation (B, D, F; S10). A and B, 3D reconstructions based on CI scan image of a cochlea with (A) and without a translocation (B), respectively. C and D, the electrode impedances corresponding to the two examples. E and F, the respective access resistances of the two examples. The dashed green lines in C, D, E, and F indicate the optimal thresholds derived from the ROC analysis for predicting the occurrence of a translocation.

resistances, respectively. The maximal electrode impedance deviation and the maximal access-resistance deviation stay below the optimal thresholds, indicating an absence of translocation.

The optimal threshold in each of these two examples refers to the medians of thresholds for predicting translocation obtained from 500 random elections (described below). In these two examples, the detection of translocation is consistent with the outcomes based on the CT-scan images.

We investigated the thresholds and the accuracies of translocation detection with the electrode impedance and access resistance from 500 random selections. The median value of the electrode impedance was 1.26 kOhm (CI95%: 1.21–1.36 kOhm) and the median accuracy was 78.7% (CI95%: 77.8%–82.1%). The median access resistance was 0.85 kOhm (CI95%: 0.84–0.86 kOhm) and the median accuracy was 90% (CI95%: 89.5%–91.2%). The accuracy of the access resistance is significantly larger than that of the electrode impedance using the Wilcoxon rank-sum test ($p < 0.0001$).

TABLE 6.2. Detection of translocations with the electrode impedance and the access resistance using median

	True positive	True negative	False positive Type Ⅰ error	False negative Type Ⅱ error	Accuracy
Electrode impedance	21	62	13	4	83%
Access resistance	25	66	9	0	91%

The CT image outcomes were used as the gold standard: 25 patients with a translocation, and 75 patients without a translocation; Total = 100; Accuracy = (true positive + true negative)/Total.

The medians of thresholds for the maximal electrode impedance deviations and the maximal access-resistance deviations were used as the optimal thresholds to detect translocations of all the patients. Accordingly, 21 true positives and 62 true negatives were found using the maximal electrode impedance deviations as shown in Table 6.2. The maximal access-resistance deviations resulted in 25 true positives and 66 true negatives. The accuracies of the two measurements were 83% and 91%, respectively.

We further investigated if the two measurements were capable of detecting the location of the

translocation, using only the true-positive cases. For the electrode impedance measurement, the median of translocation contacts of the 21 true positives (with median deviation) was 10 ± 2.6 and ranged from electrode contact 1 to 13. We found that the translocation locations did not significantly correlate with the translocation contacts according to CT imaging using Pearson's correlation coefficient (r = 0.21, p = 0.31) (Fig. 6.4A). For the access resistance measurement, the median of translocation contacts of the 25 true positives (with median deviation) was 9 ± 1.2 and ranged from contact 6 to 15 which was significantly correlated with the results based on CT imaging (r = 0.79, p < 0.001) (Fig. 6.4B).

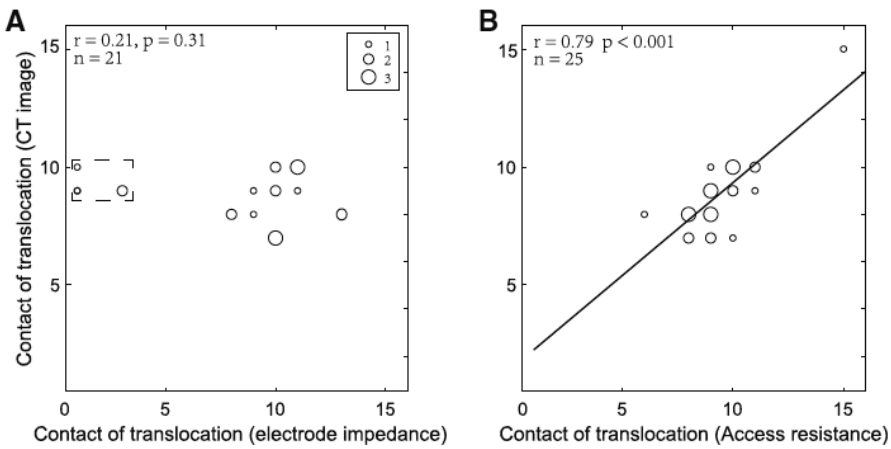

Fig. 6.4 Scatterplots showing the correlation between the location of translocation from CT image outcomes (y-axis) and the location of translocation from electrode impedance measure (A, y-axis) and the access resistance (B, y-axis). The dashed rectangle indicates the data points that the electrode impedance measure failed to detect the location of translocation.

6.4 DISCUSSION

Electrode-array translocations are detected commonly by analyzing postoperative (cone beam) CT images. Postoperative CT scans are not routinely made in many hospitals. In those hospitals where they are routinely performed after implantation surgery, it is often only after several days following the CI insertion. Hence, often there is no immediate feedback available to the surgeon regarding whether the insertion procedure resulted in translocation of the electrode array. Such

feedback is important, given that the reported incidence rates of translocation in several groups worldwide can be as high as 54% (e.g., O'Connell et al., 2016; Dhanasingh et al. 2017). In the present study, we found that the electrode impedance and the access resistance can both detect translocations, but the access resistance achieved significantly better accuracy. More importantly, only the access resistance was capable of predicting the location of the translocation (Fig. 6.4). These findings are consistent with our hypothesis that access resistance is a more viable predictor of translocation detection. Therefore, we recommend the use of the access resistance as an outcome measure for the detection of translocation, rather than the electrode impedance.

The current study shows that measuring access resistance is a viable, non-invasive method for detecting translocation of a HiFocus Mid-Scala electrode array without the need for a CT scan. Although the access resistance is not a commonly used metric, it can easily be determined in minutes based on EFI recordings. When translocations are detected, the cochlear damage has already been done; at that point in time retracting the electrode array could easily cause additional trauma to patients and is not advised. However, detecting translocation in patients immediately after insertion can potentially benefit surgeons by providing direct feedback. This can help improve their skills for future CI insertions and reduce insertion trauma (Trehan et al. 2015).

Although it is not completely clear how translocation of electrode array occurs, it is assumed that this is affected by the surgical technique, cochlear morphology, and the physical qualities of the array (Wanna et al. 2014; Trehan et al. 2015). In particular, the variability in the morphology of scala tympani, including its height, width, and cross-sectional area, could potentially play an important role in the occurrence of translocation (e.g., Aschendorff et al. 2005; Verbist et al. 2009; Avci et al. 2014). In these studies, the scalae tympani were classified into three different categories according to the variability in the vertical trajectory. The sloping category follows an upward trajectory from the round window without significant downward tendencies. The intermediate category shows a local rise in the vertical direction at the beginning, followed by a gradual decrease from the round window. The rollercoaster category follows a downward trajectory from the round window, changing to upward course between 75° to 120°, hence

generating a dip in the vertical trajectory (e.g., Avci et al. 2014). This rollercoaster category of scala tympani could force the electrode array initially into the downward direction and then into the upward direction. This may lead to trauma to the basilar membrane and translocation into the scala vestibuli at 180° location (e.g., Aschendorff et al. 2005; Verbist et al. 2009; Avci et al. 2014; van der Jagt et al. 2017). The location of translocations in the present study was 170° ± 19° according to the CT image, which was highly consistent with the rollercoaster category.

In this study, we found that the access resistance is a more accurate measure for detecting translocation than the electrode impedance. There are two possible explanations for these differences between the two measures. Tykocinski et al. (2005) proposed a contact impedance model to calculate the different components in CI electrode impedance, as shown in Figure 6.1. According to this model, when a translocation occurs, the most important change will be a change in the medium in the vicinity of the translocation site. This change mainly alters the access resistance, because its value depends on the surrounding medium (Clark et al. 2003; Tykocinski et al. 2005). How a translocation affects other capacitive and faradic resistance components of the electrode impedance is unclear. Hence, these components in the contact impedance model might obscure the effect of the electrode impedances in reflecting translocation, as illustrated by the three circles marked by a dashed rectangle in Fig. 6.4A. This speculation is supported by our observation that the access resistance measure yielded more true positives and fewer false negatives than the electrode impedance, meaning that the access resistance measure can reliably predict the location of translocation but the electrode impedance fails to do so (Fig. 6.4).

It is noteworthy that an increase in the access resistances or the electrode impedances does not necessarily indicate an electrode translocation (i.e., a false positive), because other possible causes could lead to an increase in impedance. For instance, electrode fold-over (Vanpoucke et al. 2012), or tissue, blood, air, or an unknown impurity sticking to the electrode contact during CI insertion might result in a noticeable upward deviation in impedance (Hughes 2012). This could explain the false positives in both the electrode impedance and the access resistance

method in this study. However, we cannot exclude other factors that may have caused the occurrence of false positives. We examined the CT images when our methods yielded false positives or false negatives. Unfortunately, the CT images did not yield any visual clues about the underlying reasons for the occurrence of the observed false negatives and false positives. The limited resolution of the CT images may have been partly responsible for this. Our findings also suggested that the translocation may be detected post-operatively. Note that, as time goes by after the implantation, other factors may result in an increase in impedance, such as ossifications and fibrosis (e.g., Xu et al. 1997; Tykocinski et al. 2001; Hughes 2012). This may lead to false positives. Therefore, the accuracy of the post-operative detection of electrode translocations may decline. Of note, all the patients in the current study received a HiFocus Mid-Scala electrode array where no tip-foldover occurred. Hence, the generalizability to other implant types requires further study.

Previous studies found that electrically evoked compound action potential threshold ratio between the apical and the basal portions could be used to detect a translocation (e.g., Mittmann et al. 2015, 2017). However, the NRT threshold method only yields information whether a translocation has occurred or not, and not about the exact location of the translocation along the electrode array. In contrast, we have found that the access-resistance measurement is a viable method to identify electrode translocation and where it has occurred along the electrode array. The electrically evoked compound action potential threshold ratio method depends on a detectable electrically evoked compound action potential threshold. Since electrically evoked compound action potential thresholds cannot always be determined, e.g., because of progressive degeneration of nerve fibers, the access resistance measurement may be a more feasible tool for detecting translocation in CI recipients.

Preventing intracochlear misplacement during CI insertion is thought to be important for better speech understanding (Usami et al. 2014; Dhanasingh et al. 2017). The influence of electrode translocation on speech perception in CI recipients will be examined in our center. Further, although the present method is not suitable for avoiding translocations, our findings suggest that

this method could theoretically be adapted to deliver real-time impedance measurements during insertion. Such a real-time monitoring system could provide the feedback necessary to assess the intra-cochlear placement of the electrode arrays and guide the surgeon in avoiding translocation of the array and also, perhaps, tip fold-overs. For instance, when the impedance starts changing, potentially indicating that misplacement is about to occur, the surgeon could take proper measures to avoid the misplacement, e.g., adjusting the angle and/or the speed of the insertion. In our center, EFI measurements are routinely performed, but only after CI insertion has been completed. However, we will investigate these possible uses of impedance measurements in the future.

6.5 CONCLUSIONS

We found that the electrode impedance and the access resistance can be used to detect electrode translocation immediately after intracochlear insertion without a CT scan. Using the access resistance proved to be a superior metric in terms of accuracy. Therefore, we recommend that access resistance measurements be used to monitor for translocations postoperatively. Our method can potentially be applied intra-operatively and could be extended into a useful tool to prevent or reduce the rate of translocations.

ACKNOWLEDGMENTS

The first author of the current study is financially supported by the China Scholarship Council. There are no conflicts of interest, financial, or otherwise.

Yu Dong designed and performed experiments, analyzed data and wrote the paper; Jeroen J. Briaire designed experiments and provided critical revision; Michael Siebrecht performed partially data analysis, discussed the results and implications and provided critical revision; H. Christiaan Stronks discussed the results and implications and provided critical revision; Johan H. M. Frijns discussed the results and implications and provided critical revision.

REFERENCES

Agnew, W. F., Yuen, T. G., McCreery, D. B. (1983). Morphologic changes after prolonged electrical stimulation of the cat's cortex at defined charge densities. Exp Neurol, 79, 397–411.

Aschendorff, A., Kromeier, J., Klenzner, T., & Laszig, R. (2007). Quality Control After Insertion of the Nucleus Contour and Contour Advance Electrode in Adults. Ear and Hearing, 28(Supplement), 75S-79S.

Avci, E., Nauwelaers, T., Lenarz, T., Hamacher, V., & Kral, A. (2014). Variations in microanatomy of the human cochlea. Journal of Comparative Neurology, 522(14), 3245–3261.

Briaire, J. J., & Frijns, J. H. M. (2000). Field patterns in a 3D tapered spiral model of the electrically stimulated cochlea. Hearing Research, 148(1–2), 18–30.

Brown, C. D., & Davis, H. T. (2006). Receiver operating characteristics curves and related decision measures : A tutorial, 80, 24–38.

Carlson, M. L., Driscoll, C. L. W., Gifford, R. H., Service, G. J., Tombers, N. M., Hughes-Borst, B. J., Neff, B. A., & Beatty, C. W. (2015). Implications of Minimizing Trauma During Conventional Cochlear Implantation. Journal of Investigative Dermatology, 135(2), 612–615.

Clark, G., & Richter, C. P. (2004). Cochlear Implants: Fundamentals and Applications. Physics Today, 57(11), 66-67.

Dang, K., Clerc, M., Vandersteen, C., Guevara, N., & Gnansia, D. (2015). In situ validation of a parametric model of electrical field distribution in an implanted cochlea. International IEEE/EMBS Conference on Neural Engineering, NER, 2015-July, 667–670.

Dhanasingh, A., & Jolly, C. (2017). An overview of cochlear implant electrode array designs. Hearing Research, 356, 93–103.

Finley, C. C., & Skinner, M. W. (2009). Role of electrode placement as a contributor to variability in cochlear implant outcomes, 29(7), 920–928.

Firszt, J. B., Holden, L. K., Skinner, M. W., Tobey, E. A., Peterson, A., Gaggl, W., Runge-Samuelson, C. L., & Wackym, P. A. (2004). Recognition of Speech Presented at Soft to Loud Levels by Adult Cochlear Implant Recipients of Three Cochlear Implant Systems. Ear and Hearing, 25(4), 375–387.

Frijns, J. H. M., de Snoo, S. L., & Schoonhoven, R. (1995). Potential distributions and neural excitation patterns in a rotationally symmetric model of the electrically stimulated cochlea. Hearing Research, 87(1–2), 170–186.

Giardina, C. K., Krause, E. S., Koka, K., & Fitzpatrick, D. C. (2017). Impedance Measures during in vitro

Cochlear Implantation predict Array Positioning. IEEE Transactions on Biomedical Engineering, 65(2), 327–335.

Gifford, R. H., Dorman, M. F., Skarzynski, H., Lorens, A., Polak, M., Driscoll, C. L. W., Roland, P., & Buchman, C. A. (2014). Cochlear implantation with hearing preservation yields significant benefit for speech recognition in complex listening environments. 34(4), 413–425.

Harrell, Jr, F. E., Lee, K. L., Mark, D. B. (1996). Multivariable prognostic models: Issues in developing models, evaluating assumptions and adequacy, and measuring and reducing errors. Stat Med, 15, 361–387.

Holden, L. K., Finley, C. C., Firszt, J. B., Holden, T. A., Brenner, C., Potts, L. G., Gotter, B. D., Vanderhoof, S. S., Mispagel, K., Heydebrand, G., & Skinner, M. W. (2013). Factors Affecting Open-Set Word Recognition in Adults With Cochlear Implants. Ear and Hearing, 34(3), 342–360.

Jolly, C. N., Spelman, F. A., Clopton, B. M. (1996). Quadrupolar stimulation for cochlear prostheses: Modeling and experimental data. IEEE Trans Biomed Eng, 43, 857–865.

Mens, L. H. M. (2007). Advances in Cochlear Implant Telemetry: Evoked Neural Responses, Electrical Field Imaging, and Technical Integrity. Trends in Amplification, 11(3), 143–159.

Mittmann, P., Ernst, A., & Todt, I. (2015). Intraoperative Electrophysiologic Variations Caused by the Scalar Position of Cochlear Implant Electrodes. Otology and Neurotology, 36(6), 1010–1014.

Mittmann, P., Todt, I., Ernst, A., Rademacher, G., Mutze, S., Göricke, S., Schlamann, M., Lang, S., Arweiler-Harbeck, D., & Christov, F. (2017). Radiological and NRT-Ratio-Based Estimation of Slim Straight Cochlear Implant Electrode Positions: A Multicenter Study. Annals of Otology, Rhinology and Laryngology, 126(1), 73–78.

Siebrecht, M., Briaire, J. J., & Frijns, J. H. M. Automated Inter-scalar Shift Detection for the HiFocus Mid- Scala from CT scans. In: CIAP 2019.

Hughes, M. L. (2012). Objective Measures in Cochlear Implants. Abingdon, SD: PLURAL PUBLISHING.

O'Connell, B. P., Cakir, A., Hunter, J. B., Francis, D. O., Noble, J. H., Labadie, R. F., Zuniga, G., Dawant, B. M., Rivas, A., & Wanna, G. B. (2016). Electrode Location and Angular Insertion Depth Are Predictors of Audiologic Outcomes in Cochlear Implantation. Otology & Neurotology, 37(8), 1016–1023.

Saunders, E., Cohen, L., Aschendorff, A., Shapiro, W., Knight, M., Stecker, M., Richter, B., Waltzman, S., Tykocinski, M., Roland, T., Laszig, R., & Cowan, R. (2002). Threshold, Comfortable Level and Impedance Changes as a Function of Electrode-Modiolar Distance. Ear and Hearing, 23(1 SUPPL.), 28–40.

Schisterman, E. F., Perkins, N. J., Liu, A., & Bondell, H. (2005). Optimal Cut-point and Its Corresponding Youden Index to Discriminate Individuals Using Pooled Blood Samples, 16(1), 73–81.

Suesserman, M. F., & Spelman, F. A. (1993). Lumped-Parameter Model for In Vivo Cochlear Stimulation. IEEE Transactions on Biomedical Engineering, 40(3), 237–245.

Trehan, A., Barnett-vanes, A., Carty, M. J., & Mcculloch, P. (2015). The impact of feedback of intraoperative technical performance in surgery : a systematic review, 1–5.

Tykocinski, M., Duan, Y., Tabor, B., & Cowan, R. S. (2001). Chronic electrical stimulation of the auditory nerve using high surface area (HiQ) platinum electrodes, 159.

Tykocinski, M., Cohen, L. T., & Cowan, R. S. (2005). Measurement and analysis of access resistance and polarization impedance in cochlear implant recipients. Otology and Neurotology, 26(5), 948–956.

Usami, S. I., Moteki, H., Tsukada, K., Miyagawa, M., Nishio, S. Y., Takumi, Y., Iwasaki, S., Kumakawa, K., Naito, Y., Takahashi, H., Kanda, Y., & Tono, T. (2014). Hearing preservation and clinical outcome of 32 consecutive electric acoustic stimulation (EAS) surgeries. Acta Oto-Laryngologica, 134(7), 717–727.

Van Der Jagt, M. A., Briaire, J. J., Verbist, B. M., & Frijns, J. H. M. (2017a). Comparison of the HiFocus Mid-Scala and HiFocus 1J electrode array: Angular insertion depths and speech perception outcomes. Audiology and Neurotology, 21(5), 316–325.

Jagt, A. M. A. V. Der, Kalkman, R. K., Briaire, J. J., Verbist, B. M., & Frijns, J. H. M. (2017b). Variations in cochlear duct shape revealed on clinical CT images with an automatic tracing method. Scientific Reports, 7(1), 1–9.

Vanpoucke, F., Zarowski, A., Casselman, J., Frijns, J., & Peeters, S. (2004a). The facial nerve canal: an important cochlear conduction path revealed by Clarion electrical field imaging. Otology & Neurotology, 25(3), 282-289.

Vanpoucke, F. J., Zarowski, A. J., & Peeters, S. A. (2004b). Identification of the impedance model of an implanted cochlear prosthesis from intracochlear potential measurements. IEEE Transactions on Biomedical Engineering, 51(12), 2174–2183.

Vanpoucke, F. J., Boermans, P. B. P. B., & Frijns, J. H. (2012). Assessing the placement of a cochlear electrode array by multidimensional scaling. IEEE Transactions on Biomedical Engineering, 59(2), 307–310.

Verbist, B. M., Ferrarini, L., Briaire, J. J., Zarowski, A., Admiraal-Behloul, F., Olofsen, H., Reiber, J. H. C., & Frijns, J. H. M. (2009). Anatomic considerations of cochlear morphology and its implications for insertion trauma in cochlear implant surgery. Otology and Neurotology, 30(4), 471–477.

Wanna, G. B., Noble, J. H., Carlson, M. L., Gifford, R. H., Dietrich, M. S., Haynes, D. S., Dawant, B. M.,

& Labadie, R. F. (2014). Impact of Electrode Design and Surgical Approach on Scalar Location and Cochlear Implant Outcomes. Laryngoscope, 124(S6), S1–S7.

Xu. J, R. K. S., R.E. Millard, G.M. Clark. (1997). Chronic electrical stimulation of the auditory nerve at high stimulus rates: a physiological and histopathological study. Hear Res., 105 (1–2) (1997), pp. 1-29.

Chapter 7

General discussion

Cochlear implant (CI) recipients generally regain hearing such that their quality of life improves as a result of the new communication possibilities that arise from implantation. However the variability in speech perception after implantation remains substantial, and CI outcomes can range from excellent to minimal speech recognition (Holden et al., 2013; Pisoni et al., 2017). As a result, further progress in CIs is highly desired. Objective measures are widely used to serve both clinical and scientific purposes in CIs. In the present thesis, we aimed to explore new applications of objective measures of CIs. Firstly we explored the temporal firing properties of the electrically excited auditory nerve fibers (ANFs) and their potential implications of these properties for speech perception after implantation based on electrophysiological objective measures. The second goal was to develop a tool for detecting the translocation of electrode arrays using nonphysiological objective measures.

In **Chapter 2**, an iterative deconvolution model was introduced which is capable of extracting the temporal firing properties of excited ANFs underlying human evoked compound action potential (eCAP). In **chapter 3**, this model was proven to be more robust in **Chapter 3** than the convolution model proposed by Strahl et al. (2016). The result of the estimated human UR demonstrated that the unitary response (UR) of human ANFs differed from the UR previously derived from the guinea pig ANFs (Versnel et al., 1992). The CDLD model with two Gaussian components turned out to be the optimal model, such that eCAPs can be described as a combination of two separate groups of neural responses with short and long latency. With this deconvolution model, we found in **Chapter 4** that a larger number and a greater degree of synchronicity of excited ANFs revealed by CDLDs lead to better speech perception performance after implantation. **Chapter 5** demonstrated that the refractory properties revealed by the short and long-latency components of the eCAP were different from each other and differed between children and adults. Importantly, the speed of recovery as obtained by the classical RRF method using the raw eCAP did not predict speech performance, while assessing the two components of the eCAP separately proven to be indicative of speech perception performance after implantation.

In **Chapter 6**, two impedance-based methods were proposed which are capable of detecting

translocation for HiFocus Mid-Scala electrode arrays without CT scan image using electrical field imaging (EFI) recording. These methods are viable to provide prompt feedback for surgeons after insertion, potentially enhancing their surgical skills and ultimately lowering the occurrence of translocations.

7.1 Application of physiological measures in cochlear implants

Over the years, cochlear implant systems have become more advanced. State-of-the-art systems are equipped with objective tools including neural response imaging/neural response telemetry that allow exploration of many factors that may provide implications for speech performance after implantation. These factors include the neuronal response of ANFs, the placement of the electrode array, among others (Fayad and Linthicum, 2006; Garadat et al., 2012).

With regard to the neural function, the temporal firing characteristics of excited ANFs were explored in this thesis based on eCAP measures. Under the UR assumption, i.e., that the action potential of each individual ANF identically contributes to the eCAP across subjects, electrode contacts and stimulus levels (e.g., Miller et al., 1990; Strahl et al., 2016; van Gendt et al., 2019), the temporal firing properties of excited ANFs in eCAPs were extracted by an iterative deconvolution model (**Chapter 2**). In this methodology, the UR plays an important role in obtaining accurate temporal firing properties of excited ANFs in eCAPs. It should be noted that the UR assumption may be an oversimplification of the actual contribution to the eCAP for all individual ANFs since this UR assumption are not completely verified yet. Differences in morphology and physiology between different species and between the cochleae of different patients and at different regions within a cochlea may result in differing URs, which in turn, affect the extraction accuracy of the temporal firing properties of excited ANFs. This speculation was supported by the results described in **chapter 3** that the eCAPs achieved with the estimated human UR were better than those achieved with a guinea pig UR reported by Versnel et al. (1992). Earlier studies also reported that for high stimulation levels the UR is unlikely to remain identical

for all different ANFs (e.g., Briaire and Frijns, 2005; Westen et al., 2011). In sum, using the averaged UR across differing factors (i.e., the stimulus levels, locations along the array and different patients) might to some extent deteriorate the accuracy of the extraction of these temporal firing properties. This could be a possible reason why the temporal properties of 6% eCAPs with deviant waveforms could not be validly extracted as described in **Chapter 3**. Therefore, assuming that the UR is variable and depends on multiple factors, more accurate temporal firing properties are likely obtained when using differing URs instead of the constant UR waveform estimated in **Chapter 2** and **Chapter 3**. The use of CDLDs instead of, e.g., the eCAP amplitude-based measures, may potentially improve the prediction of speech perception outcomes after implantation in CI recipients, as reported in **Chapter 4** and **Chapter 5**. However, our modeling study can neither answer whether the estimated human UR is physiologically realistic nor how it differs across different factors as stated above. To conclusively answer this question, further anatomical and electrophysiological studies on human UR are warranted. Nevertheless, even if the UR turned out to be not constant across factors, our deconvolution model can still be applied to this situation by running the iterative deconvolution model for each condition separately.

To explain some of the variability and optimize individual speech perception performance in CI recipients, another important neural factor is formed by the refractory characteristics of the auditory nerve. The auditory refractory properties can affect the capability of accurately encoding temporal information (e.g., Brown et al., 1990; Boulet et al., 2016; He et al., 2017) and are relevant to the survival status of the ANFs as well as speech perception (e.g., Stypulkowski and van den Honert, 1984; Wilson et al., 1994; He et al., 2017). In **Chapter 2** and **3**, we demonstrated that the eCAP waveform contains a short and long-latency neural response component. With regard to the origin of the two components, they may arise from the direct excitation of the axonal process and/or the peripheral process of the auditory nerve respectively (Stypulkowski and van den Honert, 1984). Another possibility is that the two groups of neural responses originated from two different groups of excited ANFs with different degrees of

degeneration and neural functionality. Thereby, the two groups of neural responses may differently affect CI outcomes. The latter hypothesis was supported by the results in **Chapter 5**, which showed the refractory properties of the two components in eCAPs were different from each other. In addition, the newly derived refractory parameters revealed differences in refractoriness between adults and children. Importantly, we found that the recovery speed of the short-latency component (S-RRF) but not the long-latency component significantly affected speech perception. Although further electrophysiological studies are warranted to completely understand the physiological mechanism of the two components in eCAPs, separately considering the refractory properties of the two separate components of eCAPs provided an additional interpretation of the variability of speech perception in CI recipients.

7.2 Application of nonphysiological measures in cochlear implants

The placement of the electrode array is an important factor that impacts the functionality of the electrode-neural interface as well as the speech understanding of patients with CIs (Usami et al., 2014; Dhanasingh et al., 2017; Liebscher et al., 2020). Unfortunately, misplacement of electrode arrays and trauma to the delicate structures within the cochlea may easily be caused as the surgeon is blind to what is happening inside the cochlea while the electrode array is being inserted. To date, electrode-array misplacements are detected commonly by analyzing postoperative (cone beam) CT images (e.g., Jia et al., 2018). However, since this radiology method requires additional work and leads to radiation exposure of patients, it is not routinely performed in many clinical practices. Therefore, an alternative, impedance-related tool for detecting electrode misplacement was developed in this thesis.

EFI measures the potential distribution through the scala tympani by recording the voltage on all electrode contacts along the electrode array when one contact is stimulated (Vanpoucke et al., 2004). With this technique, misplacements of electrode arrays can be detected, such as tip-folds over (Vanpoucke et al., 2012; Zuniga et al., 2017) and extracochlear electrodes (de Rijk et al.,

2020). Moreover, based on the results described in **Chapter 6**, one can reliably detect electrode translocations intra-operatively using the electrode impedance and access resistance using EFI measures without CT scans. This method is providing surgeons with prompt feedback, which could be beneficial for future CI insertions and reduce insertion trauma (Trehan et al. 2015).

However, the EFI-based method proposed in **Chapter 6** was not directly suitable for preventing the misplacement of the arrays. It would, therefore, be desirable to develop a tool by which surgeons can intraoperatively acquire prompt feedback regarding the placement of the electrode array and eventually avoid misplacement. The EFI measured by the CI can be used as an objective measurement to detect major issues with the electrode array placement (e.g. electrode fold-over or ossification) by making use of the multidimensional scaling method (Vanpoucke et al., 2012), while the electrode array insertion depth can be detected by the tissue resistance (see Fig. 1.4) (Aebischer et al., 2021). Together with the results described in **Chapter 6**, the impedance measures presumably could be adapted to deliver real-time impedance measurements during insertion, which could provide the feedback necessary to assess the intra-cochlear placement of the electrode arrays and guide the surgeon in avoiding misplacement of the array, such as, tip fold-overs. As a tip fold-over during insertion will occur first at the tip of the electrode array, theoretically, the whole situation of the placement of the electrode could be anticipated by measuring the impedance on the first several contacts. We assumed that when a tip fold-over occurs, the physical distance between the first apical contact and other contacts will change. This change is likely to be reflected by the impedance difference between the first apical contact and other contacts. Accordingly, a tip fold-over that is developing during surgery may potentially be detected and prevented by timely intervention by the surgeon, e.g., by adjusting the speed and/or the angle of the insertion or pulling the electrode back slightly.

To test the above assumption, a pilot study to develop a real-time intraoperative monitoring system based on the dynamic measurement of electrode impedance profiles was carried out. This system simultaneously stimulated apical electrodes E1 and E3, E4 and E5 and recorded impedances from electrode E6, such that the impedance differences between E1 and E3, E4, E5,

respectively were calculated (Δ Z1-3, Δ Z1-4 and Δ Z1-5). We simulated the insertion with and without a tip fold-over in a transparent plastic cochlear model with the aid of a microscope. If the electrode array was inserted correctly, the impedance differences were expected to follow this order: Δ Z1-3< Δ Z1-4 < Δ Z1-5. If a fold-over begins to occur, this order will be altered. This assumption was supported by the results of the pilot study (Fig. 7.1). When a tip fold-over began, the order of the impedance differences was changed. In this tip fold-over, ΔZ1-5 became the lowest one compared with Δ Z1-3 and Δ Z1-4 as E1 and E5 are approached each other. This alteration indicates that a tip fold-over is occurring. This pilot study proved that impedance-based measures can be used to develop a tool to prevent tip fold-over.

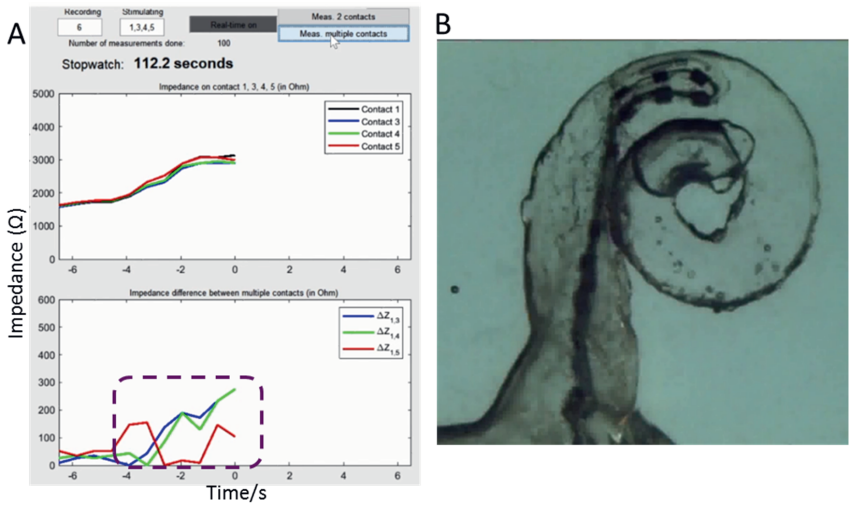

Fig.7.1 An example of electrode insertion with a tip fold-over reflected by the change of the order of the electrode impedance differences over time (A). When the fold-over is about to occur, the order of the impedance differences starts to switch (dashed square). The tip fold-over is observed in an image of the CI array in a transparent plastic dummy cochlea (B).

7.3 Clinical implications

The current research focused on the temporal firing properties of ANFs and the placement of the electrode arrays in clinical patients using objective measures. The findings regarding the temporal firing properties in the present thesis demonstrated that the eCAP waveform contains

clinically valuable information: (1) the temporal properties were age-related (i.e., children tended to present greater synchronicity and a larger number of excited ANFs) which suggested children had a better survival situation of ANFs in comparison with adults (**Chapter 3**); (2) The adult patients with greater neural synchronicity and the larger number of excited ANFs on average achieved better speech performance (**Chapter 4**); (3) in children, refractory properties of the short and long-latency component in eCAPs differed from their adult counterparts (**Chapter 5**); (4) the recovery speed from the relative refractoriness of the two components in eCAPs contributed differently to speech perception (i.e., a faster recovery speed of the short-latency neural component in eCAPs is associated with a greater speech perception) (**Chapter 5**). Therefore, the temporal firing properties of ANFs and the two components of the eCAP can provide a clinical correlate of ANF survival, neural functionality and postoperative speech perception performance. Thus, it is worthwhile to integrate the CDLD and the S-RRF into eCAP measures in future clinical practice.

Our study provided a viable and non-invasive method to detect the translocation of electrode arrays based on impedance measures (**Chapter 6**). This method was capable of detecting translocation in patients immediately after CI insertion. This feedback can potentially be beneficial for surgeons in improving their skills for future CI insertions and reduce insertion trauma. Besides, another advantage of this method over radiological methods is that our method is time-saving, cheaper and safer. The findings also suggested that further development of the impedance-based tool may be useful for monitoring the insertion of electrode arrays and avoiding misplacement as stated above.

7.4 Future perspectives

The findings in this thesis provide additional clinical implications for predicting the CI performance, understanding the variability of speech perception after implantation as well as detecting the placement of the electrode arrays as mentioned above. Accordingly, new areas of interest in the field of CIs will arise.

The human UR is mathematically derived in **Chapter 2 and 3**. However, whether this estimated UR is physiologically realistic remains unknown. To address this question, biological and electrophysiological single-unit recordings studies on human ANFs are needed. With a physiologically measured UR, the accuracy of the extracted temporal firing properties can be enhanced. In turn, better interpretation and prediction of CI performance is likely achievable. As our deconvolution model has low computational complexity, it could be potentially integrated into clinical software. Such a tool could extract the temporal firing information as well as the refractory properties underlying the two components in eCAPs of CI recipients in near-real-time. As a result, these properties can provide insights into the survival status of ANFs and give an upfront prediction of speech perception performance that can be achieved by an individual CI-recipient.

The impedance measures are expected to be applicable in real-time during electrode insertion, allowing for the development of an impedance-based real-time monitoring system. This system can measure the alteration of impedances at the first several tip contacts as the insertion progresses. Any alteration in impedance can be used as an indicator for the surgeon to prevent intra-cochlear misplacement of the electrode array (e.g., tip fold-overs, translocations as well as extracochlear electrodes) and unwanted trauma to delicate structures within the cochlea in future insertions. Before such a system can be built, our findings need to be verified in temporal bones and ultimately during CI surgeries.

The preoperative residual hearing of CI candidates is found to be an important factor that affects speech performance after implantation (e.g., Gibson 2017; Chiossi et al., 2017). Thus, damage to residual hearing caused during insertion needs to be minimized. The electrocochleography (ECochG) technique was recently introduced as an objective tool to intracochlearly record electrical potentials generated by the auditory nerve in response to acoustic stimulation. ECochG has been demonstrated to be a reliable intra-operative tool for predicting postoperative hearing loss and potentially optimizing surgical technique (Mandalà et al., 2016; Dalbert et al., 2018). Researchers also found that, on average, signal amplitudes of ECochG increase with higher

electrode insertion depths (e.g., Calloway et al., 2014), while a sudden decrease of its amplitude may indicate insertion trauma. These findings indicate that ECochG recordings may potentially provide real-time feedback for surgeons on whether the surgery and/or electrode insertion is inducing significant acute trauma to the cochlea and the damage to the residual hearing. In the future, such an ECochG-based real-time residual hearing monitoring system may be combined with the aforementioned real-time impedance monitoring system, capable of simultaneously monitoring ECochG and impedances of the apical contacts during the insertion.

REFERENCES

Abbas, P. J., and Brown, C. J. (1991). Electrically evoked auditory brainstem response: refractory properties and strength-duration functions. Hear. Res. 51, 139–147.

Aebischer, P., Meyer, S., Caversaccio, M., & Wimmer, W. (2020). Intraoperative Impedance-Based Estimation of Cochlear Implant Electrode Array Insertion Depth. IEEE transactions on biomedical engineering, 68(2), 545-555.

Boulet, J., White, M., & Bruce, I. C. (2016). Temporal Considerations for Stimulating Spiral Ganglion Neurons with Cochlear Implants. JARO - Journal of the Association for Research in Otolaryngology, 17(1), 1–17.

Briaire, J.J., Frijns, J.H.M., 2005. Unraveling the electrically evoked compound action potential. Hear. Res. 205, 143e156.

Brown, C. J., Abbas, P. J., & Gantz, B. (1990). Electrically evoked whole - nerve action potentials: Data from human cochlear implant users. The Journal of the Acoustical Society of America, 88(3), 1385–1391.

Calloway, N. H., Fitzpatrick, D. C., Campbell, A. P., Iseli, C., Pulver, S., Buchman, C. A., & Adunka, O. F. (2014). Intracochlear electrocochleography during cochlear implantation. Otology & Neurotology, 35(8), 1451-1457.

Chiossi, J. S. C., & Hyppolito, M. A. (2017). Effects of residual hearing on cochlear implant outcomes in children: a systematic-review. International journal of pediatric otorhinolaryngology, 100, 119-127.

Dalbert, A., Pfiffner, F., Hoesli, M., Koka, K., Veraguth, D., Roosli, C., & Huber, A. (2018). Assessment of cochlear function during cochlear implantation by extra-and intracochlear electrocochleography. Frontiers in neuroscience, 12, 18.

de Rijk, S. R., Tam, Y. C., Carlyon, R. P., & Bance, M. L. (2020). Detection of Extracochlear Electrodes in Cochlear Implants with Electric Field Imaging/Transimpedance Measurements: A Human Cadaver Study. Ear and hearing, 41(5), 1196–1207.

Dhanasingh, A., & Jolly, C. (2017). An overview of cochlear implant electrode array designs. Hearing Research, 356, 93–103.

Fayad, J. N., & Linthicum, F. H. (2006). Multichannel cochlear implants: Relation of histopathology to performance. Laryngoscope, 116(8), 1310–1320.

Fulmer, S. L., Runge, C., Jensen, J. W., and Friedland, D. R. (2011). Rate of neural recovery in implanted children with auditory neuropathy spectrum disorder. Otolaryngol. Head Neck Surg. 144, 274–279.

Garadat, S. N., Zwolan, T. A., & Pfingst, B. E. (2012). Across-site patterns of modulation detection: Relation to speech recognition. The Journal of the Acoustical Society of America, 131(5), 4030-4041.

Gibson, W. P. (2017). The clinical uses of electrocochleography. Frontiers in neuroscience, 11, 274.

He, S., Teagle, H. F. B., & Buchman, C. A. (2017). The electrically evoked compound action potential: From laboratory to clinic. Frontiers in Neuroscience, 11(JUN), 1–20.

Holden, L. K., Finley, C. C., Firszt, J. B., Holden, T. A., Brenner, C., Potts, L. G., ... & Skinner, M. W. (2013). Factors affecting open-set word recognition in adults with cochlear implants. Ear and hearing, 34(3), 342.

Jia, H., Torres, R., Nguyen, Y., De Seta, D., Ferrary, E., Wu, H., ... & Mosnier, I. (2018). Intraoperative conebeam CT for assessment of intracochlear positioning of electrode arrays in adult recipients of cochlear implants. American Journal of Neuroradiology, 39(4), 768-774.

Kiefer, J., Hohl, S., Stürzebecher, E., Pfennigdorff, T., and Gstöettner, W. (2001). Comparison of speech recognition with different speech coding strategies (SPEAK, CIS, and ACE) and their relationship to telemetric measure of compound action potentials in the nucleus CI 24M cochlear implant system. Audiology 40, 32–42.

Lee, E. R., Friedland, D. R., and Runge, C. L. (2012). Recovery from forward masking in elderly cochlear implant users. Otol. Neurotol. 33, 355–363.

Liebscher, T., Mewes, A., Hoppe, U., Hornung, J., Brademann, G., & Hey, M. (2020). Electrode Translocations in Perimodiolar Cochlear Implant Electrodes: Audiological and Electrophysiological Outcome. Zeitschrift für Medizinische Physik.

Mandalà, M., Colletti, L., Tonoli, G., & Colletti, V. (2012). Electrocochleography during cochlear implantation for hearing preservation. Otolaryngology-Head and Neck Surgery, 146(5), 774-781.

Miller, C.A., Abbas, P.J., Rubinstein, J.T., 1999b. An empirically based model of the electrically evoked compound action potential. Hear. Res. 135, 1e18.

Pisoni, D. B., Kronenberger, W. G., Harris, M. S., & Moberly, A. C. (2017). Three challenges for future research on cochlear implants. World Journal of Otorhinolaryngology-Head and Neck Surgery, 3(4), 240-254.

Strahl, S. B., Ramekers, D., Marjolijn M. B. Nagelkerke, K. E. S., Spitzer, P., Klis, S. F. L., Grolman, W., & Versnel, H. (2016). Assessing the Firing Properties of the Electrically Stimulated Auditory Nerve Using a Convolution Model. Adv Exp Med Biol, 894.

Stypulkowski, P. H., & van den Honert, C. (1984). Physiological properties of the electrically stimulated auditory nerve. I. Compound action potential recordings. Hearing Research, 14, 205–223.

Trehan, A., Barnett-vanes, A., Carty, M. J., & Mcculloch, P. (2015). The impact of feedback of intraoperative technical performance in surgery : a systematic review, 1–5.

Turner, C., Mehr, M., Hughes, M., Brown, C., and Abbas, P. (2002). Within-subject predictors of speech recognition in cochlear implants: a null result. Acoust. Res. Lett. Online 3, 95–100.

Usami, S. I., Moteki, H., Tsukada, K., Miyagawa, M., Nishio, S. Y., Takumi, Y., Iwasaki, S., Kumakawa, K., Naito, Y., Takahashi, H., Kanda, Y., & Tono, T. (2014). Hearing preservation and clinical outcome of 32 consecutive electric acoustic stimulation (EAS) surgeries. Acta Oto-Laryngologica, 134(7), 717–727.

van Gendt, M. J., Briaire, J. J., & Frijns, J. H. M. (2019). Effect of neural adaptation and degeneration on pulse-train ECAPs: A model study. Hearing Research, 377, 167–178.

Vanpoucke, F. J., Zarowski, A. J., & Peeters, S. A. (2004). Identification of the impedance model of an implanted cochlear prosthesis from intracochlear potential measurements. IEEE Transactions on Biomedical Engineering, 51(12), 2174–2183

Vanpoucke, F. J., Boermans, P. B. P. B., & Frijns, J. H. (2012). Assessing the placement of a cochlear electrode array by multidimensional scaling. IEEE Transactions on Biomedical Engineering, 59(2), 307–310.

Versnel, H., Prijs, V. F., & Schoonhoven, R. (1992a). Round-window recorded potential of single-fibre discharge (unit response) in normal and noise-damaged cochleas. Hearing Research, 59(2), 157–170.

Westen, A. A., Dekker, D. M. T., Briaire, J. J., & Frijns, J. H. M. (2011). Stimulus level effects on neural excitation and eCAP amplitude. Hearing Research, 280(1–2), 166–176.

Wilson, B. S., Finley, C. C., Lawson, D. T., and Zerbi, M. (1994). Speech Processors for Auditory Prostheses. NIH Project N01-DC-2-2401. Seventh Quarterly Progress Report.

Zuniga, M. G., Rivas, A., Hedley-Williams, A., Gifford, R. H., Dwyer, R., Dawant, B. M., ... & Labadie, R. F. (2017). Tip fold-over in cochlear implantation: case series. Otology & Neurotology: Official Publication of the American Otological Society, American Neurotology Society [and] European Academy of Otology and Neurotology, 38(2), 199

Chapter 8

Summary

The treatment of severe to profound sensorineural hearing loss has rapidly evolved in the last several decades. The cochlear implant (CI) device, which forms an interface between a sound signal and the auditory nerve fibers (ANFs) of the deaf ear, is by now an accepted approach of rehabilitation for profoundly deaf individuals and generally achieves high performance in terms of speech perception. However, effectiveness still widely varies from person to person. Therefore, there is a continued impetus for further progress in CIs. In this thesis, we developed new applications of objective measures in modern CIs regarding electrically evoked compound action potential (eCAP) recording and electrical field imaging (EFI). With the development of an iterative deconvolution model, this thesis focuses on extracting the temporal firing properties of excited ANFs in human eCAP and evaluating their potential implications for clinical practice. In addition, this thesis describes an attempt to intra-operatively assess the placement of the electrode array within the cochlea based on impedance measurements.

Chapter 1 presents a general introduction to the basic principle of CI devices. Then the commonly used objective measurement tools in cochlear implantation are explained in more detail. At the end of this chapter, the outline of the present thesis is given.

Chapter 2 describes a study that constructs an iterative deconvolution model with two steps for estimating the human auditory unitary response (UR) and deriving the underlying neural excitation pattern of the excited ANFs. The recorded human eCAPs were entered as input for this model to estimate the human unitary response (UR) in the first step and obtain the compound discharge latency distribution (CDLD) that reflects the contributions from individual ANFs to human eCAPs in the second step. In this method, an eCAP was modeled by convolving a UR model with a CDLD model. Then, the modeled eCAP was optimized by iteratively manipulating the variables in the parameterized UR and CDLD models, until the modeled eCAP converged to the recorded eCAPs. With this method, the human UR and/or CDLD can be obtained automatically.

Chapter 3 describes the validation process by applying the iterative deconvolution model

developed in **Chapter 2** to a relatively large dataset of human eCAP recordings, consisting of 4982 eCAPs from 111 CI recipients. With this model, a human version of the UR was estimated for the first time, which differs significantly from the guinea pig UR. With the estimated human UR, the CDLDs of 4660 eCAPs were validly extracted. Such CDLDs provided better estimates of the number of excited ANFs and their firing latencies. It was demonstrated that CDLDs had advantages over the more commonly used eCAP amplitude as they better reflected the temporal firing properties of excited ANFs. As the CDLD model with two Gaussian components was validated as the optimal model, the eCAP waveform can be described as a combination of a short and long-latency neural component (S-eCAP and L-eCAP). It was concluded that this iterative deconvolution was capable of deriving the temporal firing properties of excited ANFs underlying eCAPs, which may be clinically useful. As an example, significant differences in the temporal firing properties of excited ANFs between children and adults were found.

Chapter 4 investigates the potential clinical implication of eCAP waveforms by taking the temporal firing properties of the ANFs into account. This chapter reports on a retrospective study evaluating the effect of the temporal firing properties and the number of excited ANFs on the speech perception performance of 134 postlingually deaf adult CI recipients. With the iterative deconvolution model proposed in **Chapter 2**, the CDLD corresponding to each eCAP was obtained, and the number, peak latencies and the synchronicity of excited ANFs were calculated. It turned out that CI recipients with a larger number and greater synchronicity of excited ANFs tend to achieve better speech perception after implantation. On the contrary, the average latencies of CDLDs did not significantly affect speech perception. This study underlines the importance of taking temporal firing properties of excited ANFs in eCAPs into consideration when one investigates if eCAP recordings are indicative of speech outcomes.

Chapter 5 characterizes the refractory properties of ANFs underlying the S-eCAP and L-eCAP, and tests whether these refractory properties of children differ from those of adults as well as whether they are associated with speech perception. This retrospective study used the refractory recovery function recording obtained from 130 Hi-Focus Mid-Scala or 1J cochlear implant

(Advanced Bionics, Valencia, CA) recipients. We demonstrated that the auditory refractory properties of the S-eCAP and L-eCAP are different. We also found that these refractory properties were age-related, including that children show significantly shorter absolute refractory periods and larger saturation levels than adults. In addition, a trend that slower recovery of the S-eCAP was associated with better speech perception was found. Thus, it is worthwhile giving considerations to the two components of the eCAP in the future when assessing the clinical values of the auditory refractory properties for clinical purposes.

Chapter 6 reports a study that assessed whether the electrode impedance and the access resistance can be used to detect electrode translocation using electrical field imaging, and which metric is more feasible. A total of 100 subjects who received a HiRes90K cochlear implant with a Mid-Scala electrode were included in this study. The normal values of these two measurements were estimated as the baselines of the implant placed in the cochlea without translocation. The maximal electrode impedance deviation and the maximal access-resistance deviation from the respective baselines were calculated as detectors of translocation. It turned out that both metrics can reliably detect translocations. However, the access resistance had significantly greater accuracy and it also reliably detected the electrode-location of translocations. These measures can provide prompt feedback for surgeons after implantation, improving their surgical skills, and ultimately reducing the occurrence of translocations. In the future, these measures may allow near-real-time monitoring of the electrode array during insertion and help to avoid translocations.

Chapter 7 contains a general discussion of the results and the main conclusions of the studies presented in this thesis. Moreover, the clinical implications of the findings in this thesis and future perspectives are discussed.

Samenvatting

De laatste decennia is er veel veranderd in de behandeling van patiënten met ernstig tot zeer ernstig perceptief gehoorverlies. Het cochleaire implantaat (CI) is inmiddels een effectieve en geaccepteerde behandeling voor revalidatie van dove tot ernstig slechthorende patiënten. De CI vormt een interface tussen een extern geluidssignaal en de gehoorzenuwvezels (ANF's). Mensen met een CI behalen over het algemeen goede prestaties op het gebied van spraakperceptie, echter variëren de uitkomsten nog steeds sterk van persoon tot persoon. Daarom blijft er een aanhoudende noodzaak voor verdere ontwikkeling binnen het veld van cochleaire implantatie. In dit proefschrift hebben we nieuwe toepassingen ontwikkeld voor objectieve metingen in moderne CI's met betrekking tot elektrisch opgewekte samengestelde actiepotentialen (eCAP) en beeldvorming van het elektrische veld (EFI). Met de ontwikkeling van een iteratief deconvolutiemodel richt dit proefschrift zich op het extraheren van de temporele vuureigenschappen van aangeslagen ANF's in menselijke eCAPs en het evalueren van de mogelijke implicaties voor de klinische praktijk. Daarnaast beschrijft dit proefschrift een poging om intra-operatief de locatie van de elektrode-array in het slakkenhuis te beoordelen op basis van impedantiemetingen.

Hoofdstuk 1 geeft een algemene inleiding over het basisprincipe van CI's. Vervolgens worden de veelgebruikte objectieve meetinstrumenten bij cochleaire implantatie in meer detail uitgelegd. Aan het einde van dit hoofdstuk worden de hoofdlijnen van dit proefschrift uiteengezet.

Hoofdstuk 2 beschrijft een studie die een iteratief deconvolutiemodel construeert met twee stappen voor het schatten van de menselijke auditieve unitaire respons (UR) en het afleiden van het onderliggende neurale excitatiepatroon van de geëxciteerde ANF's. In de eerste stap werden de geregistreerde menselijke eCAP's ingevoerd als input voor het model om de menselijke unitaire respons (UR) te schatten en de samengestelde ontladingslatentieverdeling (CDLD) te verkrijgen. De CDLD weerspiegelt de bijdragen van individuele ANF's aan menselijke eCAP's welke in de tweede stap aan bod komen. Bij deze methode werd een eCAP gemodelleerd door de convolutie van een UR-model met een CDLD-model. Vervolgens werd de gemodelleerde eCAP geoptimaliseerd door de variabelen in de geparametriseerde UR- en CDLD-modellen

iteratief te manipuleren, totdat de gemodelleerde eCAP convergeerde naar de geregistreerde eCAP's. Met deze methode kunnen de menselijke UR en CDLD automatisch worden verkregen.

Hoofdstuk 3 beschrijft het validatieproces van het iteratieve deconvolutiemodel dat in hoofdstuk 2 is ontwikkeld door dit model toe te passen op een relatief grote dataset van menselijke eCAP-registraties, bestaande uit 4982 eCAP's van 111 CI-ontvangers. Met dit model wordt voor het eerst een menselijke versie van de UR geschat, die significant afwijkt van de UR van de cavia. Met de geschatte menselijke UR werden de CDLD's van 4660 eCAP's geëxtraheerd. Dergelijke CDLD's geven betere schattingen van het aantal geëxciteerde ANF's en de latentietijden van de vuureigenschappen. Er werd aangetoond dat het gebruik van CDLD's voordelen biedt ten opzichte van de meer algemeen gebruikte eCAP-amplitude omdat ze de temporele eigenschappen van geëxciteerde ANF's beter weerspiegelen. Na validatie bleek het CDLD-model met twee Gauss-componenten het optimale model voor het beschrijven van de eCAP-golfvorm. De eCAP-golfvorm kan worden beschreven als een combinatie van een neurale component met een korte en een lange latentietijd (S-eCAP en L-eCAP). Er werd geconcludeerd dat deze iteratieve deconvolutie in staat was om de tijdelijke eigenschappen van aangeslagen ANF's die ten grondslag liggen aan eCAP's af te leiden. Deze informatie kan klinisch bruikbaar zijn. Als voorbeeld: er werden significante verschillen gevonden in de temporele eigenschappen van geëxciteerde ANF's tussen kinderen en volwassenen.

Hoofdstuk 4 onderzoekt de mogelijke klinische implicaties van eCAP-golfvormen door rekening te houden met de temporele vuureigenschappen van de ANF's. Dit hoofdstuk bevat een retrospectieve studie evalueerde het effect van de temporele vuureigenschappen en het aantal geëxcitereerde ANF's op de spraakperceptie van 134 postlinguaal dove volwassen CI-ontvangers. Met het iteratieve deconvolutiemodel wat is voorgesteld in Hoofdstuk 2 werd de CDLD die overeenkomt met elke eCAP verkregen. Tevens werden de pieklatenties en de synchroniciteit van aangeslagen ANF's berekend. Het bleek dat mensen met een CI met een groter aantal en grotere synchroniciteit van geëxciteerde ANF's de neiging hebben om na implantatie een betere spraakperceptie te bereiken. Echter hadden de gemiddelde latenties van CDLD's geen

significante invloed op de spraakperceptie. Deze studie onderstreept dat vuureigenschappen van ANF's in eCAP's in overweging moeten worden genomen wanneer men onderzoekt of eCAP-opnames indicatief zijn voor spraakverstaan.

Hoofdstuk 5 karakteriseert de refractaire eigenschappen van ANF's die ten grondslag liggen aan de S-eCAP en L-eCAP en test of de refractaire eigenschappen van kinderen verschillen van die van volwassenen. Ook wordt onderzocht of deze eigenschappen geassocieerd zijn met perceptie van spraakverstaan. Deze retrospectieve studie maakte gebruik van de opnames van refractaire herstelfuncties van 130 Hi-Focus Mid-Scala of 1J cochleaire implantaten (Advanced Bionics, Valencia, CA). We hebben aangetoond dat de auditieve vuurvaste eigenschappen van de S-eCAP en L-eCAP verschillend zijn. We ontdekten ook dat deze refractaire eigenschappen leeftijdsgebonden waren en mede dat kinderen significant kortere absolute refractaire perioden en grotere verzadigingsniveaus laten zien dan volwassenen. Bovendien werd een trend gevonden dat langzamer herstel van de S-eCAP geassocieerd was met een beter spraakverstaan. Het is dus de moeite waard om in de toekomst rekening te houden met de twee componenten van de eCAP bij het beoordelen van de klinische waarden van de auditieve refractaire eigenschappen.

Hoofdstuk 6 rapporteert een onderzoek waarin is onderzocht of de elektrode-impedantie en de toegangsweerstand kunnen worden gebruikt om translocatie van elektroden te detecteren met behulp van elektrische veld beeldvorming en welke metriek hiervoor het meest optimaal is. Een totaal van 100 proefpersonen die een HiRes90K cochleair implantaat met een Mid-Scala-elektrode ontvingen werden in deze studie opgenomen. De normale waarden van deze twee metingen werden geschat als de basislijnen van het implantaat dat zonder translocatie in het slakkenhuis werd geplaatst. De maximale afwijking van de elektrode-impedantie en de maximale afwijking van de toegangsweerstand van de respectieve basislijnen werden berekend als translocatiedetectoren. Het bleek dat beide metrieken op betrouwbare wijze translocaties kunnen detecteren. De toegangsweerstand had echter een aanzienlijk grotere nauwkeurigheid en detecteerde ook betrouwbaar de elektrode-locatie van translocaties. Deze middelen kunnen chirurgen na implantatie snel feedback geven waardoor zij hun chirurgische vaardigheden

kunnen verbeteren en uiteindelijk het optreden van translocaties kunnen verminderen. In de toekomst kunnen deze maatregelen het mogelijk maken om de elektrode-array tijdens het inbrengen in realtime te volgen en translocaties te helpen voorkomen.

Hoofdstuk 7 bevat een algemene bespreking van de resultaten en de belangrijkste conclusies van de onderzoeken die in dit proefschrift worden gepresenteerd. Bovendien worden de klinische implicaties van de bevindingen en de toekomstperspectieven in dit proefschrift besproken.

List of publications

List of publications

Published

Dong, Y., Briaire, J.J., Siebrecht, M., Stronks, H.C., Frijns, J.H.M. (2021). Detection of Translocation of Cochlear Implant Electrode Arrays by Intracochlear Impedance Measurements. Ear Hear. 42, 1397–1404.

Dong, Y., Briaire, J. J., Biesheuvel, J. D., Stronks, H. C., & Frijns, J. H. M. (2020). Unraveling the Temporal Properties of Human eCAPs through an Iterative Deconvolution Model. Hearing Research, 395, 108037.

Dong, Y., Stronks, H. C., Briaire, J. J., & Frijns, J. H. M. (2021). An iterative deconvolution model to extract the temporal firing properties of the auditory nerve fibers in human eCAPs. MethodsX, 2021, 101240, ISSN 2215-0161.

Paper submitted

Dong, Y., Briaire, J. J., Stronks, H. C., & Frijns, J. H. (Under review). Predicting speech performance in individuals with cochlear implants, based on temporal firing properties of auditory nerve fibers derived from eCAPs. Ear and Hearing. 2021

Dong, Y., Briaire, J. J., Stronks, H. C., & Frijns, J. H. M. (Under review). Short and long-latency components of the eCAP reveal different refractory properties. Hearing Research. 2021.

Curriculum Vitae

Yu Dong was born on January 15, 1988, in Shehong county, Sichuan province, China. After finishing secondary education in 2007, he began his bachelor study majoring in Machine Design Manufacture and Automation at the Ocean University of China, in Qingdao, China. He received a Bachelor of Engineering degree in Mechanical engineering in June 2011. In that same year, he started working as an assistant mechanical engineer in Haiyang CIMC offshore Co. Ltd, Yan Tai city. In 2014, he began his master study as a researcher at the State Key Laboratory of Cognitive Neuroscience and Learning at the Beijing Normal University, for which the neural mechanism of temporal prediction was investigated in a primate rhesus model. He graduated with a Master of Science with his thesis titled "*The study of temporal prediction, neural mechanisms and the relationship with microsaccade in macaque monkeys*" in 2017. In September 2017, he began as a PhD student at the Department of Otorhinolaryngology at the Leiden University Medical Center, Leiden, the Netherlands (supervisors Prof. Dr. Ir. J.H.M. Frijns, Dr. Ir. J.J. Briaire and Dr. H.C. Stronks) with a focus on cochlear implants (2017-2021). The results of this study are described in the present thesis.

Acknowledgments

I would like to express my sincere appreciation to ones for their help, support and encouragement in my PhD study and writing the present thesis.

First and foremost, I would like to thank my promoter Johan Frijns, and supervisors Jeroen Briaire and Christiaan Stronks for your timely and patient support and guidance not only in implementing my scientific research but also in improving my language, tackling with difficulties encountered in life within these four years. Without you, I could not have achieved this much.

I also would like to express my thanks to all colleagues in the ENT department. All of you are always so helpful and warm-hearted which makes me feel at home. Many thanks to my sweet roomies, colleagues and friends Michael, Timo, Margriet, Klaas, Kimberly, Tirza, Dick, Constanza, Edward, Randy, Wouter, Juliette, Victor and so on. I am so happy being part of you and working with you. I have learned a lot from you in terms of critical thinking on many different things in research and daily life. I greatly enjoyed sharing different life experiences, drinking, having dinner, sailing, playing board games, having parties and best weekends together with you. In addition, great thanks to the German dolphin, Michael, for saving me out of the Dead Sea in Israel and teaching me how to swim.

I would like to sincerely thank my dear Chinese friends Fangfang, Wanbin, Wei Chen, Minkang, Guiying Wang, Chu Wenjing, Zhao Yang, Ding Ding, Hehui Li, Junjie Wu, Min Li and all my friends. Many thanks for your valuable friendship, mutual help and encouragement when I am in a foreign land. I enjoyed conversating, drinking, having dinner and playing games together with all of you. Thank you for your warm friendship that always helped me to get back to work full of energy!

Last but not least, I would like to thank my family for your support as always. My dear dad and mom, you have been continuously contributing so much to me that I can achieve the goals in each stage of my study. My dear brother, thanks for your support and encouragement and always

being with me! My dear girlfriend Sarah Wang, it is extremely fortunate to meet you and fall in love with you in the Netherland as we both graduated from Beijing Normal University without previously knowing each other. Many thanks for not only accompanying me over the last two years especially during the tough Covid-19 time but also taking care of me. Your love, tenderness and support help me go through huge difficulties in my PhD study and life. Here, I also would like to greatly thank Qingyu Meng for building the connection between me and Sarah.